

Stellingen

behorende bij het proefschrift

Nuclear reactor noise investigations on boiling effects in a simulated MTR-type fuel assembly

1. The slope of the phase of the cross spectrum between noise signals of an in-core neutron detector and a core-exit thermocouple depends on the fuel-to-coolant heat transfer coefficient. This effect contributes to the difference, observed experimentally by Sweeney and others, between the known coolant velocities in cores of pressurized water reactors and velocities inferred from noise measurements.

F.J. Sweeney, B.R. Upadhyaya, D.J. Shieh, Progress in Nuclear Energy, Vol. 15, p. 201 (1985)

R. Kozma, T. Katona, Proc. 6th Power Plant Dynamics, Control and Testing Symp., Knoxville, U.S.A., Vol. 4, pp.40.01 (1986)

2. By making use of a number of acoustic sensors and hydrogen meters in sodium-water steam generators, the leakage of water into the sodium loop through micro-cracks can be diagnosed at an early stage.

Katona T., R. Kozma, G. Uhlmann, Report ZfK-432 (1981)

Kozma R., T. Katona, Report KFKI-1983-60 (1983)

3. The low-frequency space dependence of the neutron noise measured by Kostic and colleagues in a pressurized water reactor can be interpreted as a strong thermohydraulic feedback effect.

Kostic Lj., J. Runkel, D. Stegemann, Prog. Nucl. Energy, Vol.21, p.421 (1988)

Kozma R., L. Mesko, Prog. Nucl. Energy, Vol.15, p.699 (1985)

4. The nonlinear behaviour of the phase of cross spectra between in-core self-powered neutron and gamma detectors observed by various authors in boiling water reactors can be explained by the presence of different velocities in churn- and slug-flow regimes in the core.

Kozma R., Proc. Symp. on Nuclear Reactor Surveillance and Diagnostics (SMORN VI), Knoxville, U.S.A., Vol.1., p.38.01 (1991)

5. The basic ideas and a number of methods of nuclear reactor noise analysis can be applied to the monitoring of the state of various technical and even biological systems.

6. The great Hungarian statesman Count István Széchenyi (1791-1860) wrote:
"Well-trained minds represent the real power of the nation."
This statement is now the key to Hungarian recovery.
7. Nuclear reactor science uses and produces core technologies. Therefore, efforts aimed at slowing down or abandoning research and development activities in this field are, in fact, questioning the driving forces of the modern culture.
8. The terminology "global noise component" introduced by Wach and Kosaly and now widely used in the theory of local-global decomposition of neutron noise is misleading, as the global noise component exhibits clear space-dependence in power reactors and, therefore, it is not an overall fluctuation which is essentially the same in the entire core.
Wach D., G. Kosaly, Atomkernenergie, Vol. 23, p.244 (1974)
9. The real understanding of a theory implies knowing exactly its limitations.
10. When collecting all the cherries from a cherry tree, it is wiser to choose a good position on the tree and collect all the cherries which can be reached from that position and then move to another place instead of always looking for the most reachable fruit and trying to have it in your basket.
11. Traffic jams could be reduced significantly if drivers kept the proper distance between each other. The same is true in the case of bubbles in narrow coolant channels.

**TR diss
2056**

**NUCLEAR REACTOR NOISE
INVESTIGATIONS ON BOILING EFFECTS IN
A SIMULATED MTR-TYPE FUEL ASSEMBLY**

544467
3172735
TR diss 2056

R. Kozma

Interfacultair Reactor Instituut van de Technische Universiteit Delft

CIP-GEGEVENS KONINLIJKE BIBLIOTHEEK, DEN HAAG

Kozma, Robert

Nuclear reactor noise investigations on boiling effects in
a simulated MTR-type fuel assembly / Robert Kozma. -
Delft : Interfacultair Reactor Instituut, Delft
University of Technology. - Ill.
Proefschrift Technische Universiteit Delft. - Met lit.
opg.

ISBN 90-73861-04-7

NUGI 812

Trefw.: kernreactoren / reactorruis.

**NUCLEAR REACTOR NOISE INVESTIGATIONS ON
BOILING EFFECTS IN A SIMULATED MTR-TYPE
FUEL ASSEMBLY**

PROEFSCHRIFT

**TER VERKRIJGING VAN DE GRAAD VAN DOCTOR
AAN DE TECHNISCHE UNIVERSITEIT DELFT,
OP GEZAG VAN DE RECTOR MAGNIFICUS,
PROF. DRS. P.A. SCHENCK,
IN HET OPENBAAR TE VERDEDIGEN TEN OVERSTAAN
VAN EEN COMISSIE
AANGEWEZEN DOOR HET COLLEGE VAN DEKANEN
OP 4 MEI 1992 TE 14.00 UUR**

DOOR

ROBERT KOZMA



geboren te Szeged, Hongarije,

**Master of Science in applied mathematics
Engineer in thermal physics**

Dit proefschrift is goedgekeurd door de promotor:
Prof. dr. ir. H. VAN DAM

toegevoegd promotor: dr. ir. J. E. HOOGENBOOM



The investigations described in this thesis have been performed in the group of Nuclear Reactors of the Department of Reactor Physics, Interfaculty Reactor Institute, Delft University of Technology, Mekelweg 15, 2629 JB Delft, The Netherlands.

To my parents
To Valerie and Robert-Thijs

Contents

Chapter 1	
Introduction	1
Chapter 2	
The NIOBE Facility	5
2.1 General considerations	5
2.2 Description of NIOBE	7
2.3 Thermohydraulic state of the coolant	11
2.3.1 Heat losses	12
2.3.2 Nuclear heating	14
2.3.3 Fuel to coolant heat transfer	14
2.3.4 Temperature distribution in the plates	17
2.4 Neutron flux perturbations at NIOBE	22
2.5 Main features of NIOBE	26
Chapter 3	
Flow Measurements Using Noise Signals of Axially Displaced Thermocouples	27
3.1 Introduction	27
3.2 Experimental conditions	29
3.3 Temperature Noise Measurements	30
3.4 Some important aspects of the thermohydraulics of NIOBE	39
3.5 Discussion	41
3.6 Model calculations	42
3.7 Conclusions	48

Chapter 4	
Identification of Flow Patterns	
During Actual Coolant Boiling in	
Thin Rectangular Channels	51
4.1 Introduction	51
4.2 Description of the experiments	55
4.2.1 Parameters of experiments	55
4.2.2 DC component of signals of neutron detectors	56
4.3 Neutron noise effects	58
4.3.1 Time domain analysis	58
4.3.2 Neutron noise spectra and correlation functions	63
4.4 Flow identification	66
4.5 Concluding remarks	69
 Chapter 5	
Detection of Coolant Boiling Using	
Temperature and Neutron Noise	71
5.1 Introduction	72
5.2 Experimental	75
5.3 Description of temperature noise	
at subcooled boiling : an overview	75
5.4 Temperature noise at different levels	
of boiling at NIOBE	78
5.5 Neutron noise measurements	83
5.6 Conclusions	86
 Chapter 6	
Boiling Neutron Noise at High	
Frequencies	89
6.1 Introduction	89
6.2 Theory of boiling reactor noise	90
6.3 Bernoulli statistics of boiling noise	93
6.4 Periodic bimodal noise	97

6.5 Bubble injection experiments	99
6.5.1 Overview	99
6.5.2 Experimental	99
6.5.3 Analysis of neutron noise NRMS	104
6.6 Experiments with subcooled boiling	107
6.6.1 General	107
6.6.2 Subcooled boiling description	108
6.6.3 Neutron noise NRMS effects	109
6.6.4 An anomaly detection method	112
6.7 Conclusions	114
 Chapter 7	
Low-Frequency Neutron Noise Analysis	115
7.1 Introduction	115
7.2 Neutron noise coherence at low frequencies	116
7.3 Spectral distribution of boiling neutron noise	120
7.4 Remarks on feedback effects	122
7.5 Conclusions	123
 Appendix A	
Nomenclature	125
 Appendix B	
Temperature Diffusion in the Fuel Plate	129
 Bibliography	133
 Summary	139
 Samenvatting	141
 Acknowledgements	145
 Curriculum Vitae	147

Chapter 1

Introduction

In a physical experiment, certain parameters of an object are controlled while other variables are being observed. If the set of parameters of the experiment is chosen properly, the values of the observed variables can be reproduced by repeating the experiment with the same parameters. We say that the space of controlled parameters is complete with respect to the space of observed variables in that case. Of course, the observed variables will never be exactly the same in different experiments, but they are distributed around an average value, and the deviation from the average are attributed to experimental errors. On the other hand, the controlled parameters form an incomplete space if no repeatability is found in the above sense. By expanding the space of controlled parameters with properly chosen additional parameters, repeatability can be achieved.

Another problem arises when no variation is observed although the state of the system has been changed during the experiment. This means that the observed variables are not the proper ones, and their space has to be completed. In some cases, however, no additional variables are available. Then the information contained in the small (time-dependent) fluctuations of the observed variables can furnish us with the proper information. Noise monitoring is based on the analysis of these small fluctuations which are inherently present in the signal.

At a nuclear reactor, neutron detectors are located inside and around the core, and there are also thermocouples, pressure sensors, accelerometers, etc., around the core. Certain tasks of nuclear reactor monitoring cannot be accomplished by using their DC signals only. Often there is no room for additional instrumentation, or the placement of extra detectors would contradict the other safety aspects of the core. In this situation, neutron noise

analysis has a clear advantage, as it gives additional information about the reactor without using extra detectors. In this work, neutron noise methods are studied.

We focus on problems related to boiling effects in light-water reactors (LWRs). The presence of coolant boiling has different implications on the reactor operation, depending on the type of LWR investigated. The onset of boiling is undesirable in research reactor cores, and it is considered to be an accidental situation, for it can easily lead to burnout and consequent fuel melting [Woo84]. Coolant boiling has to be prevented by all means, and, in case of occurrence, it has to be detected as early as possible in order to avoid further damage of the reactor fuel [DVr86].

Subcooled boiling is allowed at regions with the highest heat flux densities in the cores of modern pressurized water reactors (PWRs). A reliable method of subcooled boiling monitoring is welcomed here. Saturated boiling has been detected in PWRs operating under abnormal circumstances [Def88], [Rin85], but, in spite of significant efforts, no reliable method of subcooled monitoring has been established in PWR cores yet [Kat85], [Koz86], [Bau88], [Por88].

In boiling water reactors (BWRs), the operating pressure level is low compared to PWRs, and two-phase coolant flow takes place in the larger part of BWR cores. The structure of the coolant flow is different at different axial elevations. After an initial warming-up region with single-phase coolant, bubbly-flow occurs first, followed by slug, churn and annular flow-regimes. In large BWR cores, annular to mist flow-regime transition occurs as well, which results in the presence of single-phase vapour flow at the highest axial elevations. Determination of two-phase flow characteristics (e.g. velocity distribution and void fraction) and stability monitoring [VDH89] are the main tasks of noise monitoring in BWRs. A critical overview of the existing parameter monitoring methods is given in [Lub84].

Methods based on effects of parametric fluctuations of core properties are widely used in practical noise analysis. In that approach, the response of a reactor to parametric excitations is determined from neutronic principles (e.g. transport or diffusion models), and the generating noise source is specified on the basis of thermohydraulic considerations [VDa76]. This approach serves as a theoretical basis of the 'local-global' decomposition of neutron noise, a dominating concept of reactor noise during the past 15 years.

Assume that the neutronic properties of the reactor are completely known. Then, the measured neutron noise can be used to gain information about the noise sources. On the other hand, if the noise sources are known (e.g. they can be approximated as white noise), certain parameters of the core can

be inferred. Also, combinations of these methods found their application in reactor noise practice, such as parametric noise sources, etc.

Local neutron noise can be investigated in research reactors by introducing air bubbles into the core. Air bubbles move upwards and cause propagating perturbations of the coolant density. In this way, one can study how the presence of void affects the noise signals of neutron detectors located either in the surroundings of or at a larger distance from the perturbation. The results of such measurements helped to reveal the structure of the neutron noise field, to identify its 'local-global' character, and to analyse in detail local changes in the neutron noise [Fug77], [Kle79], [Kos82]. This method, however, has certain shortcomings, as the generation and collapse of steam bubbles cannot be modelled properly with the help of noncondensable air bubbles.

An adequate treatment requires inducing actual boiling in the test section. This has been done at the 5 MW research reactor of the Paul Scherrer Institute, Wurenlingen, when coolant boiling was generated in the core by reducing the flow rate through and/or by increasing the reactor power [Beh82]. During these experiments, boiling was detected by analysis of noise signals of ionisation chambers located in the reflector and optically as well. Boiling effects under well-defined thermohydraulic circumstances have been investigated by the IRENE loop at the OSIRIS reactor, Saclay. The noise signal of an in-core neutron detector located in the boiling region clearly indicates coolant boiling when the steam content exceeds a certain threshold value [Ber82].

It was clear from the very beginning of modelling parametric effects that thermohydraulic feedback is not included in this treatment. Feedback effects are sometimes called structural effects [Koz88a], for the presence of feedback changes the structure of the neutronics of the core. The increasing interest in thermohydraulic feedback is generated by the need for interpreting low-frequency effects in LWRs (space-dependence, stability, etc.) and by the limitations of core monitoring methods based on 'local-global' effects only. An advantage of feedback models is that certain fundamental thermohydraulic processes are inherently included in the description [Kle81b]. This needs, in turn, more complicated mathematical tools as, for example, the method of spatial higher harmonics [Kon82] and the state-space approach [Mes84], [Koz85a].

An additional aspect of boiling in research reactor cores has to be emphasized. Research reactors often use plate-type fuels with relatively narrow coolant channels; the width of the channels is in the range of 2 - 3 mm.

Boiling in narrow channels is not a well-studied phenomenon, and the investigation of boiling effects in this geometry is interesting in its own right. Therefore, thermohydraulic studies form a significant part of the present work.

Boiling experiments at HOR have a relatively long history that began more than a decade ago. Following some introductory out-of-pile experiments, a boiling setup was operating at HOR between 1984 and 1986. Based on the experience of that setup, a new boiling experiment, NIOBE (Noise Investigations On Boiling Effects), has been designed. The NIOBE setup has been in operation since the end of 1986. The present work contains results of experiments performed between 1988 and 1991, with the exception of Chapter 5, in which experiments with the predecessor of NIOBE are treated.

In Chapter 2, the main characteristics of NIOBE are summarized. NIOBE is a simulated MTR-type fuel assembly where coolant boiling can be investigated under various thermohydraulic circumstances in a nuclear reactor environment. This property makes NIOBE unique in its class. An example of parameter/anomaly monitoring, i.e., velocity profile monitoring in coolant channels, is introduced in Chapter 3 based on indications of thermocouples.

In Chapter 4, peculiarities of coolant boiling in narrow channels are studied by neutron noise methods. Chapters 5 and 6 contain results regarding parametric noise effects, such as the local field-of-view of self-powered neutron detectors (SPNDs), void fraction measurements, and subcooled boiling monitoring by SPNDs. In Chapter 7, low-frequency boiling effects are studied.

This thesis is based on results of experiments performed at the NIOBE loop located in a research reactor (HOR). But a great part of the conclusions is not restricted to research reactor applications only. It can be of interest to specialists working in the field of thermohydraulic parameter monitoring of various light water reactors.

Chapter 2

The NIOBE Facility

In this chapter, the main characteristics of NIOBE are given. First, the basic considerations are outlined which played a role in the design of the setup. This section is followed by the detailed description of the setup and its instrumentation. Finally, the experimental circumstances are characterised.

2.1 General Considerations

The aim of the experiments at NIOBE is to study boiling effects in the Hoger Onderwijs Reactor (HOR) of IRI without interrupting its normal operation schedule. HOR is a pool-type research reactor of 2 MWth power. It is fuelled with highly enriched uranium (93 wt%) located in the fuel plates of MTR-type assemblies. An MTR assembly consists of 19 fuel plates of 1.1 mm thickness each. The fuel assemblies have a 77 mm \times 81 mm rectangular cross-section and an active length of 625 mm. The main construction material of the core is aluminium. The reactor is controlled by 4 control rods. HOR is basically a water-reflected system, but it has a few BeO reflector elements as well. The exact number of the reflector elements depends on the actual core configuration. An example of the core configuration of HOR is shown in Fig. 2.1, with 25 fuel and 7 reflector elements.

The HOR reactor is located at the bottom of a 7 m deep pool. It is cooled by water which streams downwards through the core. The average velocity of coolant in the fuel assemblies of HOR is 50 cm/s.

The presence of coolant boiling in pool-type research reactors is considered an accidental situation. Therefore, boiling is induced not in the core

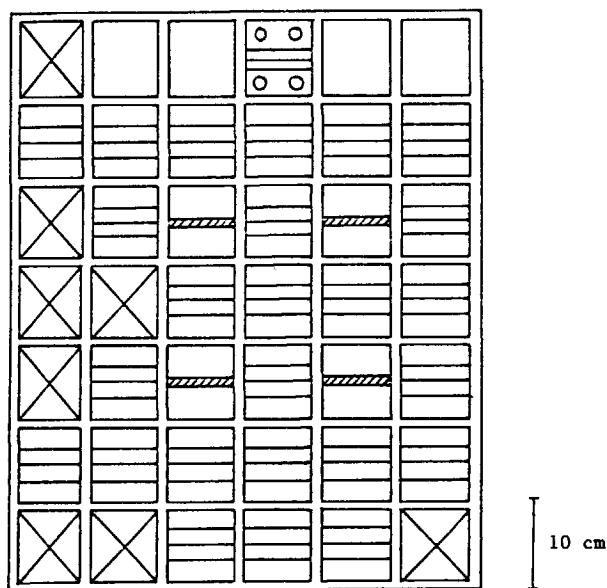
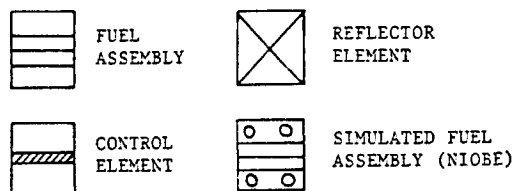


Figure 2.1: Map of the HOR core. NIOBE is located in the reflector region next to an actual MTR-type fuel assembly.
 The cross-section of a fuel assembly has dimensions 77 mm \times 81 mm.

itself but in an autonomous coolant loop which is fully separated from the main water volume of the reactor pool. This separated coolant loop includes a simulated MTR-type fuel assembly with outer dimensions being equal to those of an actual one. This feature allows the simulated assembly to be placed anywhere in the core of HOR to substitute us an actual fuel assembly. Due to safety reasons, however, NIOBE is found in the reflector region adjacent to an actual fuel assembly.

The coolant flow rate can be adjusted at NIOBE due to the presence of its autonomous coolant loop. Also, the heat flux at the fuel surface is a freely controllable variable because of the use of electrical heating at NIOBE instead of the nuclear heating of an actual MTR assembly. By varying the coolant flow rate and the heating power, different boiling conditions can be induced in the assembly. These features make NIOBE unique among facilities operating in a nuclear reactor environment.

In order to gather as much information as possible about the boiling process, NIOBE accomodates neutron detectors and thermocouples in the direct neighbourhood of the boiling region. To allow room for the instrumentation within the original dimensions of the assembly, the total number of fuel plates had to be decreased with respect to the original construction of an MTR element with 19 plates. Finally, a configuration with 3 plates has been realized at NIOBE.

2.2 Description of NIOBE

NIOBE consists of a simulated assembly, a circulation pump, two turbine flowmeters, and two valves. The coolant circuit is divided into two loops after the circulation pump. Each loop has its own turbine flowmeter and an electrically controlled valve which is located above the water level of the reactor basin. They are connected to the simulated assembly with the help of a set of 7 m long tubes.

The coolant arrives at the simulated assembly via two separate tubes. It flows downwards through coolant transport tubes inside the simulated assembly and enters a coolant channel. The first channel is found between fuel plates Nos. 1 and 2, the second being the one between plates Nos. 2 and 3. The axial cross-section of the assembly is depicted in Fig. 2.2.

At the inlet of the channel, the coolant passes through an orifice with a cross-section of $6.15 \text{ cm} \times 0.16 \text{ cm}$. Therefore, the flow suddenly expands

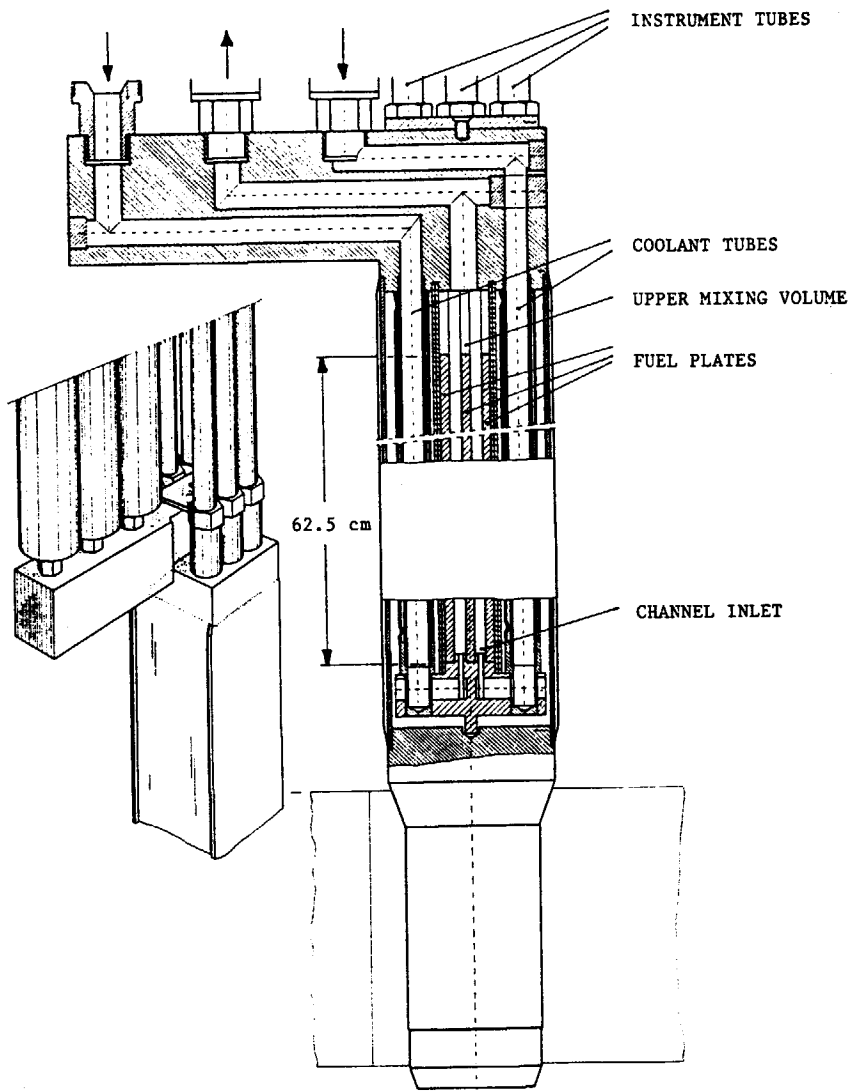


Figure 2.2: Axial cross-section of NIOBE. The length of each fuel plate is 625 mm.

when entering the channel. Due to this expansion, entrance effects are important in the coolant channels.

The coolant is heated up while streaming upwards between the plates. The two coolant channels join in a common upper mixing volume, and the coolant leaves the assembly in a single tube. The coolant is cooled by the surrounding water of the reactor pool when passing through the transport tubes after leaving the simulated assembly.

The maximum attainable mass velocity (in fact a mass flux density) is about $300 \text{ kg/m}^2\text{s}$ in each channel. Very low mass velocities are excluded from the present studies. Accordingly, a safety panel automatically switches off the setup as soon as mass velocities less than $60 \text{ kg/m}^2\text{s}$ have been detected by a flowmeter. The working range of the mass velocity was between $100 \text{ kg/m}^2\text{s}$ and $250 \text{ kg/m}^2\text{s}$ during the experiments. Experiments with low mass velocities (the nominal mass velocity at HOR is $500 \text{ kg/m}^2\text{s}$) can be used to analyse the cooling regime with natural convection at HOR or effects caused by partial channel blockage.

The simulated assembly has 3 aluminium fuel plates; the length of a plate is 625 mm, both in an actual and in the simulated assembly. The dimensions of the cooling channels are $61.5 \text{ mm} \times 5 \text{ mm}$, which differ from the channel sizes of the MTR assembly ($65 \text{ mm} \times 3 \text{ mm}$). The thickness of plates is significantly greater in the simulated assembly than in the actual case, 4 mm vs. 1.1 mm, because now the plates have to accommodate thermocoax heating wires of diameter 1.5 mm and thermocouples as well. The heating wires are placed in the plates in a special pattern so that the electrical heating power approximates a cosine shaped distribution in axial direction. By applying this special power shape, the effect of the neutron flux distribution in a homogeneous bare reactor in axial direction is simulated.

It must be noted that the actual neutron flux distribution in the HOR is not cosine shaped. Two major reasons can be indicated which deform the cosine shape: the reflector effect and the presence of control rods. The core of the HOR is reflected by water in an axial direction, and the neutron flux shape is influenced by the reflector close to the top and to the bottom of the core. Moreover, HOR is controlled by 4 control rods which are inserted into the core from the top. The control rods are strong absorbers of neutrons; therefore the neutron flux has a bottom-peaked shape. This shape changes in time, as the control rods are continuously removed from the core to compensate for the reactivity decrease caused by the burnup of the fuel. By applying a cosine shaped power profile at NIOBE, these effects are neglected.

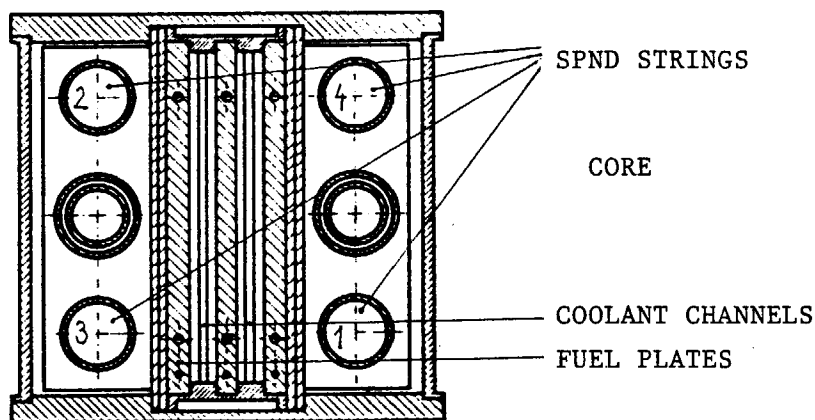


Figure 2.3: Radial cross-section of NIOBE. Dimensions of the cross-section are 77 mm \times 81 mm.

The concession of using electrically heated plates means that thermohydraulic feedback effects are completely absent at NIOBE, i.e., temperature and void effects have no influence on the dominant (electrical) heat production.

The experimental assembly is equipped with 4 strings of self-powered neutron detectors (SPNDs) located in instrument tubes next to the fuel plates (see Fig. 2.3). Each SPND has a Cd-Mg emitter of 3 mm diameter and of 20 mm length insulated from the stainless steel sheaths of the detector. An electric current is generated in the emitter due to (n, γ) capture followed by the absorption of the produced electrons in the sheath. This SPND has been designed for and successfully utilized in neutron noise measurements [Kle81a]. Each string has two SPNDs at a fixed distance. The effective distance between the detectors of strings 1 to 4 are 100 mm, 250 mm, 140 mm, and 100 mm, respectively. The SPND strings are movable in axial direction. Each string includes γ -detectors (SPGDs) as well. Due to the frequent failure of SPGDs, however, the analysis of SPGD signals is not included in the present work.

The temperature of the fuel plates is measured by chromel-alumel thermocouples (TCs) of 0.5 mm diameter which are built into the plates with an explosive welding technique to assure excellent thermal contact between the TCs and the plate material. Each plate has 5 TCs. Some of the TCs are broken, but signals of 6 TCs were available for noise analysis. These are

TC 1.2, TC 1.5, TC 2.3, TC 3.2, TC 3.3, and TC 3.5. The first number indicates the plate; the second stands for the axial position. TCs 1.2 and 3.2 are located at axial elevation 22.2 cm measured from the channel inlet; the elevation is 31.2 cm, 40.2 cm, and 53.2 cm for TCs at the 3rd, 4th, and 5th elevations, respectively. There is a TC at the exit of both channels which measures the coolant temperature.

The heating power of the plates can be adjusted continuously or step-wise with a maximum of 7 kW per plate. This value is close to the 7.2 kW per plate maximum at HOR operating at nominal power of 2 MW. In order to exclude the possibility of burnout of the fuel plates (which could occur at the combination of low flow rates and high heating powers), the safety panel of the setup switches off the setup if a temperature of 150 °C or more is indicated by any of the TCs in the channel walls.

Special measures were taken to reduce heat losses, caused by the large temperature difference between NIOBE and the surrounding water. Temperatures can reach or exceed 100 °C in the assembly, while the pool water has a temperature of 30 - 40 °C. There is Contimet-35 isolation next to both side plates. Contimet-35 is an alloy of metallic titanium and small amounts of Fe, C, and other elements. Its heat conductivity is low; $k_{contimet} = 12.3 \text{ W/mK}$. The plates are fixed in the assembly in a special manner to minimize the contact surface between the plates and the wall of the assembly.

A measured detector signal is divided into an average component which is constant in time and a time-dependent fluctuating part which has zero average value. The applied cadmium SPNDs are sensitive to neutron flux fluctuations up to high frequencies ($\sim 50 \text{ Hz}$ or more) due to their prompt responding character. The working frequency range of the TCs extends up to $\sim 5 \text{ Hz}$. The statistical properties of these fluctuations have been analysed by various noise methods in order to gain information about the thermohydraulic state of the coolant at NIOBE.

2.3 Thermohydraulic state of the coolant

In this section, characterisation of the mean thermohydraulic parameters of NIOBE under various steady-state experimental conditions is given. These conditions cover most of the experiments at NIOBE. In some cases, when non-stationarity of the processes becomes essential, additional considerations are necessary; see Section 6.6 in Chapter 6.

Generally speaking, the thermohydraulic state of the coolant is described

by the mass-, momentum-, and energy-conservation equations. By averaging the 3-dimensional local equations across the channel cross-section, a system of one-dimensional equations will be obtained for the coolant [Del77] with the pressure, the velocity, and the internal energy of the coolant as state variables.

In the case of NIOBE, the system of steady-state conservation equations can be reduced significantly. The mass velocity is kept constant in both channels during each experiment, thus the mass conservation is fulfilled automatically. The gravitational pressure drop along the channels of NIOBE (0.06 bar) is much greater than the frictional acceleration and entrance/exit losses because of the small velocities ($v \ll 1\text{m/s}$) [Nab89]. In the case of steady-state, the changes of the energy of the coolant caused by pressure variations are negligible compared to the convective heat transfer at the channel walls. So, pressure can be omitted as a separate state-variable. Parametric dependence on pressure, of course, is still preserved. Now, the coolant state is described by the following energy balance equation:

$$\frac{\partial}{\partial z}(\rho_c(z)v_c(z)u_c(z)) = Q(z) + S(z). \quad (2.1)$$

Here $Q(z)$ is the heating power entering the coolant through the walls per unit coolant volume, and $S(z)$ is the direct heat production in unit coolant volume (nuclear heating from the HOR). The subscript c stands for coolant, while ρ , v , and u denote the density, velocity, and full energy, respectively. The total energy of the coolant can be approximated by the enthalpy, h_c , for not extremely high velocities. Then the energy equation becomes:

$$\rho_c(z)v_c(z)\frac{\partial}{\partial z}h_c(z) + h_c(z)\frac{\partial}{\partial z}(\rho_c(z)v_c(z)) = Q(z) + S(z). \quad (2.2)$$

Taking into account that the mass velocity is constant during an experiment, the second term on the left side of the above equation can be omitted. Based on Eq. (2.2), the enthalpy of the coolant can be determined at any axial elevation if the inlet enthalpy and heat source terms $Q(z)$ and $S(z)$ are known. Further on, the above factors will be analysed.

2.3.1 Heat losses

The total heat generated in the heating wires is known within an accuracy of 0.3 % determined by the error of measuring the voltage and current. One has to take into account, however, that not all of this heat enters the coolant.

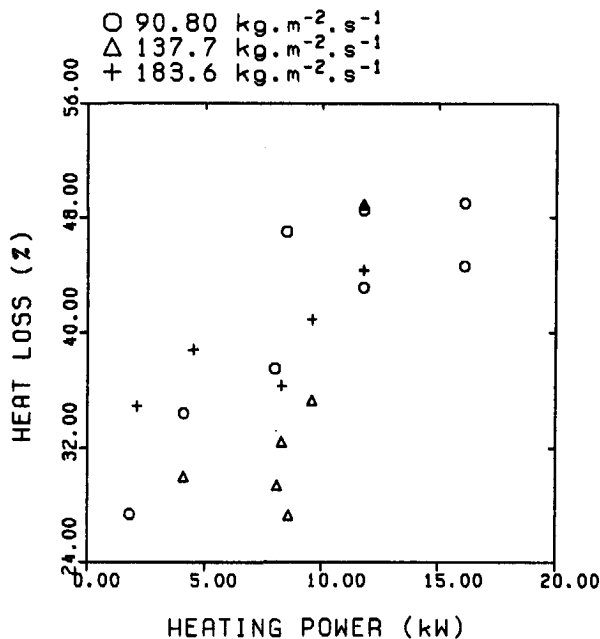


Figure 2.4: Heat losses at NIOBE vs. total heating power at different mass velocities.

Part of the developed heat is conducted to the outer walls of NIOBE by the fuel plates and transferred into the surrounding water; there are heat losses from the coolant through the unheated channel walls as well, etc. The determination of heat losses is not possible in a straightforward way, simply by comparing the outlet and inlet enthalpies of the coolant, because of the absence of TCs in the coolant at the channel inlets. Nevertheless, the heat losses are estimated on the basis of a series of experiments designed for this purpose by making use of additional TCs, which have been pushed to the bottom of the 7 m long coolant transport tubes. The results are introduced in Fig. 2.4 for 3 mass velocities at various heating powers. Heat losses vary between 27 % and 48 % of the total heating power. There is a tendency of increasing heat losses with increasing power. At 16 kW, the heat loss reaches 48 % of the total heating power. The relative error of the heat losses varies between 5 % and 15 % and is dominated by the error of the temperature measurement. Due to the high values of heat losses and the limitations of the power unit, the average coolant enthalpy does not reach saturation during experiments at NIOBE, and coolant boiling remains subcooled even at the highest heating powers.

2.3.2 Nuclear heating

The significance of the heat coming from the HOR has been determined by comparing temperatures with the HOR in operation and without HOR heating. The amount of heat originating from the HOR has been found to be (0.75 ± 0.05) kW among different operation conditions at NIOBE. This value is small but not negligible, especially at low heating powers. It is taken into account, together with heat losses, as a correction factor when evaluating the effective heat source term for each experiment.

2.3.3 Fuel-to-coolant heat transfer

Let us consider now the heat transferred from the fuel to the coolant and denote q''_{fl} the heat flux density at the surface of the fuel plate. In the case of single-phase flow, q''_{fl} equals the single-phase forced convection heat flux density q''_{FC} given by

$$q''_{FC} = h_{FC} \{T_W(z) - T_C(z)\} \quad (2.3)$$

According to the actual values of the Reynolds number, $2900 < Re < 8000$, there are transitional and turbulent flows at NIOBE. In this case, the forced convection heat transfer is calculated by the modified Dittus-Boelter correlation [Bjo82]

$$Nu = 0.023 Re^{0.8} Pr^{0.3} \quad (2.4)$$

Turning to boiling phenomena, several definitions have to be introduced. The development of boiling along a channel is depicted schematically in Fig. 2.5, where 3 main regions are indicated: single-phase forced convection, subcooled boiling, and saturated boiling. No vapour phase is present at the forced convection region, and the heat transfer is described by Eq. (2.4). When the surface temperature reaches a certain level above the local saturation temperature of the coolant, bubbles start to form on the surface. The start of bubble generation is marked by the point of onset of nucleate boiling (ONB). The relation between wall superheat, $\Delta T_{sat} = T_W - T_S$, and heat flux density at the wall at ONB is given by the Bergles-Rohsenow relation [Ber64]

$$q''_{ONB} = 1.1 p^{1.156} (1.8 \Delta T_{sat})^{\frac{2.16}{0.00234}}, \quad (2.5)$$

where p is the coolant pressure. In highly subcooled flows, bubbles either condense at the position of their birth or they move in the thermal boundary layer and condense in the direct neighbourhood of the wall (wall voidage).

Bubbles enter the subcooled central flow region when the point of net vapour generation (NVG) is reached, and rapid growth of the steam phase starts. Saturated boiling begins when the temperature of the main coolant volume reaches saturation, and thermal equilibrium has been established.

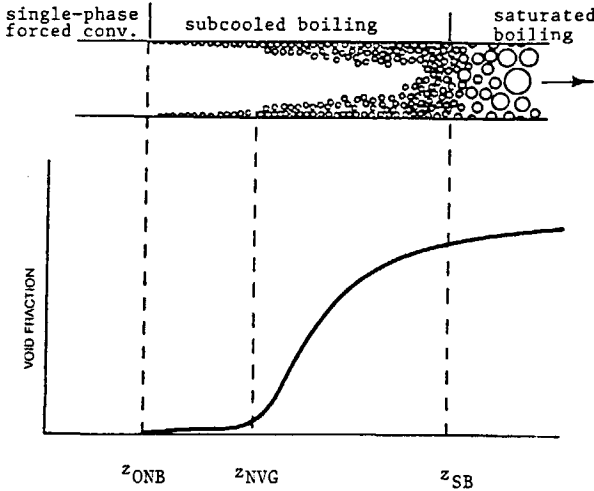


Figure 2.5: Boiling regions along a heated coolant channel; notations: ONB - onset of nucleate boiling; NVG - net void generation; SB - saturated boiling

The heat transfer becomes more intensive after the incipience of boiling due to the growth and collapse of steam bubbles in the subcooled flow. In the case of fully developed nucleate boiling (FDNB), the Jens - Lottes relation [Roh85] will be used for the description of the heat transfer:

$$q''_{FDNB} = \exp\left(-\frac{4p}{61.245}\right)\left(\frac{\Delta T_{sat}}{0.792}\right)^4 \cdot 10^{-3} \quad (2.6)$$

In the transition region between single phase convection and fully developed nucleate boiling, various methods are used for the evaluation of the heat transfer coefficient. In the method proposed by Bergles and Rohsenow, an interpolation is used between the ONB and FDNB points of the boiling curves.

There are significant discrepancies between the ONB and FDNB relations given in the literature for general use (independently of the actual geometry of the channel) and the experimental results in the case of boiling

of a coolant in thin rectangular channels under low velocity circumstances [Bel88], [Sud86], [Bel91]. According to these results, Eq. (2.5) may over- or underestimate q''_{ONB} , while Eq. (2.6) usually overestimates q''_{FDNB} . It is suggested that the channel width must appear explicitly in the correlations in the case of thin channels. Such discrepancies have been observed in our experiments as well.

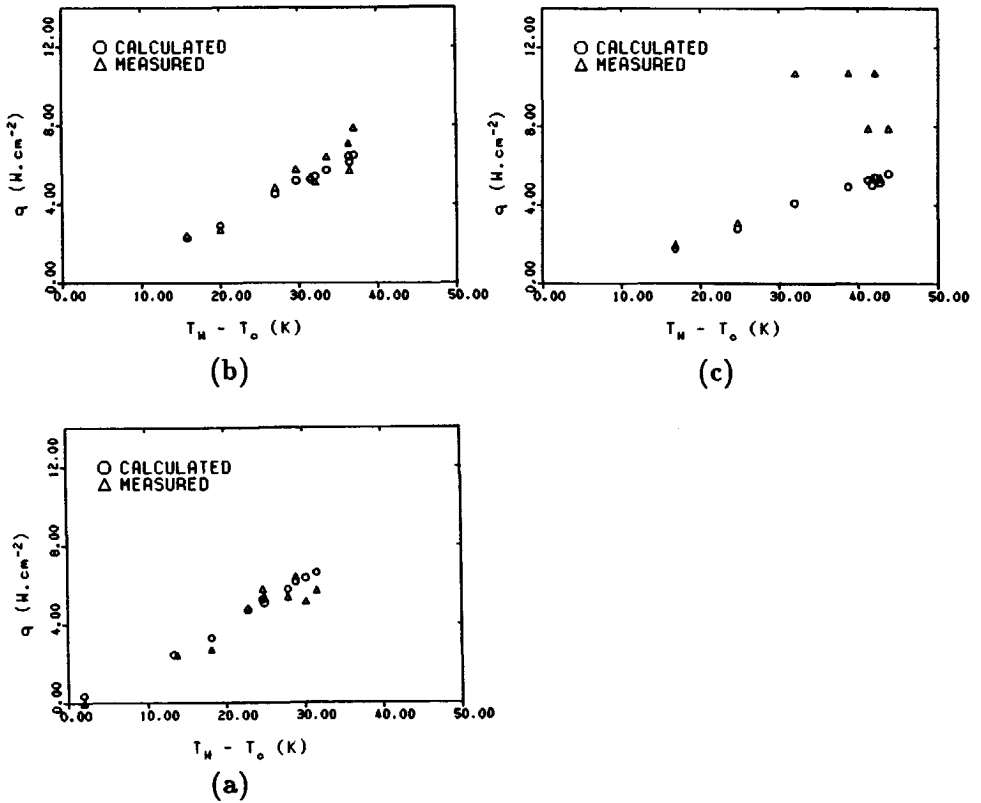


Figure 2.6: Heat flux density as a function of $T_W - T_c$.

Black squares denote heat flux densities calculated by Eq. (2.4) for given mass velocities; diamonds are measurement points. The mass velocities are (a) $183.6 \text{ kg/m}^2\text{s}$, (b) $137.7 \text{ kg/m}^2\text{s}$, (c) $90.8 \text{ kg/m}^2\text{s}$.

The relationship between $\Delta T_{sub} = T_W - T_c$ and the local heat flux density at the surface of the wall is depicted in Fig. 2.6 for different mass velocities at NIOBE. T_W is estimated by the temperature measured by TCs in the plates, usually by TC 2.3 located at half the height of the middle-plate. The error

introduced by this estimation is less than 1°C during the experiments with constant parameters according to results of a numerical study summarized later in this chapter. The theoretical value of q''_{FC} is determined from Eq. (2.3) for given T_{IV} and T_c values, and it is also depicted in Fig. 2.6. Coolant temperatures are evaluated from the heat balance by making use of the actual values of heat sources/losses, measured outlet enthalpy, and mass velocity.

The indications of the TCs have an uncertainty of 0.5°C . The error of the heat loss evaluation yields 5 % error of ΔT_{sat} . As a result, the error of ΔT_{sat} varies between 3°C and 4°C . Taking into account this relatively large inaccuracy of the measurements, the correspondance between measurements and the calculated forced convection points is considered to be satisfactory for heat flux densities of up to $\sim 6 \text{ W/cm}^2$. The difference between the measured and calculated heat flux densities above 6 W/cm^2 is large, and it cannot be attributed to measurement errors. The actual heat flux densities exceed the forced convection component in a consistent manner.

Further information can be gained from the measured boiling curves given in Fig. 2.7, where also the forced convection curves are shown for 3 mass velocities. Curves FC128, FC137, and FC90 do not correspond to constant coolant temperatures, and they are given just to indicate the position of the forced convection points at each experiment. In Fig. 2.7, the ONB and FDNB curves are drawn as well, which are calculated by Eq. (2.5) and Eq. (2.6), respectively. It can be concluded that coolant boiling starts at NIOBE if the wall superheat is greater than about 3°C . This conclusion explains the deviation from the forced convection regime observed in Fig. 2.6, because the points with heat flux densities above 6 W/cm^2 at mass velocities of $90.8 \text{ kg/m}^2\text{s}$ and $137.7 \text{ kg/m}^2\text{s}$ indeed belong to states with $\Delta T_{sat} > 3^{\circ}\text{C}$.

2.3.4 Temperature distribution in the plates

The heat is generated in the fuel plates by thermocoax heating wires. It is expected that, due to the large heat conductivity of Al, $k_{Al} = 240 \text{ W/mK}$, the microstructure of the temperature distribution along the plate surface is rather uniform and has no peaks in the direct neighbourhood of the wires [VMe84]. Calculations have been performed to evaluate the actual temperature distribution in the plate around the wire. In this way, the difference between the indication of TCs (inside the plates) and the actual surface temperatures can be estimated.

The heat diffusion equation has been solved in X-Y geometry shown in

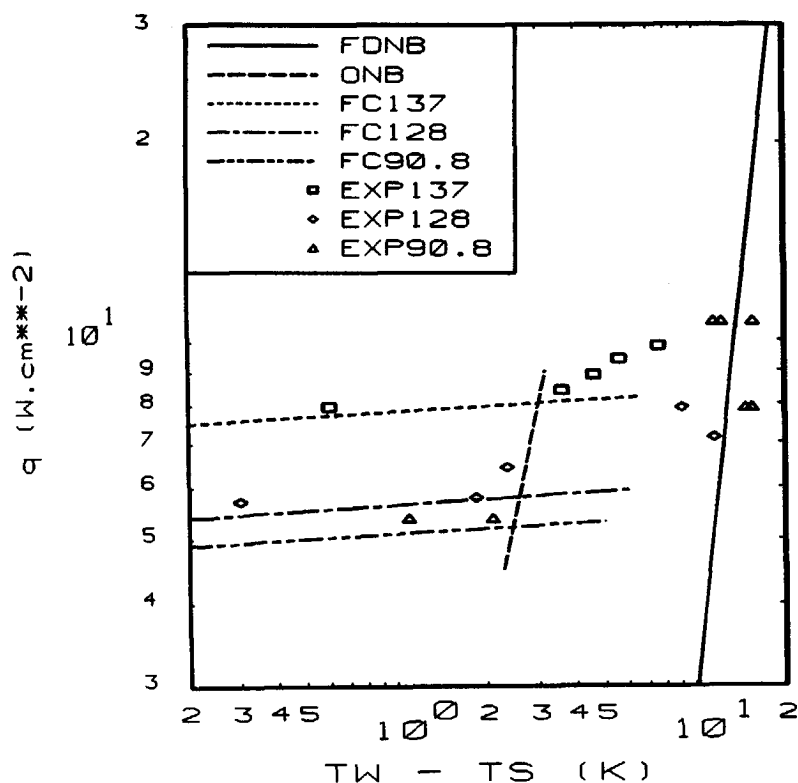


Figure 2.7: Boiling curves at NIOBE at different mass velocities. FDNB : fully-developed nucleate boiling curve according to Jens-Lottes [Roh85]; ONB : onset of nucleate boiling curve according to Bergles-Rohsenow [Ber64]. Curves FC128, FC137, and FC90.8 mark the positions of the points belonging to single-phase forced convection conditions (calculations). The measured points are given by squares ($137 \text{ kg/m}^2\text{s}$), diamonds ($128 \text{ kg/m}^2\text{s}$), and triangles ($90.8 \text{ kg/m}^2\text{s}$).

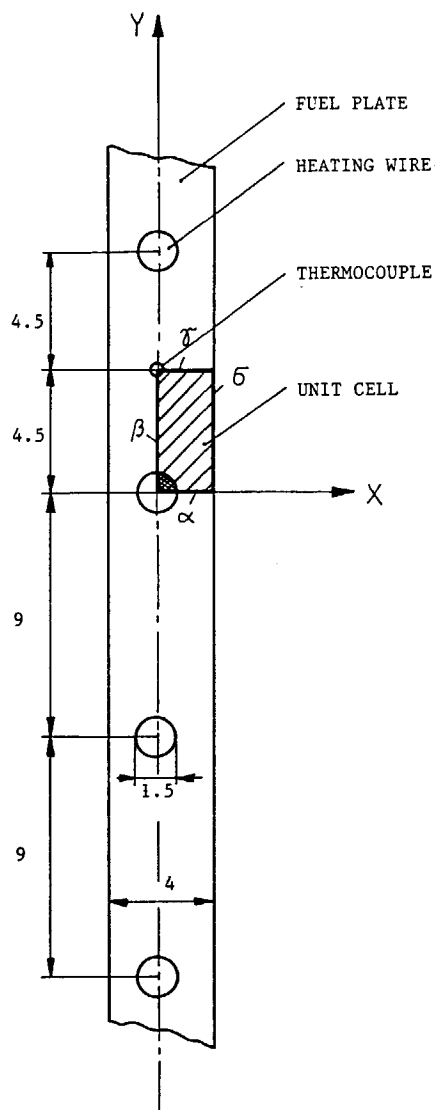


Figure 2.8: Geometry of the 2D heat diffusion problem. All dimensions are in mm.

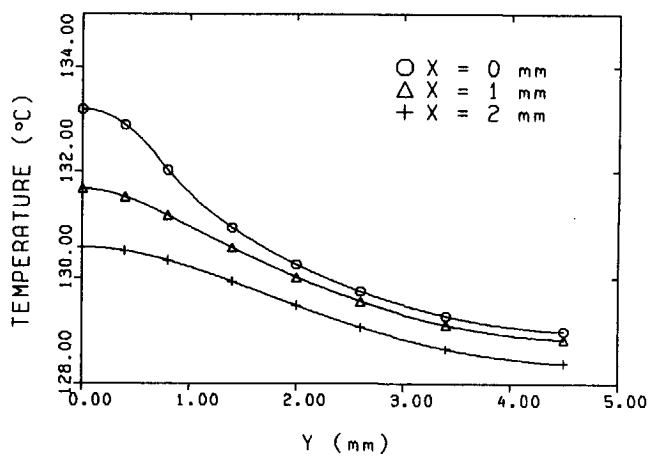
Fig. 2.8. The width of the plate, which is 65 mm in the actual case, is assumed to be infinite in the model. The dimensions of the unit cell are determined by the half thickness of the plate (2 mm) on the one hand, and by the half distance (4.5 mm) between two parallel wire segment in the regions with the highest wire density on the other hand. The heat source term is uniformly distributed in the quarter circle segment that corresponds to the heating wire in the unit cell. Based on symmetry considerations, no heat transfer is allowed at the boundaries inside the plate (boundaries α , β , δ , and γ). At surface σ_1 , both Dirichlet ($T_{\sigma_1} = \text{const.} = 133^\circ\text{C}$) and Neumann ($\text{grad}T|_{\sigma_1} = \text{const.} = -5.4 \text{ W/cm}^2$) conditions are considered. The results given in Figs. 2.9a-b represent the temperature distribution in a fuel plate in the region with the highest power densities.

The maximum temperature difference along the surface in the neighbourhood of a wire is 2°C for the Neumann problem. In the experiments, $\Delta T_{sub} = T_w - T_c$ varies between 20°C and 50°C . A 2°C increase in the plate temperature means about 10 % increase in ΔT_{sub} at constant coolant temperature (conservative estimation!). Assuming constant heat transfer coefficient, the heat flux density increases by 10 %, due to $q''_{FC} \sim \Delta T_{sub}$. In most experiments, ΔT_{sub} is larger than 20°C , and the local peaking of the heat flux density constitutes less than 10 % of the nominal value. Consequently, the Neumann condition is a good approximation of reality in the case of single-phase heat transfer.

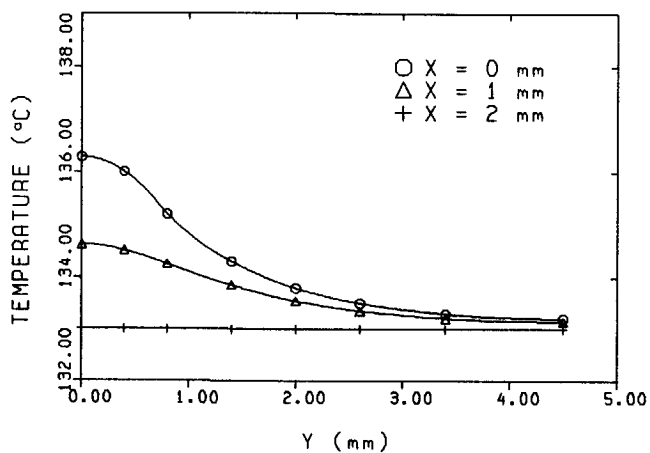
According to Figs. 2.9a-b, the temperature at the TC position differs from the surface temperatures by 0.2°C (Dirichlet condition) to 0.6°C (Neumann condition). In the evaluation of the experiments, a value of 1°C will be used as an estimation of the maximum difference between the surface temperatures and TC indications.

The role of small temperature differences becomes more significant during coolant boiling. At boiling heat transfer, $\Delta T_{sat} = T_w - T_s$ is of importance. It varies between 3°C and 15°C . The dependence of q'' on ΔT_{sat} follows a power law with increasing exponent. It starts with the 2nd power at ONB and ends with the 4th power at FDNB conditions. Accordingly, the peaking factor of the heat flux density increases at boiling, and it can reach or exceed a value of 2.

It can be concluded that the temperature distribution around the heating wire is rather uniform in the case of single-phase flows, and the TCs in the plates give a good estimation of the surface temperatures within an error of 1°C . The heat flux density is approximately uniform at the surface in the case of single-phase flow. Distortions occur in the microstructure of



(a)



(b)

Figure 2.9: Calculated temperature distribution in the fuel plates; (a) Neumann condition; (b) Dirichlet condition. The thermocouple is located at position 4.5 mm along the y-axis; the heating wire is at 0 mm.

the heat flux density during boiling, resulting in periodic maxima in the neighbourhood of the heating wires.

2.4 Neutron flux perturbations at NIOBE

Changes in the thermohydraulic state of the coolant in the channels of NIOBE lead to changes in the neutron flux of HOR as well. In this section, stationary neutronic effects will be calculated. In the analysis, multi-group neutron diffusion equations are used. This system of equations is written for G energy groups without external noise sources (see Nomenclature for notations):

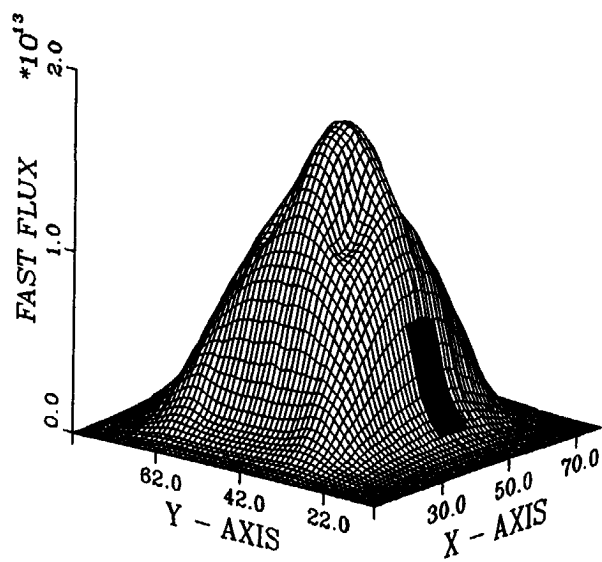
$$-\nabla D_g \nabla \Phi_g + \Sigma_{tg} \Phi_g(\mathbf{r}) = \sum_{g'=1}^G \Sigma_{sg' \rightarrow g} \Phi_{g'} + \frac{\chi_g}{k} \sum_{g'=1}^G \nu_{g'} \Sigma_{fg'} \Phi_{g'} \quad (2.7)$$

where g is the energy group number, ($g = 1, 2, \dots, G$). The operator form of Eq. (2.7) is written:

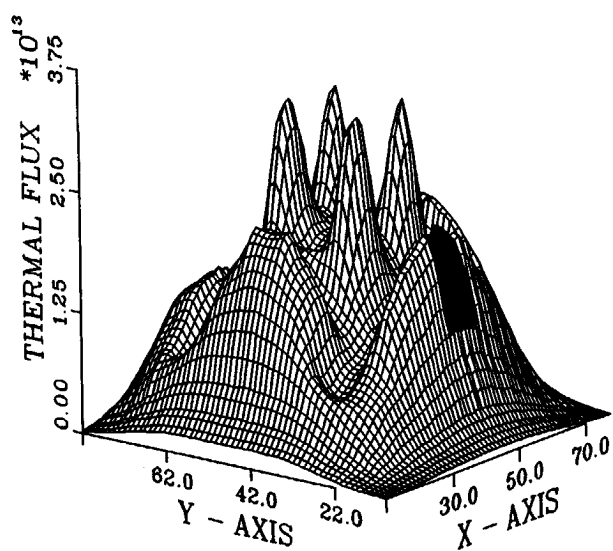
$$\mathcal{M} \underline{\Phi} = \frac{1}{k} \mathcal{F} \underline{\Phi}, \quad (2.8)$$

where $\underline{\Phi}$ is the vector of group flux densities, and \mathcal{M} and \mathcal{F} are the diffusion and fission operators, respectively. In the forthcoming considerations, we use the term neutron flux instead of neutron flux density [Dud76]. After specifying proper boundary conditions, e.g., zero fluxes at the extrapolated boundaries, an eigenvalue problem for k is obtained. This problem has been solved for HOR with the help of the CITATION diffusion code [Fow71] for two-dimensional slab geometry. Calculations have been performed with different amounts of a homogeneously distributed void fraction in the coolant channels of NIOBE, which correspond to different levels of boiling.

In the calculations, the assembly was assumed to be in the reflector at the actual position of the NIOBE. The calculated fast and thermal neutron flux are shown in Figs. 2.10a-b. The thermal flux has peaks in the reflector region around the reactor. There are 4 peaks inside the core region as well. Those are due to the water gaps at the positions of the withdrawn control assemblies. The location of NIOBE is marked by a black square, and it is given by x-coordinates 43.2 to 50.9 cm and by y-coordinates 20.0 to 28.1 cm. In other words, NIOBE is found in the reflector peak. Closer inspection shows that SPND strings 1 and 4 are on the inner side of the peak (closer to the reactor), while strings 2 and 3 are on the outer side of this peak.



(a)



(b)

Figure 2.10: Calculated fast (a) and thermal (b) neutron fluxes at HOR. The position of NIOBE is marked by a black square.

In Fig. 2.11, the calculated thermal neutron flux is shown across the NIOBE as a function of the average void fraction. The coolant channels are located between positions 23.1 cm and 23.6 cm, and 24.0 cm and 24.5 cm. The instrument tubes are found between 21.0 cm and 22.0 cm, and 25.5 cm and 26.5 cm, respectively.

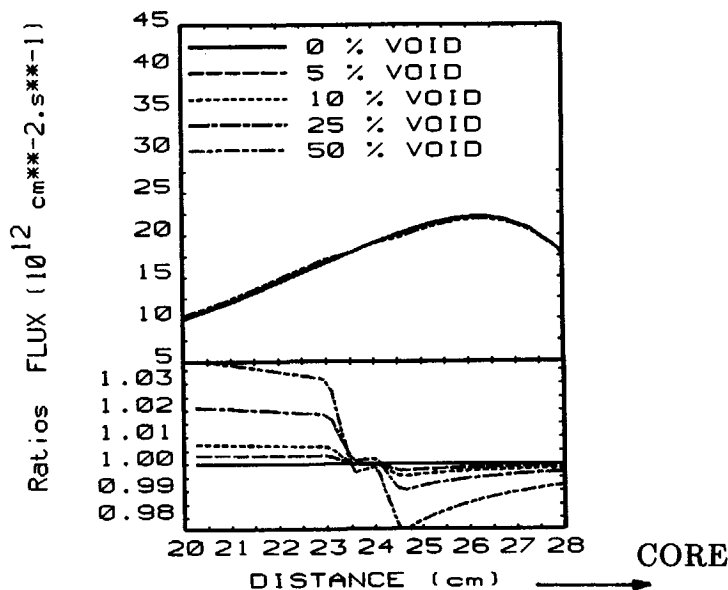


Figure 2.11: Thermal neutron flux at different void fractions in NIOBE; calculations by code CITATION.

On the lower figure, the relative change of the neutron flux with respect to the case without boiling (0 % void) is given.

There is a negative void coefficient for string 4, but calculations indicate a positive void effect at the position of string 3. The magnitude of the relative neutron flux variation at the detector positions may reach a few percent, depending on the actual void content. We observe a spatial relaxation at detector string 4. At the same time, the positive effect at string 3 is remarkably constant inside NIOBE.

The occurrence of positive void effects is a consequence of the actual location of the assembly in the reflector and can be explained as follows [Kle79]. In the core region, the main void effect is caused by changes in the moderation cross-section. If the void fraction increases, the amount of the moderator decreases; therefore the thermal flux becomes lower. The situa-

tion is changing at the core-reflector interface and in the reflector where the neutron current is large due to radial leakage from the core. In this situation, the spatial arrangement of the boiling region, the neutron detector, and the source of neutrons (now the reflector peak works as an effective neutron source) determine the sign of the measured effect. Decreasing coolant density may cause: (a) positive void effect (i.e. increasing neutron flux) if the void region is located between the detector and the neutron source, or (b) a negative void effect (i.e., decreasing neutron flux) when the void is found at the other side of either of them. We have case (a) for strings 2 and 3 and case (b) for strings 1 and 4.

The uncertainty of the neutron flux measurement by SPNDs varies between $\pm 0.3\%$ and $\pm 1\%$. This error is due to the error of measuring the detector current and to the fluctuations of the neutron flux itself. Therefore, no measurable neutron flux level variations are expected in experiments with void fractions below ~ 5 to 10% , i.e., in experiments with an onset of nucleate boiling and low-void subcooled boiling. At higher void fractions, detectable DC effects must occur. Indeed, neutron flux changes exceeding 1% have been detected in experiments with the highest powers (see Chapter 4).

Consider now reactivity effects caused by the operation of NIOBE. The calculated void reactivity coefficient is -0.03 pcm per cm^3 of void in NIOBE. This means that 50% voidage in the 2 coolant channels of NIOBE yields -5.9 pcm reactivity variation. Note: 1 pcm (per cent mille) means a reactivity of 10^{-5} .

The core regulation system of HOR acts as follows in response to this reactivity decrease. The HOR has 4 control rods which respond to the signals of ionisation chambers located around the reactor core. Three out of the 4 control rods are at a fixed position during stationary operation. One of them is in automatic control mode. The magnitude of the control rod movement upon a given reactivity perturbation depends on the position of the rod. The control rod worth is highest at about half the height of the core, and it decreases while approaching the boundary of the core. Based on the control rod importance curves of HOR [Sti91], the maximum rod movement needed to compensate 5.9 pcm reactivity decrease is 3 mm when the control rod is close to the top of the core. This is a small movement, but it can be detected by closer investigation of the operation data file.

It is concluded that changes in the average neutron flux caused by boiling at NIOBE cannot serve as a tool for boiling indication during experiments with low void fraction. Detectable variations of the average signal level occur

only at experiments with intensive boiling (highest heating powers).

2.5 Summary of Main Features of NIOBE

1. Boiling effects in an MTR-type fuel assembly can be investigated experimentally at NIOBE. Different types of subcooled boiling were induced in the coolant channels of NIOBE. In experiments with the highest heating powers, temperatures in the plates indicate coolant states which are close to fully developed nucleate boiling. Saturated boiling cannot be reached at NIOBE due to large heat losses and limited power supply.
2. The influence of actual coolant boiling on the neutron flux can be investigated at NIOBE by SPNDs close to the boiling region. Thermocouples in the fuel plates are used for direct monitoring of thermohydraulic processes at NIOBE.
3. Variations of the average signal level of the available neutron detectors due to boiling at NIOBE are negligible except for experiments with the highest heating powers.
4. The location of NIOBE in the reflector gives rise to some special neutronic effects, e.g., a significant neutron current caused by large gradients of the neutron flux and a possible positive local void effect on the neutron detector signals. These features will be taken into account in the interpretation of the measurements.

Chapter 3

Flow Measurements Using Noise Signals of Axially Displaced Thermocouples†

Results of flow measurements using axially displaced thermocouples in the channel wall are introduced. It has been found that the velocities obtained via temperature noise correlation methods are significantly larger than the area-averaged velocity in the single-phase coolant flow. Model calculations show that the observed phenomenon can be attributed to the effects caused by the radial velocity distribution in the channel.

3.1 Introduction

Determination of the flow rate of the coolant in the channels of nuclear reactors is an important task of core monitoring. It is usually impossible to measure the flow by flowmeters in the individual channels due to lack of space and safety reasons. An alternative method of flow measurements is based on the analysis of noise signals of the available in-core detectors. In noise methods, a transit time, which characterises the propagation of thermohydraulic fluctuations (density or temperature fluctuations) in the coolant, is determined from the correlation between the noise signals of axially displaced detectors.

†This Chapter is a slightly adapted version of the article "Flow Measurements Using Noise Signals of Axially Displaced TCs" by R. Kozma, J.E. Hoogenboom, *Annals of Nuclear Energy*, Vol 17,p.493(1990)

Neutron noise analysis proved to be useful for flow monitoring in boiling water reactors (BWR), where coolant density fluctuations have a significant effect on the noise signals of in-core neutron detectors. Good agreement between the velocity inferred from neutron noise measurements and the theoretically expected void propagation velocity was reported in different studies [Wac73], [Sei73]. A second velocity has been found in other experiments [Kos77], [Beh81], [Fed82]. The interpretation of the latter results needed more involved models [Beh83]. Further experimental and theoretical analysis helped to reveal the physical meaning of the inferred velocities [Lub83a], [Lub84], [Ana84]. It has been pointed out that usually the area-averaged velocity is not measured by neutron detectors.

Also, noise signals of thermocouples (TC) displaced along a coolant channel can be used for flow measurements. A TC which is located in the streaming coolant can be regarded as a local probe, i.e., it measures temperature fluctuations which reach its location.

It has been shown in an earlier version of NIOBE that also TCs in the channel wall (out-of-stream TCs) can be used for flow velocity determination [VMe85]. Coolant temperature fluctuations entering the channel wall attenuate in the wall material. This attenuation is the same for both thermocouples. One can investigate thermohydraulic processes in the coolant using TCs in the plates if the attenuated signals at the TC positions are larger than the background electronic noise of the TCs. This condition is satisfied in the mentioned experiment of Van Meulenbroek and Van de Wakker, due to the excellent contact between the TCs and the plate material.

The usefulness of the flow determination method using out-of-stream TCs has been demonstrated in an out-of-core experimental setup in the case of one-phase coolant, where the flow in the channel between two plates has been monitored simultaneously by a rotameter, by temperature noise correlation methods, and also via light transmission measurements using spy-glasses in the channel wall [VMe84]. In the experiment, the width of the channel was 3 mm. Velocities obtained via the different measuring methods agreed well with each other, especially at higher flow rates. In the case of flows with Reynolds number $Re > 2000$, the difference between the various velocities was less than 5 %.

In this chapter, the results of temperature noise measurements performed in the framework of the NIOBE project using out-of-stream TCs will be introduced. During the experiments, the coolant flow in the individual channels can be measured by flowmeters and TCs in the channel wall as well. Our experiments indicate large discrepancies between velocities measured

by flowmeters and velocities inferred from temperature noise in the case of single-phase coolant. It was found that the flow rate inferred from noise measurements exceeds the value determined on the basis of the flowmeter indication by about 15-20 %. The origin of this discrepancy will be analysed in the second part of this chapter.

3.2 Experimental conditions

Experiments with various flow rates and heating powers have been performed at NIOBE. At low flow rates and heatings, the coherences between the temperature noise signals are very low, and noise correlation measurements cannot be performed with the proper accuracy. High heating powers lead to coolant temperatures close to saturation, and in certain parts of the channels, coolant boiling occurs. Coolant boiling certainly influences the velocity field. The coherence between out-of-stream TC signals decreases with the onset of boiling in the channels, and the velocity measurements based on temperature noise correlation becomes less accurate. In this chapter, only the measurements with one-phase coolant flow are introduced.

TABLE I
Parameters of the experiments

Experiment	V_{fm} ℓ/h	P $kW/plate$	\bar{T} $^{\circ}C$	v_F cm/s	Δv_F cm/s
A	200	2.8	95	18.70	1.12
B	200	1.4	68	18.57	1.12
C	150	2.8	100	14.07	0.84
D	150	1.4	71	13.92	0.84

Parameters of the experiments A, B, C, and D, to be investigated in the present study, are given in Table I. The notations are: V_{fm} is the volumetric flow indicated by rotameters; P is the heating power; \bar{T} is the average coolant temperature in the upper region of the channels; v_F is the average coolant velocity determined from the measured flow rate. Details of the evaluation of v_F and its error, Δv_F , will be discussed below.

Both loops have a turbine flowmeter of type Bestobell M2/0500/B1. The flowmeters measure the volumetric flow (in ℓ/h), so the cross-sectional averaged coolant flow velocity in the channels can be evaluated. Two corrections have to be done with respect to the indication of the flowmeters to obtain the right velocity values in the channels. The first accounts for the changing

coolant temperatures at the positions of the flowmeters ranging from 55 °C to 85°C. Calibration experiments show that the flow rate is underestimated when the reference (20 °C) calibration constant is used at higher temperatures. The order of the underestimation is 1-2 %. The actual flow rate can be evaluated using the temperature-dependent correction factor $k_\nu(T)$. In the range of the parameters of the present experiments, however, its value can be approximated as $k_\nu = 1.017 \pm 0.002$.

The temperature of the coolant is higher in the simulated assembly than at the flowmeter. This increase in temperature leads to thermal expansion of the coolant. The value of the thermal expansion coefficient (k_p) is defined as the ratio of the coolant densities at the pump and in the simulated assembly. In the present experiments, its value varies from 1.008 to 1.020.

Using the obtained corrections, the cross-section averaged velocity v_F in the upper half of the cooling channels was calculated as $v_F = k_\nu k_p V_{fm} / 3.6A$, where A is the channel cross-section area in cm^2 , v_G is the average velocity in cm/s , and 3.6 is a conversion factor. The error of the average velocity, Δv_F , has been evaluated by taking into account the errors of the flowmeter indication, the corrections and the geometric dimensions. Its value is $\Delta v_F = 0.06v_F$. The relative error of the velocity determination is dominated by the uncertainty in linear dimensions.

Summarizing the results of the present section, it can be concluded that with the help of the flowmeters, the area-averaged flow velocities can be determined in the upper part of the cooling channels with an error of at most 6 %. v_F differs from the actual velocities in the channels due to the presence of radial and axial velocity profiles. In the next paragraph, these deviations will be examined.

3.3 Temperature Noise Measurements

Making use of standard data processing techniques, the signals of out-of-stream TCs were filtered, amplified, and sampled. The sampled noise signals were processed using the noise analysing code system available at the IRI [Hoo88] to obtain auto- and cross-power spectral density functions (APSD and CPSD) and cross correlation functions (CCF).

A transit time which characterises the propagation of temperature fluctuations between two axially displaced TCs can be determined from the measured noise, both in time- and frequency-domain. In the first case, the CCF of the temperature noise signals is used for velocity determination. In

this method, the position of the maximum of the CCF gives the transit time. In the second case, the slope of the phase of the CPSD of temperature noise signals is used. The phase is fitted to a linear curve, and the slope of this curve is proportional to the transit time, i.e., the time lag between the two signals for which the CPSD is calculated.

Results of experiment A (see Table I) will be analysed first. In Fig. 3.1, typical temperature noise spectra, phase, and coherence are shown, which belong to TC pair 1.2 - 2.3 at a distance of 9 cm. Similar behaviour is found for other TCs. The general properties of the measured temperature noise are as follows. There is a quick drop in the magnitude of the APSDs for every TC combination in the frequency region 0 Hz to 1 Hz, followed by a relatively slow change up to about 4 Hz. Most of the CPSDs and coherences have a dip at about 1 Hz. The phases of the CPSDs show a linear behaviour.

Velocities inferred from the phase plots are depicted in Fig. 3.2. The frequency region 0 Hz to 3.5 Hz has been used in the linear fitting after the elimination of the 2π phase jump. Above 3.5 Hz, the coherences diminish, and the phases are not linear any more. The velocity obtained by noise analysis is larger than the average flow velocity for each pair of detectors; for some TC pairs, the overestimation is close to 20 %. This discrepancy is very large and cannot be explained by the inaccuracy of the applied methods only.

Detailed analysis shows that the slopes of the phase curves are not exactly linear. The phase slope is higher below 1 Hz than in the 1 Hz to 3.5 Hz region. The deviation from the linear behaviour is larger for TC combinations at lower axial levels (e.g., pairs 1.2 - 2.3, 1.2 - 2.4, 2.3 - 2.4, 2.3 - 3.2) than at higher positions (e.g., 2.3 - 3.5 and 2.4 - 3.5). This conclusion is illustrated in Figs. 3.3a and 3.3b. The non-linear behaviour is clearly seen when the phase curve is compared to the fitted (linear) curve. The deviation from the linear phase behaviour is larger in Fig. 3.3a (TCs 1.2 and 2.3) than in Fig. 3.3b (TCs 2.4 and 3.5).

The above observations indicate that the temperature noise behaviour in the frequency region 0 to 1 Hz is different from the behaviour at higher frequencies (1 Hz to 3.5 Hz). In this sense, the temperature noise measured by TCs in the plates consists of at least two components. One of them is confined to frequencies below 1 Hz. This component indicates a relatively low propagation velocity. The other component is dominant between 1 Hz and 3.5 Hz and gives a higher propagation velocity.

The following velocities will be used in the forthcoming analysis:

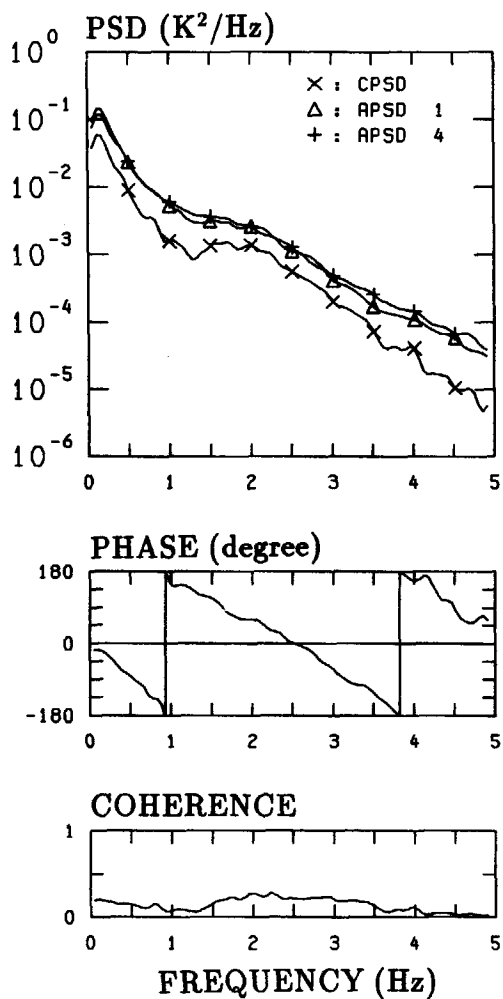


Figure 3.1: Magnitude, phase of CPSD, and coherence between the noise signals of thermocouples in experiment A; 1 - TC 1.2; 2 - TC 2.3.

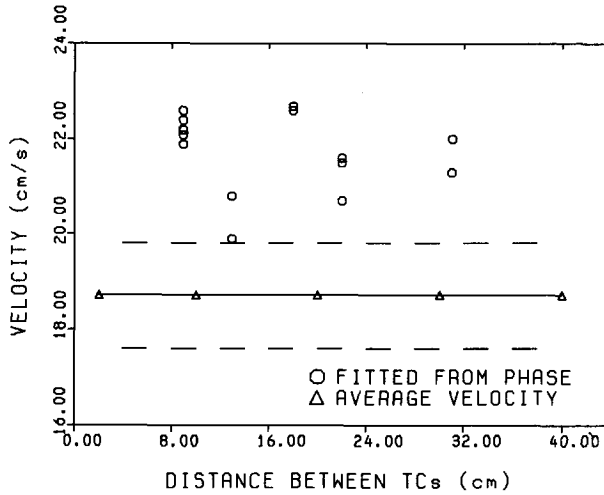


Figure 3.2: Velocities inferred from the slope of the CPSD phase in experiment A as a function of the distance between the TCs.

- v_F - velocity determined from the flow rate;
it is assumed to be the cross-section averaged
propagation velocity given in Table I;
- v_T - velocity inferred from the phase slope of the
temperature CPSDs at frequencies [0 Hz, 3.5 Hz];
- v_{TL} - the above definition with a modified (lower)
frequency region of [0 Hz, 1 Hz];
- v_{TH} - the above definition with frequency region [1 Hz, 3.5 Hz];
- v_{CCF} - velocity determined from the position of the main
peak of the CCF between temperature noise signals.

In the case of a two-parameter fit, a least-squares fit to a straight line $\varphi = ax + b$ is made over the specified frequency range. In this case, both a and b are fitted. For the one-parameter fit, $b = 0$ is assumed and only a is fitted. v_T and v_{TL} were determined by one-parameter fits; v_{TH} has been calculated on the basis of a two-parameter fit. The variance of the phase of CPSD (σ_φ^2) increases with decreasing coherence (γ^2): $\sigma_\varphi^2 \propto 1/\gamma^2 - 1$. Therefore, low coherence between the noise signals yields increasing error of the determined transit time. A TC pair was excluded from further evaluations if the average coherence over the investigated frequency region was less than 0.05 for that TC combination.

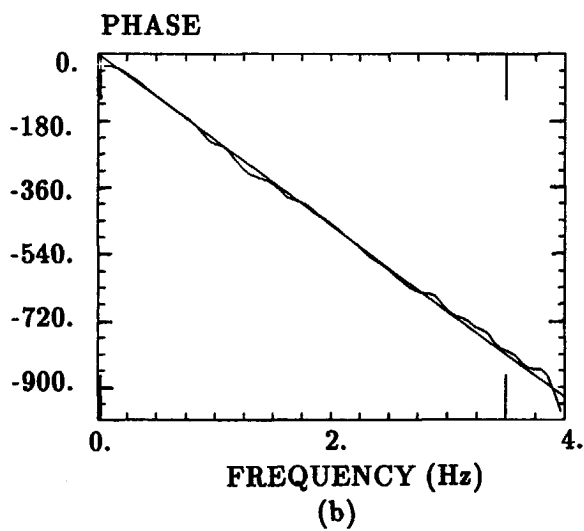
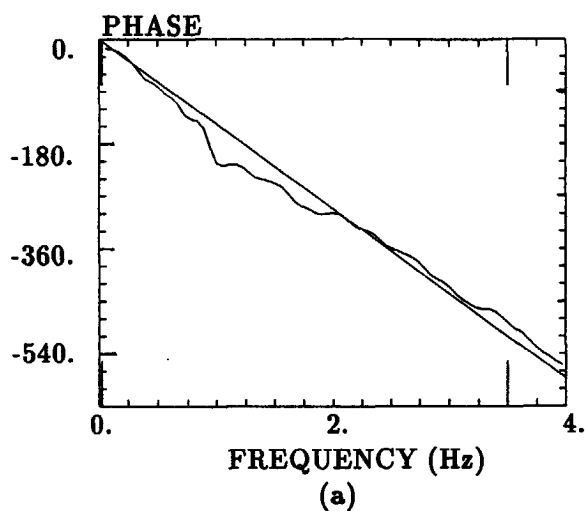


Figure 3.3: Phase curves fitted in the frequency interval 0 to 3.5 Hz for TC pairs: (a) TC 1.2 and TC 2.3; (b) TC 2.4 and 3.5.

The accuracy of v_{CCF} depends on the relation between the sampling time of the noise measurement, τ , and the transit time to be determined. In the present analysis, the value $\tau = 18$ ms has been used. In the worst case (i.e., when the velocity is high and the detector distance is minimal), this yields an inaccuracy of v_{CCF} of about 4%.

In Fig. 3.4, the inferred velocities are shown in relative units, compared to the average velocity v_F . On the horizontal axis, the average elevation of the TCs is given. The confidence interval of v_F is marked by dashed lines. It is clearly seen in Fig. 3.4 that v_T is found always outside this confidence interval. A much better agreement between v_F and v_{TL} : most of the v_{TL} points are located within the confidence region. The values of v_{TH} differ very much from each other and from v_F and vary from 21.3 cm/s to 32.6 cm/s. Combinations with TCs 1.2 and 3.2 give the highest v_{TH} values, and TC pairs at the top positions correspond to the lowest values of v_{TH} . It is a general tendency that v_{TH} decreases when taking higher axial positions.

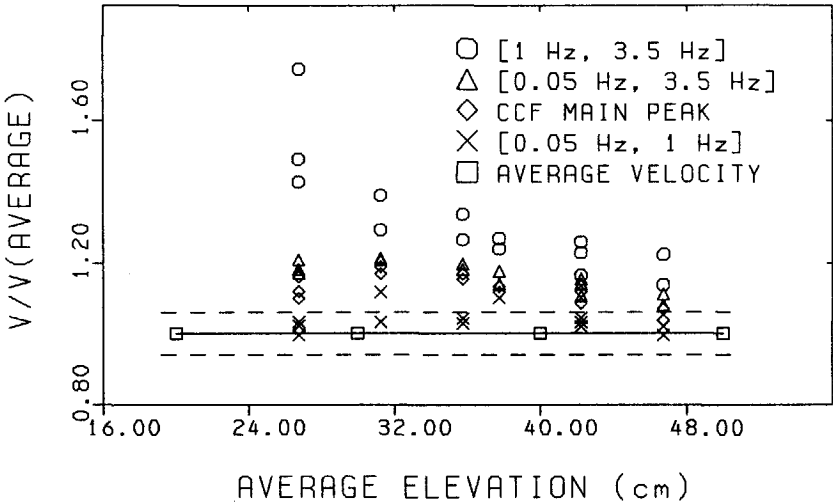


Figure 3.4: Inferred velocities in experiment A as a function of the average axial elevation of the TCs.

v_{CCF} always overestimates v_F , but it usually approximates v_F better than v_T does. At the highest positions, i.e., for combinations 1.5 - 2.4 and 2.4 - 3.5, v_{CCF} is found already within the confidence region of v_F . The

relationship between the different velocities finally appears as:

$$v_F \lesssim v_{TL} < v_{CCF} < v_T < v_{TH}. \quad (3.1)$$

Some additional information about the velocities can be gained by analysing the shape of the CCFs. The CCF of TC pairs 1.2 - 1.5, 1.5 - 2.3, 1.2 - 2.4, and 2.4 - 3.2 has a side peak. The side peaks are most pronounced for CCFs of distant TCs. The distance between the TCs must be at least 18 cm to obtain a clear side peak. An example of a CCF with a side peak is given in Fig. 3.5 for TCs 1.2 and 2.4. The velocities inferred from the side peaks of the CCFs are very large; they are larger than any of the velocities inferred from the phase slopes and vary from 30 cm/s to 50 cm/s.

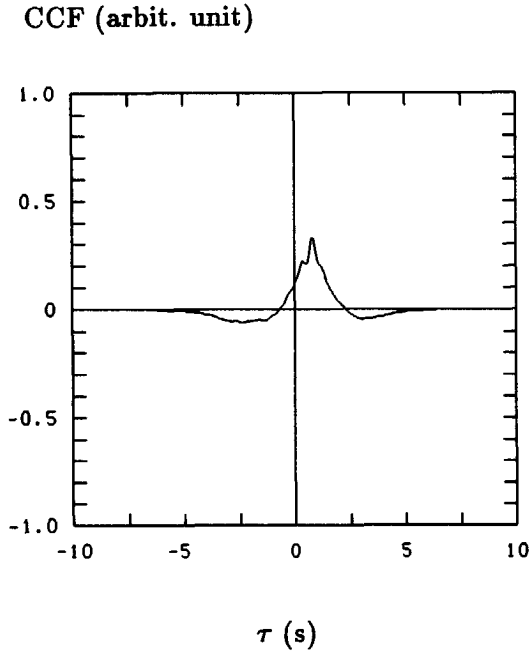


Figure 3.5: Cross correlation function with a side peak for TC 1.2 and TC 2.4

Further on, experiments B, C, and D with various flow rates and heating conditions are treated. In experiment C with volumetric flow rate 150 l/h, the coherences between the TC signals are smaller than in experiment A, in which the volumetric flow rate was 200 l/h. Every CPSD has a dip at low frequencies. For different TC combinations, the frequency of the CPSD dip

varies between 0.5 Hz and 1Hz. The phases have different slopes at lower and higher frequencies. The coherence has a well-defined minimum for certain pairs (e.g., 1.2 - 2.3, 2.3 - 2.4, 2.3 - 3.2). For other pairs (2.3 - 3.5, 2.4 - 3.5), the coherence diminishes below 1 Hz. In these latter cases, v_{TL} cannot be evaluated due to the low coherences.

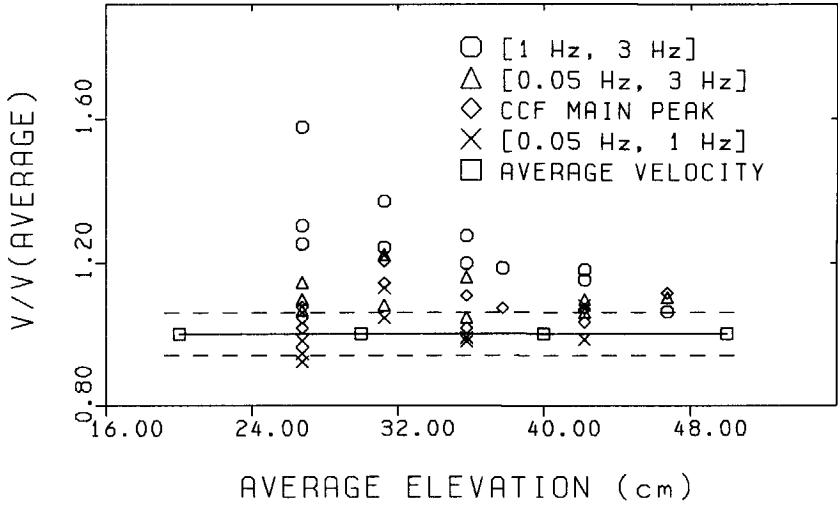


Figure 3.6: Inferred velocities in experiment C as a function of the average elevation of the TCs.

In Fig. 3.6, inferred velocities are shown as a function of the average axial elevation of the TCs in Experiment C. The applied frequency regions are $[0 \text{ Hz}, 3 \text{ Hz}]$ for v_T , $[0 \text{ Hz}, 1 \text{ Hz}]$ for v_{TL} , and $[1 \text{ Hz}, 3 \text{ Hz}]$ for v_{TH} . An upper fitting frequency of 3 Hz has been chosen, because the coherences diminish above 3 Hz in experiment C. v_{TL} agrees well with v_F ; all the v_T values are significantly larger than v_F ; v_{TH} is always the largest inferred velocity. v_{CCF} estimates v_F usually better than v_T does. In short, relationship (3.1) is fulfilled in experiment C as well.

The conclusion concerning the spatial behaviour of v_{TH} is the same as in experiment A: v_{TH} decreases with increasing axial TC positions. At the highest axial positions, v_{TH} is found within the confidence interval of v_F .

The following features of the noise spectra have been observed in experiments B and D. The coherences are lower than in the corresponding experiments A and C with higher heatings. Most of the CPSDs and coherences have clear dips. The exceptions are the combinations of TCs from opposite

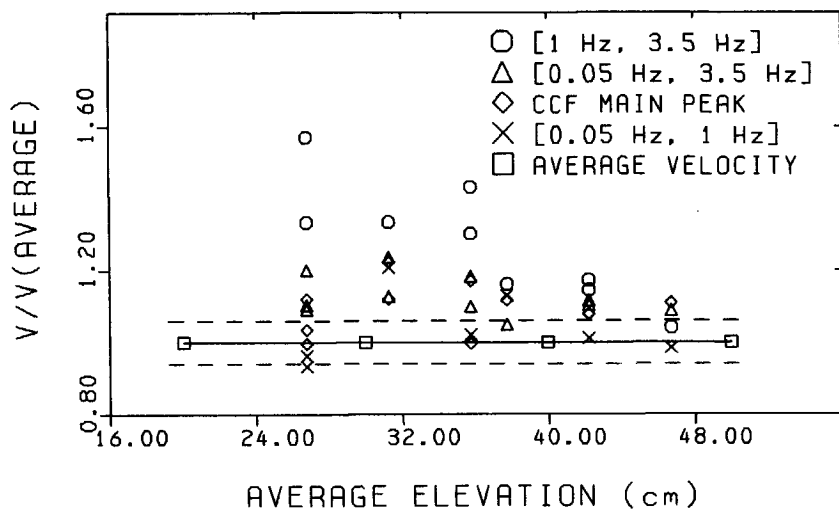


Figure 3.7: Inferred velocities in experiment B as a function of the average axial elevation of the TCs.

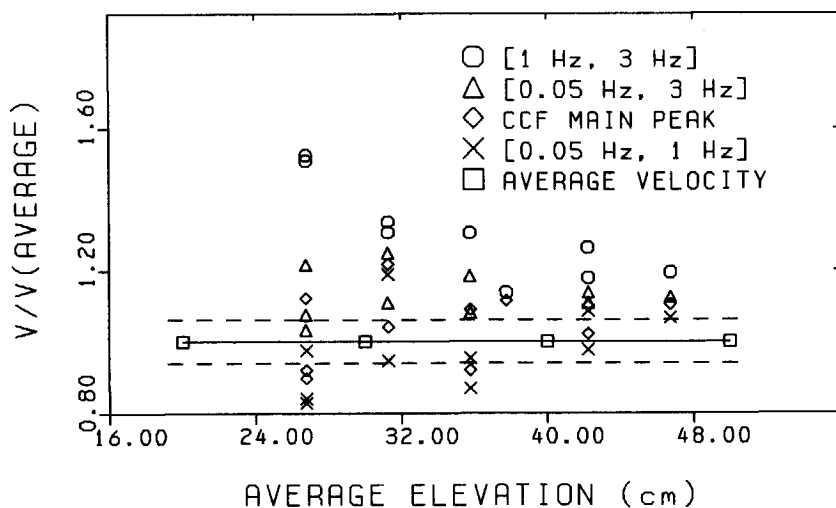


Figure 3.8: Inferred velocities in experiment D as a function of the average axial elevation of the TCs.

sides of the second channel, where the dips are weak due to the low coherence. The inaccuracy of the linear fitting of the phases of the CPSDs clearly increases in experiments B and D compared to experiments with higher powers. Velocities obtained in experiments B and D are introduced in Figs. 3.7 and 3.8, respectively. In experiment D, the differences between the velocities inferred at various frequency regions are much larger than in experiment C (compare Figs. 3.8 and 3.6). The deviation from linear behaviour becomes so pronounced in experiment B for certain TC combinations (2.3 - 3.2, 2.4 - 3.2, 2.4 - 3.3) that no velocities can be inferred. Figs. 3.7 and 3.8 show that the space-dependence of the inferred velocities described in the case of experiments A and C remain in force at lower powers, too. Also, condition (3.1) holds in these cases as well.

Experimental findings introduced in this section can be summarized as follows. The CPSDs and coherences between signals of TCs in the plates have a dip at about 1 Hz. The phases of the temperature CPSDs show a piecewise linear behaviour. Below the dip-frequency, the slope of the phase plot is larger than in the frequency region above the dip. For the various inferred velocities, relationship (3.1) holds. At higher axial positions, the difference between the inferred velocities decreases. Changing the flow rate, the above conclusions remain in force. The difference observed in the temperature noise behaviour at frequencies below and above the dip increased when the heating flux at the channel was reduced.

3.4 Some important aspects of the thermohydraulics of NIOBE

In this section, possible factors contributing to the measured temperature noise effects will be analysed. First, the effect of nuclear heating of the HOR is studied. Experiments were performed when the reactor was shut down in order to test the influence of the HOR heating on the observed phenomena. The volumetric flow rate was 200 l/h in both channels, and 2.8 kW heating was applied on each plate. The stationary temperatures in the fuel assembly in this experiment were lower by about 3°C than in experiment A with the same parameters but with HOR at power. The temperature noise field remained unchanged in general. All conclusions of the previous chapter concerning the CPSD, phase, coherence, and inferred velocities are valid in this case as well.

These results show that the low-frequency noise effects discussed in the

previous section are not generated by the heating contribution of the reactor.

Experiments performed at an earlier boiling setup [VMe84] did not show the two temperature noise components observed in experiments A, B, C, and D. Which factors contribute to the observed behaviour of the phase of the CPSDs in the present experiments? In order to answer this question, the construction of NIOBE and its earlier version has been investigated. Two major alterations in the channel geometries have been found: (1) the distance between the plates is 5 mm at NIOBE, and it was 3 mm in the previous assembly, (2) the channel cross-section suddenly increases at the inlet of the channels at NIOBE, but no such increase takes place in the earlier experiment.

At the inlet of NIOBE, the coolant passes through an orifice with a 61.5 mm \times 1.6 mm rectangular cross-section. This means that entering the channel, the flow suddenly expands; the expansion ratio is $A/A_0 = 3.125$, where A and A_0 are the channel and entrance cross-sections, respectively.

These modifications have an important effect on the velocity profile in the channels. Fully developed velocity and temperature profiles occur in a channel only after the coolant has travelled a sufficient length of that channel, measured from its entrance. This length is called the entrance length (l_e). It depends on the actual flow conditions and can be expressed in terms of the hydraulic diameter (D_e) of the channel. D_e is defined as $D_e = 4A/\Pi$, where A is the cross-section area, and Π is the perimeter of the channel. The entrance length is about 20 D_e in a tube; after a sudden expansion, it can be close to (30 - 40) D_e [ElW78].

In experiments introduced in [VMe85], a fully developed velocity profile is reached relatively quickly at a distance of ca. 12 cm measured from the entrance of the channels, taking into account $D_e = 0.57$ cm in that case. In the upper part of the channels, the velocity variations are determined by the convective heat exchange between the coolant and the channel wall. The situation is different at NIOBE, where $D_e = 0.92$ cm and $l_e = 28-37$ cm, i.e., entrance effects are important up to medium axial elevations. Due to the sudden expansion of the flow at the entrance, the main stream of the flow is concentrated in the central third of the cross-section directly after the channel entrance. The maximum (central) velocities decrease during the flow expansion. In the upper half of the channels, the velocity distribution is close to the developed velocity profile.

The value of the Reynolds number was between 2900 and 5500 in the experiments. Therefore, there is usually turbulent flow in the upper regions of the channels. The flow may have a transition character between the laminar

and turbulent flows in experiments with the lowest Re number (experiment D).

3.5 Discussion

Temperature noise measurements illustrate good agreement between the area-averaged flow velocity and the velocity inferred from the slope of the phase curve of temperature CPSDs at frequencies up to 1 Hz. v_{TL} can be regarded as a good approximation of the average flow velocity in the simulated assembly.

Let us now consider v_{TH} , which is always larger than v_F . Several physical phenomena may contribute to the presence of velocities larger than the area-averaged value. The first is the entrance effect, which extends up to medium axial elevations at NIOBE. The flow velocity exceeds v_F by about 3 times at the channel entrance. Moving upwards in the channel, the coolant flow expands, and the maximum (central) velocities decrease. In the upper regions, the radial velocity distribution in the developed flow determines the velocities. The magnitude of this effect depends on the flow type and can be characterised by a peaking factor $PF = v_{max}/\bar{v}$, where v_{max} is the maximum of the velocity in the cross-section of the channel, and \bar{v} is the area-averaged velocity.

The coolant temperature is highest at positions close to the wall due to heating through the plates. This temperature distribution yields an additional free convection and leads to increased upward velocities in the direct neighbourhood of the wall. This phenomenon, as well as the effects caused by the axially non-uniform heating power distribution, modify the velocity profile. Therefore, no fully developed turbulent profile can be expected at NIOBE.

In the next considerations, we check the consistency of the assumption that v_{TH} is connected with the maximum of the radial velocity profile. If this assumption is true, the peaking factor can be estimated by the quantity v_{TH}/v_F . Further on, this ratio will be called the experimental peaking factor.

Let us consider first the lower channel regions, up to axial elevation of 37 cm. If v_{TH} is related to the maximum velocities, then it must decrease at higher TC positions, for when taking higher axial positions, the velocity profile is more and more equally distributed. This is exactly what is seen in Figs .3.4 and 3.6 to 3.8. Also, the magnitude of the experimental peaking factor seems to be reasonable. Its maximum value is about 1.6 -1.7 (at axial

elevation 26 cm), which may reflect an intermediate stage of the actual flow expansion. v_{TH} decreases further in the upper regions of the channel. The peaking factor varies between 1.5 to 1.1 in the upper half of the channel. At the highest positions, v_{TH} approaches v_F , and the experimental peaking factor drops to 1.15 - 1.1, which is the property of a flat velocity profile.

Consequently, the large velocities at higher frequencies (above the dip-frequency) may have a connection with the radial velocity profile. In the experiments, however, it is impossible to measure the actual velocity distribution. Therefore, the validity of this interpretation cannot be tested experimentally. However, model calculations introduced in the next section contribute to a better understanding of the observed phenomena.

3.6 Model calculations

In these calculations, we use a method in which fluctuations in the two-phase flow are simulated numerically. A simulation method has been used earlier [Lub83a] for the interpretation of velocities obtained from noise signals of axially displaced detectors (light-beam detectors, neutron detectors, etc.). The main assumptions of our model are as follows. The fuel plates are assumed to be infinite plane slabs in the y- and z-directions, with a coolant streaming between them in the z-direction. The coolant flow has constant parameters in the z-direction and has a certain velocity profile along the x-axis.

Fluctuations, which move with a velocity $v(x)$ in the subchannel of width dx at a distance of x from the first plate, have a certain contribution to the signal of the detector positioned in the first plate. It is assumed that the weight of this contribution depends only on the distance x . The noise of the total detector signal in the wall can be written as a superposition of the contributions of the noise sources in the individual subchannels and the background noise:

$$T_1(t) = \int_0^d f(x) \Theta(x, t - \frac{x}{v_r} - \tau_F) dx + w_1(t), \quad (3.2)$$

where

$\Theta(x, t)$ - temperature noise sources in a subchannel of unit width
at a distance x from the wall

$T_1(t)$ - total noise signal of the first detector at the channel wall

$f(x)$ - weighing function

- $w_1(t)$ - background noise component of the first detector signal
- d - width of the channel
- τ_F - time constant of the fuel plate
- v_r - characteristic velocity of radial turbulent mixing.

The signal of a second detector located at a distance of z above the first detector appears as:

$$T_2(t) = \int_0^d f(x) \Theta(x, t - \frac{z}{v(x)} - \frac{x}{v_r} - \tau_F) dx + w_2(t). \quad (3.3)$$

Here $T_2(t)$ and $w_2(t)$ are the total noise signal and the background noise component of the second detector signal, respectively. According to Eq. (3.2), signals at radial position r arrive at the detector in the wall with a delay time of $\tau_D = \frac{x}{v_r} + \tau_F$. The first term describes the propagation of temperature fluctuations in the turbulent flow in radial direction, while the second term is responsible for the delay time of the convective heat transfer process at the wall and the propagation of temperature fluctuations inside the plate. Eq. (3.3) expresses the fact that fluctuations at a distance x from the first wall appear with a time-delay $z/v(x)$ at higher positions, where z is the distance between the two axial positions.

In the numerical calculations, the channel has been divided into n subchannels. The integral over the channel width in Eqs. (3.2)-(3.3) is approximated by a finite sum, and the noise sources in the i^{th} subchannel are represented by a single fluctuation $\Theta_i(t) = \Theta(x_i, t)$, where $x_i = id/n$. It is assumed that the correlation between fluctuations $\Theta_i(t)$, $i = 1, \dots, n$ exponentially decreases with increasing distance between the subchannels. Moreover, $w_j(t)$, $j = 1, 2$ are white noise sources which are independent of $\Theta_i(t)$. The effect of the fluctuations in a given subchannel on the signal detected at the channel wall is decreasing with increasing distance between the detector and the subchannel. This effect will be approximated by an exponential weighing function: $f(x) = \exp(-x/D)$, where D is a constant that describes how deep the detectors "look" into the channel. Using an earlier terminology [Lub83a], d/D is called the field-of-view parameter.

The actual fluctuations, temperature fluctuations in our case, are certainly not white. Also, the weighing function is more complicated in reality than in our assumptions, for it depends not only on the distance of the subchannel to the wall but also on the local velocity $v(x)$. Nevertheless, even this very simple model is able to reflect some of the main features of the measured signals.

Let us estimate the order of different delay times. The fuel time constant can be calculated according to equation $\tau_F = \rho_F c_{p,F} R_F / (2h)$, where ρ_F and $c_{p,F}$ are the density and specific heat of the fuel, respectively; R_F is the width of the fuel plate, and h is the effective fuel-to-coolant heat transfer coefficient. A numerical value of $\tau_F = 2.76$ s is obtained with parameters $\rho_F = 2.7 \times 10^3$ kg/m³, $c_{p,F} = 0.89 \times$ kJ/kgK, and $h = 1.745$ kW/m²K. The plate width is 4 mm. The large time constant is the result of the large R_F , low velocities, and low thermohydraulic parameters at NIOBE in the case of single phase coolant. NB: τ_F of an MTR-assembly at nominal HOR parameters is about 0.25 s or even less. The response time of temperature diffusion inside the fuel of NIOBE is much less than τ_F and, based on the model given in Appendix B, its value is a few milliseconds. The propagation time of turbulent temperature transfer in radial direction in the coolant channel is also much smaller than τ_F , taking into account that the width of the channel is just 5 mm. Finally, the transit time of temperature fluctuations between two TCs at a distance of 9 cm varies between 0.45 s and 0.7 s for velocities between 14 cm/s and 20 cm/s, which are the nominal velocities in the present experiments. Based on these considerations, the effects of radial time delay in the coolant and temperature diffusion in the plate is neglected with respect to the fuel response time.

Synthetic noise signals were produced by making use of Eqs. (3.2) and (3.3) and by applying a random number generator to simulate the subchannel fluctuations and the background noise. These synthetic signals were processed and their spectra were evaluated as if they were actual noise signals.

An example of the calculated spectra is shown in Fig. 3.9. The applied velocity distribution was a profile with peaking factor of 1.32, which is more pronounced than a fully developed turbulent profile. The field-of-view parameter is equal to 1 in this case. The linear fit of the phase gives a velocity 21.7 cm/s at frequencies [0 Hz, 1 Hz] and velocity 32.5 cm/s at frequencies [1 Hz, 5 Hz]. The first velocity, v_{TL} , is close to the area-averaged velocity (22.7 cm/s), while the second one is closer to the maximum of the input velocity profile (30 cm/s). Numerical experiments with a great variety of velocity profiles show that v_{TL} agrees well with the area-averaged velocity, and it is always much smaller than v_{TH} . v_{TH} is always close to the value of v_{max} .

Calculations have been performed with different field-of-view parameters. Increasing its value, which means decreasing D , the velocities inferred from the phase slope are more and more close to the minimum velocity. In the

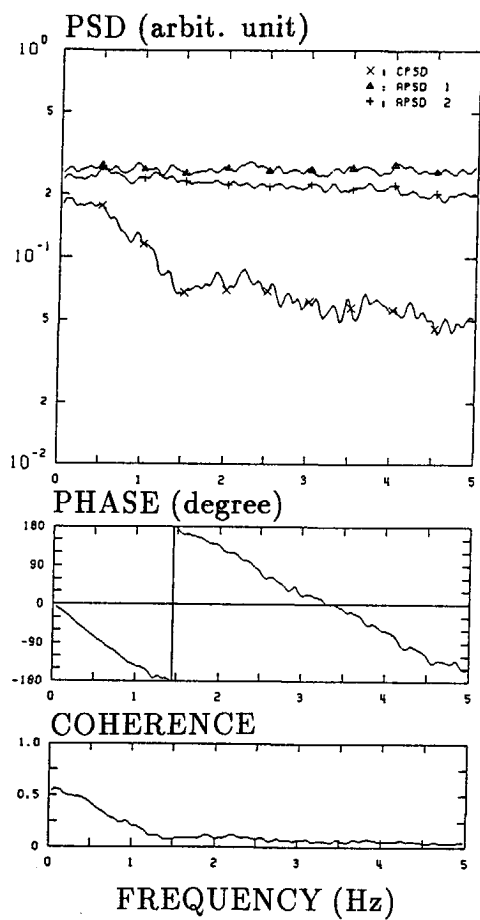


Figure 3.9: Spectra, phase of CP5D and coherence calculated using synthetic noise signals; the peaking factor of the applied velocity profile was 1.32.

applied profiles, the minimum of the velocity profile was at the wall. The above result means that, for $d \gg D$, only perturbations from the direct neighbourhood of the wall affect the detector signal. For a field-of-view parameter around or below 1, the phase behaviour becomes significantly non-linear, and v_{TL} and v_{TH} are close to the average and maximum velocities, respectively.

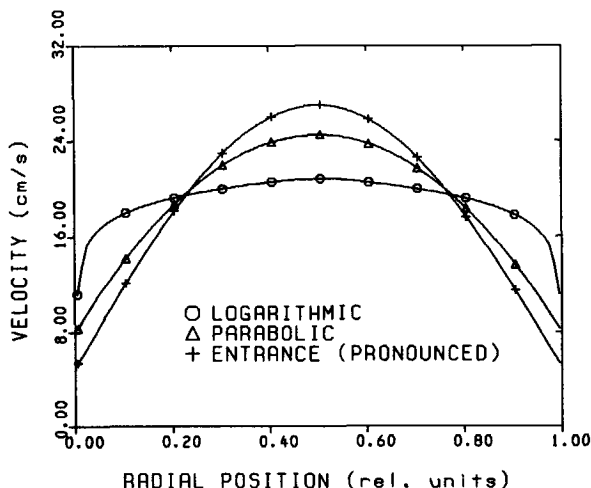


Figure 3.10: Velocity profiles used for the generation of the synthetic noise signals.

In the following, some further simplifications will be introduced. The influence of the background noise will be neglected. In this case, the field-of-view parameter and the velocity distribution determine the calculated spectra. Calculations with three velocity profiles (see Fig. 3.10) will be introduced. The logarithmic profile is flat. The parabolic profile has a higher peaking factor, while the third case represents the most pronounced profile. These profiles approximate in certain respects the turbulent, laminar, and entrance velocity profiles, respectively. The area-averaged velocity is 19 cm/s in every case; the field-of-view parameter is 1.

Calculated phase curves are depicted in Fig. 3.11. The phase slope is almost constant for the logarithmic profile. Taking other velocity profiles with higher peaking factors, the non-linear character of the curves increases. In Fig. 3.12, velocities inferred from the phase curves via one-parameter linear fitting over a variable interval $[0.05 \text{ Hz}, f]$ are shown, where f is the

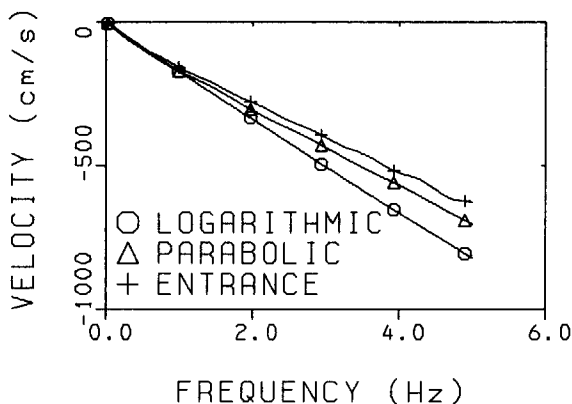


Figure 3.11: Curves of the phase of CPSD of the synthetic noise signals for different velocity profiles.

frequency indicated along the x-axis. The inferred velocities increase with increasing upper frequency to the fitting interval. The most remarkable variation of the velocity as a function of the fitting interval is found in the case of the entrance profile. This curve starts well below the average velocity, then quickly increases. The inferred velocity differs from the maximum by less than 10 % for upper fitting frequencies close to 5 Hz. Less remarkable variation is found in the parabolic profile. The velocities change only slightly when the fitting interval varies in the case of logarithmic profile.

The average velocity (19 cm/s) is reached below 1 Hz for the entrance profile, while the value of this frequency is somewhat higher than 1 Hz for the other profiles. Calculations with a two-parameter fit in the interval [1 Hz, 5 Hz] show that the inferred velocity, v_{TH} , differs from the maximum velocity by less than 5 %.

Calculations show that the slope of the phase of the CPSD between signals of axially displaced detectors at low frequencies is larger than at higher frequencies. By fitting the curve in the frequency region below 1 Hz with a linear curve, velocities close to the area-averaged velocity are obtained. The inferred velocities are closer to the maximum when choosing a higher frequency region for the fitting. This means that some of the main features of the measured spectra can be reproduced by simulations with synthetic noise signals.

Also, the observed minima of CPSD and coherence between temperature

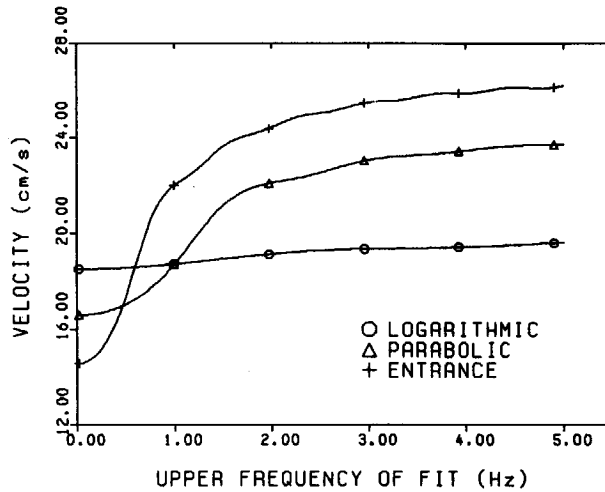


Figure 3.12: Velocities inferred in the case of synthetic noise signals.

noise signals can be related to the presence of a velocity profile in the channel. It can be shown that the coherence has periodic minima if two propagation phenomena with different velocities influence the detector signals. The frequency of the minima f_m is given by $f_m = (2k - 1)/[2(\tau_1 - \tau_2)]$, $k = 1, \dots, n, \dots$ where τ_1 and τ_2 are the transit times belonging to the first and second transport effect, respectively. The situation is much more complicated in the case of a velocity distribution. Nevertheless, it has been shown in [Koz91] that, in many practically important cases, two dominant velocities emerge from the total spectrum of velocities. These dominant velocities determine a resonance structure with periodic minima in the corresponding CPSDs. For these two effective transit times, the above expression of f_m can be used.

3.7 Conclusions

1. The noise of TCs in the fuel plates of the simulated fuel assembly can be divided into a lower and a higher frequency part. In both regions the phase of the CPSDs between TC signals can be approximated by a first order (linear) curve. The slope of the phase curve is larger in the low-frequency part than at higher frequencies.
2. The velocity obtained from the phase slope at lower frequencies agrees

well with the average velocity determined from the indication of the flowmeters. Model calculations support this experimental result.

3. Velocities which have been inferred in the region above the dip-frequency are closer to the maximum of the radial velocity profile. The actual radial velocity distributions were unknown in the experiments. Analysing the given experimental circumstances and the results of model calculation, it seems possible that the velocities at high frequencies are connected with the maximum velocities in the channels. Consequently, the observed temperature noise effects may be caused by the radial velocity profile in the coolant.

Chapter 4

Identification of Flow Patterns During Actual Coolant Boiling in Thin Rectangular Channels†

Flow patterns in the boiling coolant are identified by means of analysis of probability density functions and power spectral densities of neutron noise measured by self-powered neutron detectors. It is shown that boiling has an oscillating character due to partial channel blockage caused by steam slugs generated periodically between the plates. The observed phenomenon can serve as a basis for a boiling detection method in reactors with plate-type fuels.

4.1 Introduction

Flow pattern identification is a thoroughly studied topic of two-phase flow investigations. In nuclear reactor applications, interest is directed first of all towards vertical flows. It is common to distinguish two-phase flow patterns on the basis of spatial arrangement of the phases. Further on, we will use the following classification of flow patterns in vertical channels: bubbly flow, slug flow, churn flow, and annular flow.

†This Chapter is an adapted version of the paper "Identification of Flow Patterns by Neutron Noise Analysis During Actual Coolant Boiling in Thin Rectangular Channels", by R. Kozma, H. van Dam, J.E. Hoogenboom, to appear in Nuclear Technology (1992).

Bubbly flow is characterized by a suspension of discrete bubbles surrounded by liquid and occurring at low void fractions. In slug flow, large bubbles appear which fill in almost the entire cross-section of the channel; the space between two large bubbles is occupied by a mixture of water and small bubbles. In annular flow, a continuous liquid annulus flows along the wall while gas flows in the central regions. This flow pattern occurs at high void fractions. Of course, hybrid flow patterns can be introduced as well, which represent a transition from one flow-type to another. In fact, slug flow can be treated as a transition between bubbly and annular flow at not very high flow rates. At certain flow conditions, mostly at higher flow rates, churn flow can occur which is more chaotic and disordered than slug flow. A systematic overview of the existing theoretical models and measurement methods aimed at flow regime identification is given by [Duk86].

The first flow-regime investigations were based entirely on visual observations. Later on, various measurement techniques were applied for the characterization of two-phase flow patterns. These methods can be either direct observations, which include light/laser beam transmission and X-ray densitometry, or indirect studies based on the analysis of the fluctuations of certain process variables, e.g., pressure and neutron flux, which are modulated by the two-phase flow. The so-called direct methods, by the nature of the utilized signals, mean out-of-core experiments. Light/laser beam experiments at air-water loops proved to be useful in the interpretation of propagating velocities measured by noise techniques [Mit79], [Lub83b], [VDH88], and in some cases they could be utilized to obtain information about the flow regime [Wan88].

Results obtained with the help of X-ray void measurement systems can be summarized as follows [Jon75], [Lah78], [Vin82]. The moments of the probability density function (PDF) and the power spectral density (PSD) of the detector signals are useful for the identification of flow regimes. In the analysis, usually four moments of PDF were utilized: (1) the first moment, i.e., the mean value of the signal; (2) variance, or the second central moment, a measure of the distribution about the mean; (3) skewness, or the third central moment normalized by the 3rd power of standard deviation, a measure of the asymmetry of the PDF; (4) kurtosis, the fourth central moment normalized by the 4th power of standard deviation, a measure of the peakedness of the distribution.

Different flow patterns are characterised by the following properties [Vin82]. Slug flow has two PDF peaks (bimodal flow), the variance of the PDF is large, the skewness is close to zero (good symmetry), and the kurtosis is

smaller than 3 (flattened PDF). On the other hand, PDFs of bubbly and annular flows are single-peaked (unimodal flow), their variance is small, and skewness is large compared to the values of slug flows. Finally, their kurtoses are greater than 3 which is a property of peaked PDFs compared to a Gaussian one. These two flow patterns can be distinguished on the basis of the position of their single PDF peak; the PDF peak of the bubbly flow belongs to low void fractions, while this peak is in the region of high void contents in the case of annular flow. The actual distinction between bubble and annular flows must include some preliminary information about the system, e.g., history, and expected value of the void fraction.

If the two peaks of the PDF of a bimodal flow are distinct, the kurtosis is much smaller than 3, and the bimodal character of the flow can be recognised easily (e.g., by eye inspection) without calculating the actual kurtosis value. Nevertheless, it is still meaningful to calculate this parameter, because its actual value can be used as a criterion in automated system which monitor bimodal flows.

In the case of air-water flow in a test tube, the threshold normalized variance value of 4 % has been established for the bubbly to slug and slug to annular transitions. The direction of changes is different in the above two cases: bubbly to slug transition is characterized by increasing variance, while the variance decreases during slug to annular transition. Concerning the PSD functions, it has been revealed that bubbly flow has a broad-band and low-magnitude spectrum in comparison with other flow types; in annular flow the spectrum is of medium band and medium magnitude; finally, a slug flow is characterized by PSD peaks at low frequencies.

A succesful flow pattern identification in an actual nuclear reactor has been reported in [Alb82] on the basis of results obtained at a test loop located in a research reactor. Making use of the measured neutron noise signals, different flow types (bubbly, churn, and slug flows) have been identified. Introducing a parametrisation of the two-phase flow, several main properties of the two-phase mixture have been estimated, e.g., void contents, average residence time, and variance of both modes. These results are based mostly on the evaluation of PDFs of neutron signals.

A different method is based on evaluation of the high frequency contribution fraction (HFCF) of neutron noise in an air-water test loop in the Zero-Power Reactor at INER, Taiwan [Wan89]. This method was originally used for the interpretation of light emission measurements [Wan88], and it is based on the experimentally observed variation of the bandwidth of the PSD among different flow conditions. These experiments have been analysed via

autoregressive moving average (ARMA) modelling as well. Based on this model, two-phase flow patterns were identified by the so-called "dynamic signature" index [Kin89].

All the experiments introduced so far were performed at air- water loops, i.e., without actual coolant boiling. The identification of flow patterns in the boiling coolant via neutron noise measurements is an important and till now an unsolved issue of nuclear reactor monitoring.

In the present work, boiling in narrow channels between fuel plates of a simulated MTR-type fuel assembly was studied. Plate-type fuels are often used in research reactors, where boiling is not allowed during normal reactor operation. Therefore, the detection of boiling is of great importance from the safety point of view.

It has been outlined in [Sud86] and in [Bel88] that coolant boiling in thin rectangular channels has its own peculiarities, and correlations obtained for tubes and rod bundles have to be applied in this case with caution. The main task of these works was the investigation of the onset of nucleate boiling in the channels. It has been demonstrated in the case of low velocities, in particular, that the onset of nucleate boiling is determined not only by local pressure and wall superheat but by the channel gap size and flow velocity as well. In the case of upward flow in narrow coolant channels, the bubbles which grow on opposite channel walls sometimes join and move upwards without detachment by the flow and buoyancy and leave the channel in the form of a vapour slug [Bel88]. On the other hand, low-frequency flow and temperature oscillations have been observed in the boiling coolant with downward flow direction [Sud86].

In the present chapter, an example of flow pattern identification at NIOBE via neutron noise analysis will be introduced. We do not intend to give a general identification procedure, as the results depend very much on the actual experimental circumstances. Particularly, the character of the observed phenomena is determined to a great extent by the fact that boiling occurs in narrow ducts during the experiments. The obtained results demonstrate the usefulness of neutron-noise-based boiling identification and, perhaps, they can stimulate further studies in this topic.

4.2 Description of the experiments

4.2.1 Parameters of experiments

The volumetric flow was 100 l/h in both channels of NIOBE during the experiments, according to the indication of the turbine flowmeters. This value corresponds to an equivalent area-averaged velocity value of 9.4 cm/s between the plates. This means a significant degradation of the cooling conditions as compared to the nominal HOR operation, when the velocity of the coolant flow downwards between the fuel plates is about 50 cm/s. A significant decrease of the coolant flow at HOR can be caused by (partial) blockage of one or several channels. The flow has upward direction in the experiments. Low coolant flow rates in an upward direction can occur at HOR in a natural circulation regime following an emergency stop.

The actual velocities differ from the value of 9.4 cm/s due to the presence of radial and axial velocity profiles in the coolant as well as to the possible occurrence of boiling in the channels. Indeed, coolant boiling took place in the experiments, as will be shown in the following.

Two heating levels have been applied in the experiments. First, we used 3 kW heating power on each plate, which represents heating conditions in an average HOR assembly. Due to the reduced flow rate compared to the nominal value at HOR, some of the TCs in the walls detected a wall-superheat of 5°C. The experiments have been analysed using the 1-dimensional thermo-hydraulic code HEATHYD [Nab89]. The results show that the coolant bulk-temperature remains under saturation in the experiments, but the Bergles-Rohsenow criterion [Roh85] for the onset of nucleate boiling is satisfied between axial positions of 18 cm and 40 cm, i.e., surface boiling occurs at the hottest positions.

In the second case, 6 kW heating power was used at each plate. This value is close to the 7.2 kW per plate maximum value with the HOR operating at a nominal power of 2 MW. Taking into account the sizes of the plates and the power distribution in the plates, we obtain a maximum heat flux density of 122.5 kW/m² at NIOBE. In experiments with 6 kW per plate, the onset of the nucleate boiling criterion is satisfied along almost the total length of the channels. At this higher heating power, the TCs indicate large temperature fluctuations. The magnitude of these fluctuations is 3-5°C in the wall and 8-10°C in the coolant at the outlet of the channels. The maximum temperature measured by outlet TCs is close to the saturation temperature.

In the present experimental circumstances, important factors contribut-

ing to the coolant heat-balance equation (inlet enthalpy, heat losses) cannot be determined with proper accuracy. Therefore, the coolant boiling state cannot be evaluated on the basis of thermohydraulic calculations. Neutron detector signals, however, are useful for boiling monitoring, as will be shown in the following.

4.2.2 DC component of neutron detector signals

The variation of the thermohydraulic state of the coolant has an influence on both the DC and AC components of the neutron detector signals. First, let us see what kind of changes are expected in the DC level according to numerical calculations. Calculations have been performed with the code CITATION [Fow71] for a 2-dimensional HOR model in X-Y geometry using ENDF/B-IV data with different amounts of homogeneously distributed void fraction in both coolant channels.

The results are depicted in Fig. 4.1, where the relative variation of the thermal neutron flux is shown at the positions of the 3rd and 4th SPND strings as a function of the void fraction (α) in the channels. The calculated effect is localized at the position of the assembly, and the relative neutron flux variation in the core amounts to less than 0.1 % at a distance of 8 cm from the set-up, even in the case of high (75 %) void fraction. Further on, the analysis of the thermohydraulic processes at NIOBE will be introduced on the basis of the evaluation of the available SPND signals.

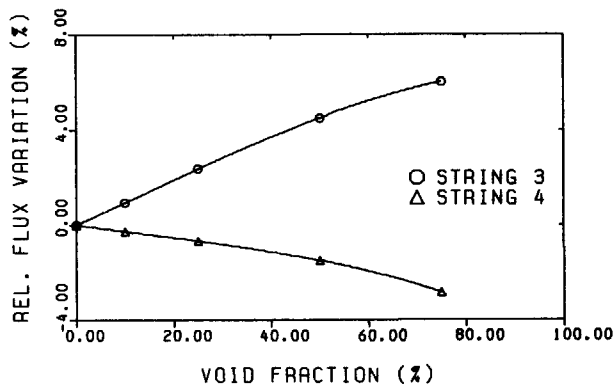


Figure 4.1: Calculated thermal neutron flux changes caused by varying void content in the cooling channels; evaluations by code CITATION.

Comparison of DC signals of the SPNDs in the two measurements, i.e., 3 kW per plate and 6 kW per plate, respectively, indicate positive void

effect at string 3, but there is a negative effect at string 4. The relative variation, R , of the DC level of SPNDs in strings 3 and 4 is depicted in Fig. 4.2 as a function of the axial elevation. Quantity R is defined as $R = \Delta U / U_0$, where $\Delta U = \max[U_1(t) - U_0]$ and U_1 and U_0 are the measured SPND signals during experiments with 6 kW per plate and 3 kW per plate, respectively. In experiments with the 6 kW per plate, the SPND signal level fluctuates significantly; for the sake of definitiveness, we use the maximum of the deviation in the definition of R . Also, the error of quantity R is indicated in Fig. 4.2. The high errors are due to the fact that the observed void effect causes DC-level variation up to ~ 100 mV, while the background noise of the signals amounts to, at least, 10-20 mV. The curves have an extremum (maximum and minimum for strings 3 and 4, respectively) at axial positions 40-50 cm. Comparing Figs. 4.1 and 4.2, it is concluded that the maximum void fraction is 40-50 % in the channels.

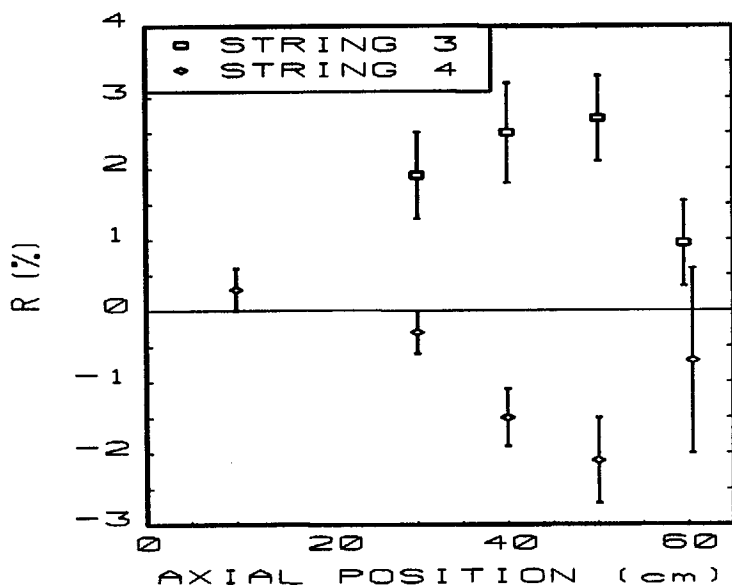


Figure 4.2: Measured relative variation of the neutron flux along NIOBE.

4.3 Neutron noise effects

The signals of the SPNDs were band-passed, filtered, and sampled. The sampled noise signals have been processed both in time domain and, following the standard fast Fourier-transformation procedure, in frequency domain. Results of the evaluations are introduced in this section.

4.3.1 Time domain analysis

The time signals of the SPNDs at different axial locations of string 4 are depicted in Fig. 4.3. On the vertical axis of Figs. 4.3a-e, the normalized magnitude of the fluctuations is shown; along the horizontal axis, the time is in seconds. At lower positions (10 cm and 30 cm) as well as at the highest elevation (60 cm), fluctuations occur with relatively low magnitude. Periodic fluctuations take place at detector positions 40 cm and 50 cm. The period of this fluctuation is ~ 4 s. The exact value of this period (4.45 s) is determined on the basis of spectral analysis of the signals to be introduced in the following section. Note that there are only two SPNDs in one string; therefore, the time-plots in Fig. 4.3 belong to different experiments with the same thermohydraulic parameters but with different detector positions.

It is quite obvious that a periodically occurring perturbation affects the neutron field and causes regular breakdowns in the neutron flux. The fluctuations of the SPNDs are largest at those axial elevations where the heat flux density at the wall is the highest. The TCs in the coolant and in the wall material indicate fluctuations with the same period. These arguments show that the perturbation causing large neutron fluctuations is of thermohydraulic character. More specifically, these perturbations are coolant density fluctuations due to boiling at the hottest positions of the channels. The periodic minima in Figs. 4.3b-c can be interpreted as the result of large void fractions appearing in the neighbourhood of the SPNDs, thus causing local thermal neutron flux drop due to the negative void effect at string 4.

In order to develop a possible objective characterisation of the boiling process, we introduce various statistical descriptors of the neutron noise.

The PDFs of the different noise signals are displayed in Figs. 4.4a-e. Along the x- and y-axes, the magnitude of the fluctuations in volts and the counting rates with arbitrary scale are shown, respectively. The presence of two peaks in the PDF in Figs. 4.4b and 4.4c is an indication of the bimodality of the coolant flow. A peak with large magnitude and relatively small width is found on the right-hand side of Figs. 4.4b-c, i.e., at higher

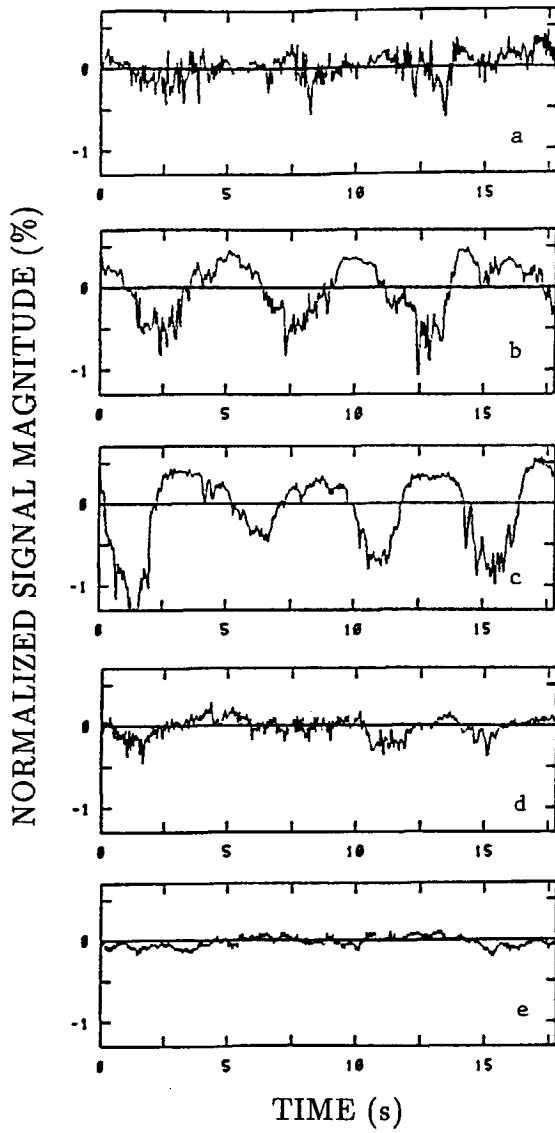


Figure 4.3: Normalized time signals of SPNDs located at different axial elevations in string 4;
(a) - 60 cm, (b) - 50 cm, (c) - 40 cm, (d) - 30 cm, (e) - 10 cm

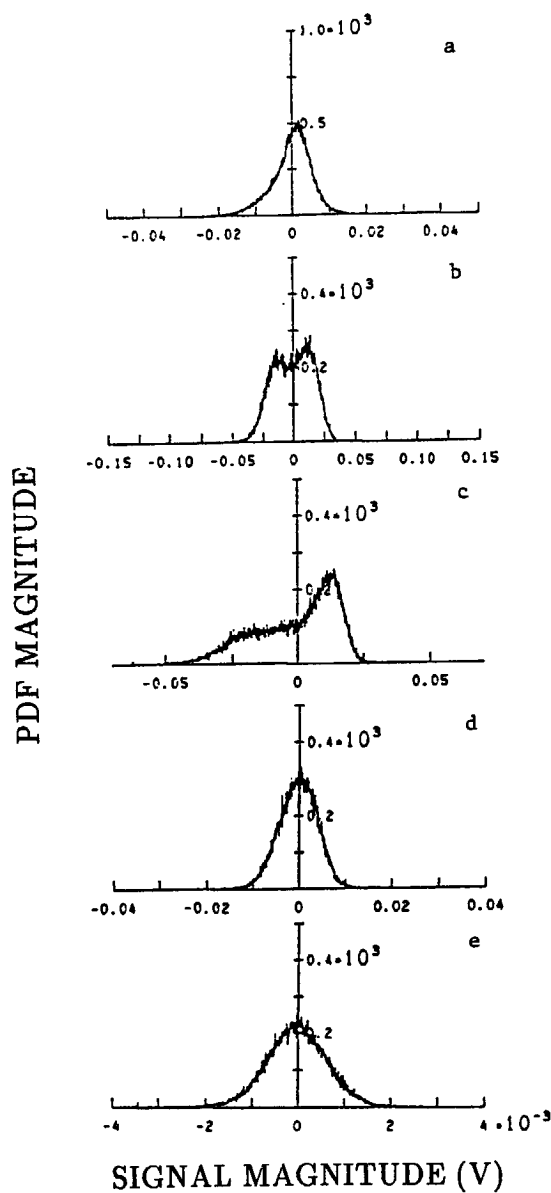


Figure 4.4: Probability density functions of signal amplitudes of SPNDs located at different axial elevations in string 4;
(a) - 60 cm, (b) - 50 cm, (c) - 40 cm, (d) - 30 cm, (e) - 10 cm.

signal amplitudes. Taking into account that the void effect is negative in string 4, we find that this peak is in the region of small void fractions (or even without void at all). The other maximum is less pronounced and appears at lower signal levels, i.e., at higher void fractions.

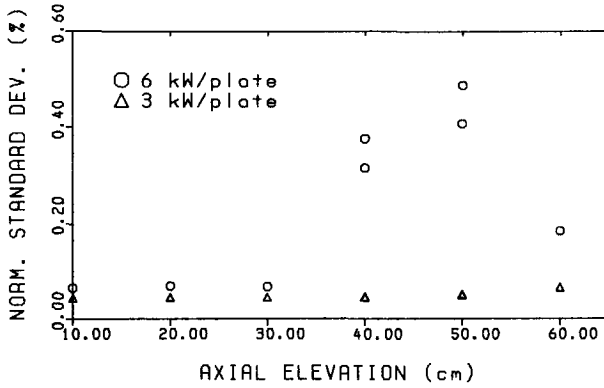


Figure 4.5: Standard deviation of the PDFs of SPND noise signals as a function of axial elevation in string 4.

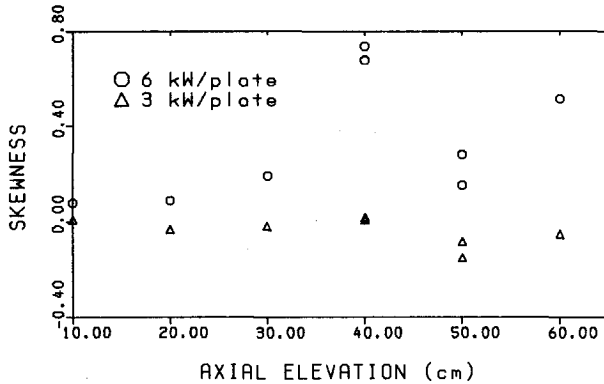


Figure 4.6: Skewness of the PDFs of SPND noise signals as a function of axial elevation in string 4.

In Figs. 4.5-4.7, the 2nd, 3rd, and 4th moment of the PDFs are shown as a function of the axial position; the corresponding data of the reference measurements with low heating power are indicated, too. The standard deviation (σ) increases in the upper core regions (see Fig. 4.5). Its maximum

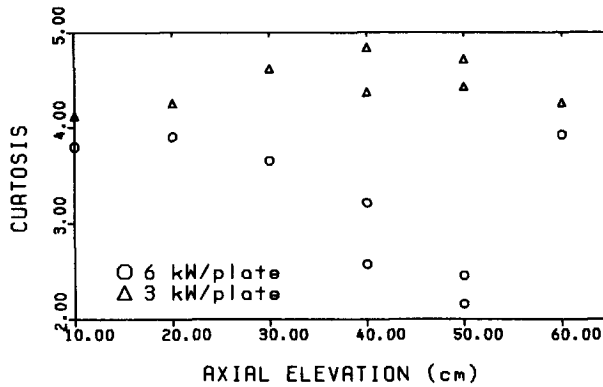


Figure 4.7: Kurtosis of the PDFs of SPND noise signals as a function of axial elevation in string 4.

value is close to 0.5 % and exceeds the values of σ without boiling by almost 10 times.

The skewness varies in a wide range along the channel (see Fig. 4.6). It takes small positive values at lower positions and has a positive maximum at 40 cm. The deviation from zero is a measure of asymmetry of the PDF; therefore, the large skewness (especially at 40 cm) can be attributed to the large difference between the peak at positive-, and the flattened region at negative signal values; see Fig. 4.4c.

Fig. 4.7 shows that the kurtosis drops below 3 at axial positions between 40 cm and 50 cm. This behaviour indicates the presence of bimodal flow [Vin82] at those positions. The kurtosis is always greater than 3 in the reference experiments (indicating a unimodal flow).

Summarizing the observations based on time-domain inspection of the SPND signals, it has to be emphasized that there is a predominantly homogeneous flow in the lower regions of the channels and bimodal flow in its upper half during experiments with 6 kW per plate. At an axial elevation of 30 cm, some periodicity is already noticeable in the time signal. The intensity of the fluctuations increases in the bimodal flow at 40 cm; the residence time of the low-void mode is large and constitutes almost half of the total ~ 4 s oscillation period. At 50 cm, the bimodality is still very strong; the residence time of the low-void mode decreases, and the difference between the properties of the modes ceases. At the highest position (60 cm), the bimodality almost disappears, and the magnitude of the fluctuations is

reduced.

The variance of the PDFs is significantly higher in the bimodal flow than in the case of the unimodal one. The skewness proved to be not very useful in the analysis. Finally, the kurtosis changes characteristically along the channel, and the condition given in [Lah78] for the description of two-phase flows is applicable in the present experiments as well. Namely, PDFs with kurtoses above and below 3 belong to unimodal and bimodal systems, respectively.

4.3.2 Neutron noise spectra and correlation functions

In Fig. 4.8, the normalized noise spectra, phase of the CPSD, and coherence is displayed for SPNDs at 50 cm (signal 3) and 60 cm (signal 4) in string 4. Both the CPSD and the coherence have a dip at 1 Hz, and below the dip frequency they have a strong peak. This peak indicates the presence of a low-frequency oscillation in the system.

Closer inspection of the low-frequency region shows that the frequency of the peak is $f_p = 0.225$ Hz; this yields an oscillation period of (4.45 ± 0.28) s. The coherence is large at the peak frequency, and the phase of CPSD has a well-defined, non-zero value in the neighbourhood of f_p . Above 1 Hz, the phase decreases slowly with increasing frequency (after eliminating the 360° jump).

Experiments with SPND positions 40-50 cm, 30-40 cm, and 10-20 cm, respectively, show in general similar behaviour as in the case of positions 50-60 cm, introduced in Fig. 4.8. However, a few peculiarities should be pointed out. At the lowest positions, the low-frequency peak of PSDs is missing; the phase is zero below ~ 2 Hz and undulates around zero at higher frequencies. At higher positions, the low-frequency oscillation is always present, and its strength depends on the axial elevation. This is seen clearly in Fig. 4.9, where the normalized autospectra of SPNDs are displayed for different axial locations in string 4. The peak is strongest at positions 40 cm and 50 cm, where also harmonics appear at multiples of f_p .

At the resonance frequency f_p , there is a phase-shift between SPND signals at 30-40 cm, 40-50 cm, and 50-60 cm. This shift is negative for detector combinations at 40-50 cm and 50-60 cm, respectively. It is remarkable that the phase shift is positive for the combination 30-40 cm. A negative phase-shift between detector signals A and B means that signal B lags behind A. A positive phase-shift has just the opposite meaning, i.e., A lags behind B. The values of the exact peak frequencies and the phase at f_p are given in

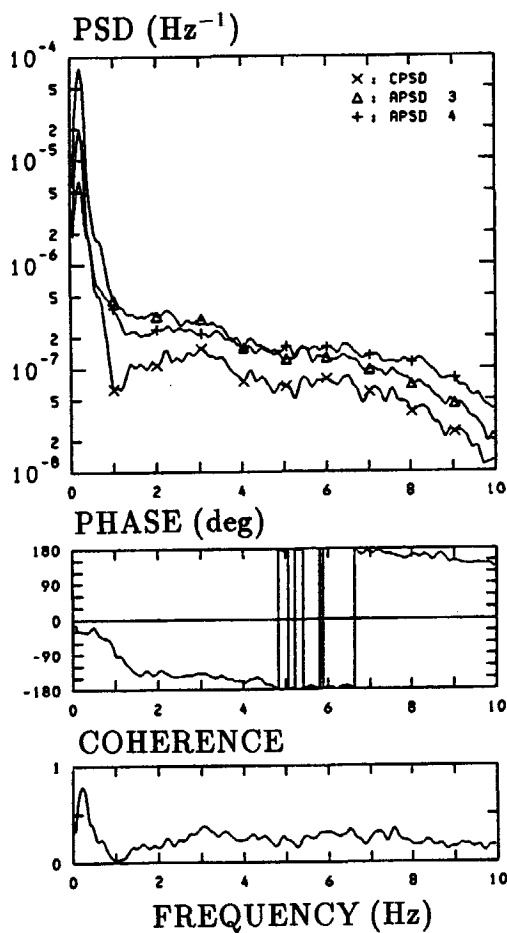


Figure 4.8: Spectra, phase of the CPSD, and coherence between noise signals of SPNDs in string 4; detector 3 - at axial position 50 cm, detector 4 - at axial position 60 cm.

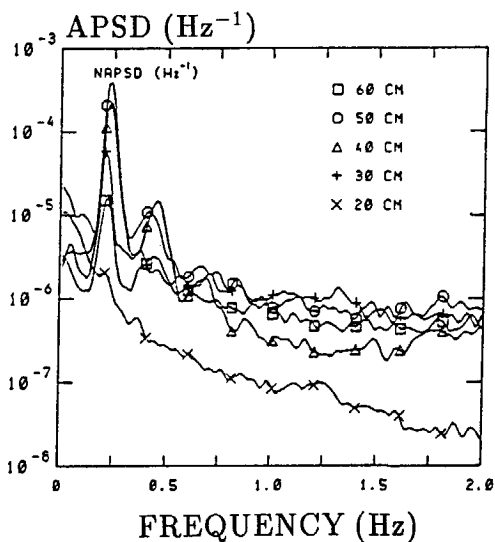


Figure 4.9: Axial evolution of the low-frequency resonance in string 4.

Table I. On the basis of these values, a transit time has been inferred for each combination, which is also given in Table I.

TABLE I
Transit times inferred from CPSD phases and CCFs

<i>position</i> (cm)	<i>CPSD</i>			<i>CCF</i>
	<i>f</i> (Hz)	$\varphi(^{\circ})$	$\tau(s)$	$\tau(s)^{\dagger}$
50-60	0.224	-26.71	0.331 ± 0.038	0.348
40-50	0.238	-27.31	0.318 ± 0.021	0.104
				0.348
30-40	0.210	30.07	-0.397 ± 0.035	0.139
10-20	no peak	0	0	-0.348
				0

$^{\dagger} \Delta \tau_{CCF} = 0.035$ s in every case

The main peak of the cross correlation functions (CCF) of SPND signals is shifted with respect to zero for SPND combinations in the upper half of the core, which is an indication of time-delay between the corresponding signals. This time-delay is positive between SPNDs at 40-50 cm and 50-60 cm, but

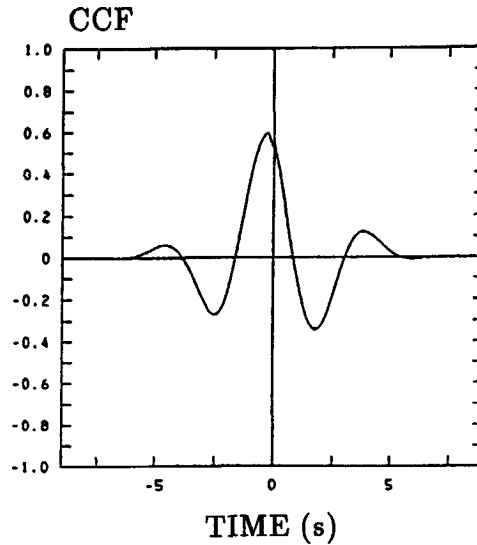


Figure 4.10: Cross correlation function between noise signals of SPNDs at 30 cm and 40 cm.

it is negative between signals at 30-40 cm. The CCF in this latter case is depicted in Fig. 4.10. The corresponding delay-time values are found in the last column of Table I. One should note that, at the highest positions, the CCFs have an additional peak at smaller transit times; these values are also indicated in Table I.

The interpretation of the above results and their application for the identification of two-phase flow characteristics follows next.

4.4 Flow identification

Let us analyse now in detail the results obtained in experiments with heating of 6 kW per plate, when boiling occurs along almost the full length of the plates. Several factors indicate the presence of slug flow regime in the coolant channels. Time signals of SPNDs at axial positions 40 cm and 50 cm (shown in Figs. 4.3b-e) clearly have a 'switching' character with a peak-to-peak variation of 1.5-2 % of the nominal signal level. Neutron flux variations caused by coolant density changes were analyzed by the code CITATION in Section 2. According to the results shown in Fig. 4.1, such variations are

generated by void changes of about 50 % at NIOBE.

Coolant states with low and high void fractions appear periodically nearby the SPNDs, and a peak arises in the neutron noise APSDs at 0.23 Hz. According to earlier two-phase flow investigations [Jon75], the presence of low-frequency peaks in spectra of the noise signals is typical for slug flow. The bimodality of the detected signals can be investigated via PDFs. For SPNDs at 40 cm and 50 cm elevations, the kurtosis is smaller than 3, which is again an indication of slug flow [Vin82]. On the basis of the above results, one can conclude that slug flow is present in the upper regions of the NIOBE. This slug flow, however, has a number of peculiarities discussed below.

Based on delay times inferred from CCFs and phase of CPSDs between neutron noise signals given in Table I and the known distances between SPNDs, one can infer the velocity values displayed in Table II.

The inferred velocities can be divided into two groups. The first group includes velocities with magnitude of 25.2 to 31.4 cm/s, which exceed significantly the nominal coolant flow velocity, 9.4 cm/s.

TABLE II
Velocities inferred from the phase of CPSD and CCF

position (cm)	v (cm/s)	v (cm/s)
50-60	30.3 ± 3.8	28.7 ± 3.2
		95.8 ± 33.5
40-50	31.4 ± 2.4	28.7 ± 3.2
		71.8 ± 18.7
30-40	-25.2 ± 2.5	-28.7 ± 3.2

For detectors at 30 and 40 cm, the inferred velocity appears go downwards, i.e., just opposite to the main coolant streaming. The velocities of the other group are much larger than the ones in the first group and can be as large as 70 to 100 cm/s; they are obtained by analyzing the second peak of CCFs.

The evaluation of the available TC signals helps to understand the underlying physical phenomena. Inspecting the time signal of the outlet coolant TC shown in Fig. 4.11, one finds that low-frequency temperature fluctuations of magnitude 8-10 °C take place in the coolant. The maximum coolant temperature is close to the saturation temperature. The coolant temperature is rather constant at this high level for about 2-2.5 sec. This period

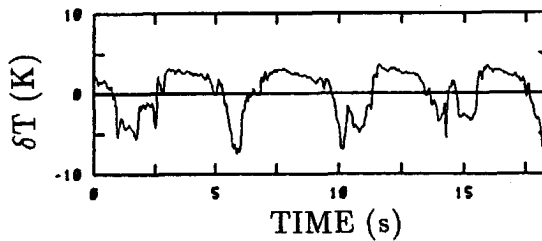


Figure 4.11: Time signal of the TC in the coolant at the channel outlet.

is followed by a drop in the coolant temperature, when highly subcooled coolant passes the TC. Consequently, in spite of the periodically occurring high void fractions, there is no saturated boiling in the channels.

In the following, a possible interpretation of the measured effects will be introduced. In the narrow channels, bubble detachment and coolant boiling do not take place in the conventional sense. In this case, bubbles developing close to each other sometimes join, stick to the wall, and without detachment move upwards [Bel88]. If this process continues, the size of the bubbles increases and void fronts propagate along the surface of the plates.

The exact description of the dynamics of the above processes, which leads to a system of nonlinear differential equations, is beyond the focus of the present study. Instead, a simple linear model is given in Appendix B. In the model, the boiling region on the plate surface is characterized by increased temperatures. Calculations show that this boiling region may expand with a relatively large velocity, when boiling with non-detaching steam bubbles occurs. This velocity may reach magnitudes of 20 cm/s or more, depending on the data of the numerical model.

When the bubble reaches a certain size, it does not grow further but slips out of the channel. After the slug has left the channel, there remains mostly single-phase coolant, and the whole process starts again. This periodicity can be the reason for the experimentally observed low-frequency fluctuations. The optimum conditions for the beginning of this process are between axial positions 30 and 40 cm, where the heat flux density and plate temperatures have their maxima. At lower regions of the channel (10 and 20 cm), no low-frequency peak is found in neutron noise spectra, so the slug does not extend to those positions, and its maximum length must be about 30 to 40 cm.

The coolant is mixed in the upper mixing volume of NIOBE after leaving the two coolant channels. Due to the mixing, the large density variations which occur in the channels are reduced above the plates. This effect can explain the decreased neutron noise variance at the highest position (60 cm), which is located in the direct neighbourhood of the channel exit.

On the basis of model calculations, the first group of velocities (of magnitude 25-31 cm/s) in Table II can be interpreted as the ones characterising the expansion of the region with large void fractions starting from a hot spot at an axial position of about 40 cm. The big bubble, stuck to the wall, reduces the effective channel cross-section. According to the indications of the flowmeters, the flow rate does not deviate significantly from the nominal value. Therefore, the cross-section is never blocked fully, and the coolant streams with increased velocity through the partially blocked channel. Inferred velocity values of 70-100 cm/s in Table II can be connected with coolant propagation in channels with reduced cross-section.

It has been shown in this chapter that the low-frequency oscillations in NIOBE can be interpreted as the ones caused by the special boiling phenomena in narrow rectangular channels, when bubble detachment does not occur in the usual sense. Instead, a vapour slug is generated, growing and moving upwards on the wall, and finally leaving the channel. The above process occurs periodically with a frequency of 0.23 Hz.

It is interesting to note that a similar phenomenon has been reported in an earlier boiling experiment at the HOR [Koz90a]. The channel width was 3 mm in that setup, and the oscillation occurred at frequency 0.4 Hz. Also, low-frequency oscillations have been observed during boiling in a simulated JRR-3 coolant channel [Sud86]. It is possible, therefore, that the results obtained at the NIOBE reflect some general properties of boiling in narrow channels and can be utilized for boiling detection in reactors with fuel plates.

4.5 Concluding remarks

1. Neutron noise analysis is a useful tool for analysis of actual boiling in an operating nuclear reactor. The following indicators proved to be applicable for two-phase flow regime identification:

probability density function (PDF) A significant increase of the variance of the neutron noise with respect to the case without boiling shows slug flow. Namely, variances greater than 0.2 % always indicate slug flow, while the variance of the single phase flow is 0.07 %. Also,

kurtosis values less than 3 serve as indicator of slug flow. This result is in agreement with the findings of [Vin82]. The skewness of the PDF, however, did not produce a consistent criterium for flow identification, contrary to the results introduced in the above reference.

power spectral densities (PSD) Neutron noise PSDs have a strong low-frequency peak (at 0.23 Hz), which is an indication of slug flow.

2. Using these indicators, coolant boiling in the narrow rectangular channels of a simulated MTR fuel assembly has been analyzed. Boiling took place in the assembly with heating power level corresponding to the nominal HOR power and with degraded cooling caused by the significantly reduced coolant velocities through the channels.
3. Boiling has a very peculiar character in this case. The results have been interpreted as partial channel blockage caused by interaction of steam bubbles in the channel. Various parameters of the process have been estimated, e.g., steam/water front velocity, maximum slug length, and slug residence time. The observed phenomena may be of use for boiling detection in reactors with plate-type fuel.

Chapter 5

Detection of Coolant Boiling Using Temperature and Neutron Noise†

Results concerning the detection of coolant boiling at NIOBE based on temperature noise are introduced. Applying the theory of boiling temperature noise, different stages of boiling (one-phase flow, subcooled boiling, and volume boiling) could be identified in the measurements analyzing the noise signals of the available thermocouples. It has been ascertained that neutron noise signals changed appreciably only when developed volume boiling took place in the channels. Neutron spectra did not vary at all at certain neutron detector positions, although developed volume boiling occurred at a distance of 3-4 cm from these detectors. This phenomenon has been applied to study the field-of-view of neutron detectors.

5.1 Introduction

Experiments introduced in this chapter have been performed not at NIOBE, but at an earlier boiling setup which was in operation from 1984 to 1986 at the HOR. It is similar to NIOBE regarding its main parameters [Hoo85], [Koz88b]. The differences can be summarized as follows. In the earlier version, all of the three fuel plates are cooled from both sides. There were

†This chapter is a shortened version of a paper published in *Kernenergie* [Academie Verlag, Berlin], Vol.33(4), pp.191-199, 1990; by R. Kozma, J.E. Hoogenboom, and H. van Dam.

4 coolant channels of width 3 mm each. At NIOBE, we have only two coolant channels of width 5 mm. The coolant flow rate can be adjusted and measured separately in the two channels of NIOBE. This was not possible in the earlier experiment, because it had only one loop with parallel coolant channels, and the value of the volumetric flow rate was not exactly known in the individual channels.

It is clear from temperature noise measurements that large differences exist between velocities in the different coolant channels due to certain alterations in their hydraulic characteristics. The minimum velocities were 5 - 6 cm/s, which are smaller than at NIOBE. At low velocities, saturated boiling occurred in the two inner coolant channels in the case of large heating powers.

After describing experimental circumstances, the theory of boiling temperature noise is given. This is followed by the characterisation of coolant boiling at NIOBE on the basis of the measured temperature noise. Finally, neutron noise effects are studied under different boiling conditions.

5.2 Experimental

Two strings of twin SPNDs and 7 TCs in the fuel plates have been used. The distance between the SPNDs in a string is 14 cm. One of the strings is located at the core side, the other on the reflector side of NIOBE. The schematic view of the location of the detectors is shown in Fig. 5.1.

Different thermohydraulic states of the coolant can be produced in the assembly by modifying the heating power and the flow rate. Three heating power levels (P) were applied during the experiments. The volumetric flow rate (V_{fm}) was fixed first at 300 l/h, then at 450 l/h for all 4 coolant channels together. Parameters of the experiments are given in Table I. Experiments with increasing serial numbers correspond to increasing heating powers.

The stationary temperatures recorded by TCs located in the plates give a good picture of the thermohydraulic conditions produced in the channels (see Fig. 5.2). The curves in Fig. 5.2 are calculated by spline fit of the experimental points. Dotted lines indicate the saturation temperature. The stationary temperature values can be used to draw some preliminary conclusions about the thermohydraulic state of the coolant in the assembly. There is one-phase flow in every measurement at the level of the lowest TCs. On the other hand, the 3rd and 4th level TCs in experiments III and 3 show very high temperatures, and their values exceed the saturation temperature

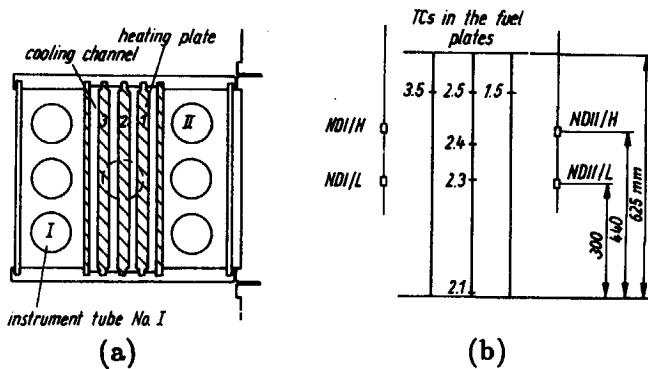


Figure 5.1: Schematic view of the measuring section

(a) radial cross-section, (b) vertical arrangement

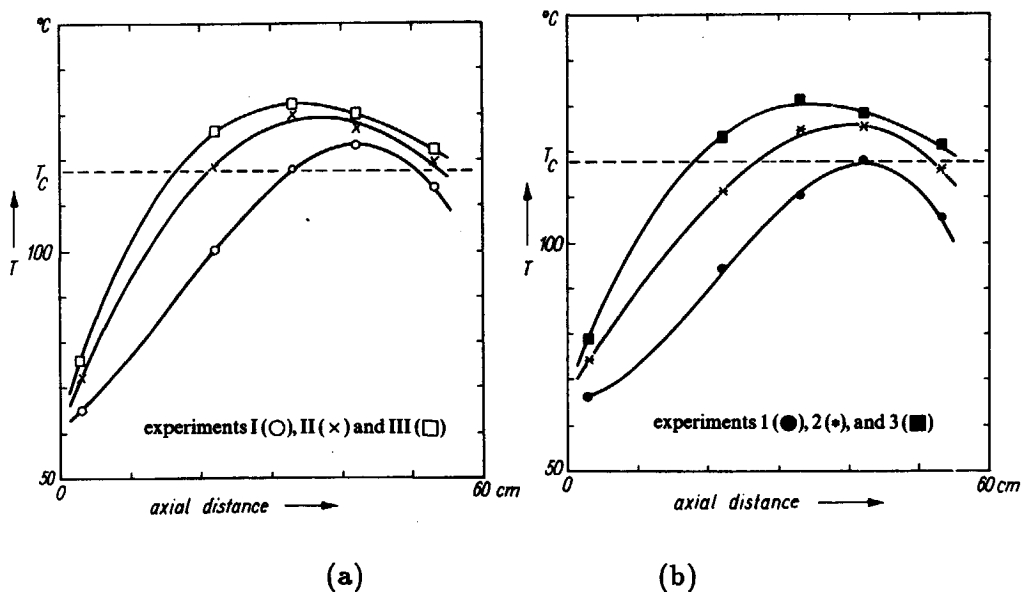


Figure 5.2: Stationary temperatures: (a) in experiments I, II, III, (b) in experiments 1, 2, 3.

The curves were calculated by spline-fit of the experimental points.

by about 10 °C or more. Those points are located close to the Jens- Lottes line (for details, see section 2.3 in Chapter 2), and coolant state with fully developed nucleate boiling is approached in experiments III and 3 at the position of TCs 2.3 and 2.4.

Table I
Parameters of the experiments

<i>Experiment</i>	I	II	III	1	2	3
<i>P</i> (kW)	9.5	14.0	18.2	9.5	14.0	18.2
<i>V_{fm}</i> (l/h)	300	300	300	450	450	450

Subcooled boiling may occur if the maximum wall temperature exceeds that of saturation by $\Delta T_{SAT;ONB}$. $\Delta T_{SAT;ONB}$ is about 3 °C in the present experiments according to the Bergles-Rohsenow criterion [Ber64]. The actual temperature of the surface might, however, differ from the measured temperatures due to several factors. The axial microstructure of the heat distribution in the plates shows periodic maxima and minima. The maxima occur in the surroundings of the heating wire, but the minima coincide with the positions of the TCs. Due to this effect, the measured temperatures always lag behind the maximum temperature at the plate surface. On the other hand, one has to consider that the TCs are built into the plates; thus they do not measure the surface temperature. The temperature indicated by a TC is higher than the surface temperature around that TC.

It has been found in Chapter 2 that the magnitude of this effect is in the order of 1 °C. The maximum temperature of the surface may exceed the maximum of the temperatures recorded by TCs in the plates. Thus, subcooled boiling may occur on the surface, not only when onset of nucleate boiling margin is reached at the position of one of the TCs, but at lower temperature indications as well.

If all the thermohydraulic properties of the assembly, i.e., heat losses, pressure drop coefficients, and flow rates were known in each channel, the boiling state of the coolant could be determined exactly in the channels. In the present experiments, however, most of these parameters are unknown. In this case, only a few very characteristic flow patterns, namely one-phase flow and developed volume boiling, can be identified on the basis of the stationary temperature values. The transition between these two states and, consequently, the onset of boiling cannot be studied in this way. Analysis of the noise components of TC signals will be used for that purpose.

5.3 Description of temperature noise at subcooled boiling : an overview

Features of temperature fluctuations are studied. It will be pointed out how the onset of boiling can be recognised on the basis of measured power spectral density functions (PSD) of temperature noise.

A great deal of theoretical and experimental work has been done to analyse thermohydraulic properties of non-equilibrium, two-phase flow [Del77], [Ish75]. Katona's ideas regarding boiling temperature noise [Kat78] have been applied and developed further during the experiments at Rheinsberg NPP. Results of these latter works have demonstrated that noise signals of neutron detectors and TCs are suitable for investigating the thermohydraulic state of the coolant [Col86], [Wer86]. In the following, the main results of these experimental works are summarized.

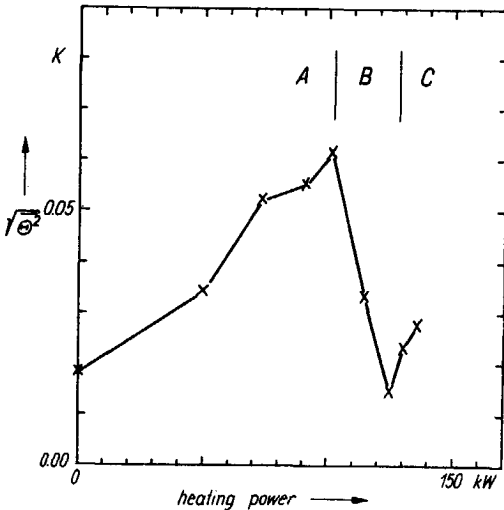


Figure 5.3: Intensity of temperature fluctuations as a function of the heating power [Kat78].

An important feature of the TCs is that they give a signal which is averaged spatially over their sensitive volume. Moreover, due to their thermal inertia, TCs average out to a certain extent in time domain as well. The intensity of the coolant temperature fluctuations changes in a very characteristic way with increasing heat flux density according to measurements of [Kat78]. In Fig. 5.3, $\Theta(t)$ is the fluctuating part of the measured temperature

signal. Results in Fig. 5.3 are obtained on an out-of-core thermohydraulic loop with upward flow of the coolant in an electrically heated tube, where temperature fluctuations have been measured in the upper part of the tube.

Three characteristic parts are found in Fig. 5.3. Detailed analysis of the thermohydraulic conditions shows that these parts correspond to subcooled boiling (A), saturated boiling with bubbly or slug flows (B), and annular flow (C), respectively. It is remarkable that temperature fluctuations increase with increasing heating power in the flow with subcooled boiling and decrease as soon as the state of volume boiling has been reached. These results have been checked at the experimental fuel assembly placed in the core of the 70 MW Rheinsberg NPP. The flow rate through the assembly could be reduced by a special valve, thus inducing different types of boiling. It is seen in Fig. 5.4 how the intensity of temperature fluctuations vary when more and more steam emerges by reducing the flow rate. The significant increase followed by the decrease of the intensity is obvious for TCs at higher positions, while there is a continuous growth in the intensity of temperature fluctuations at the bottom.

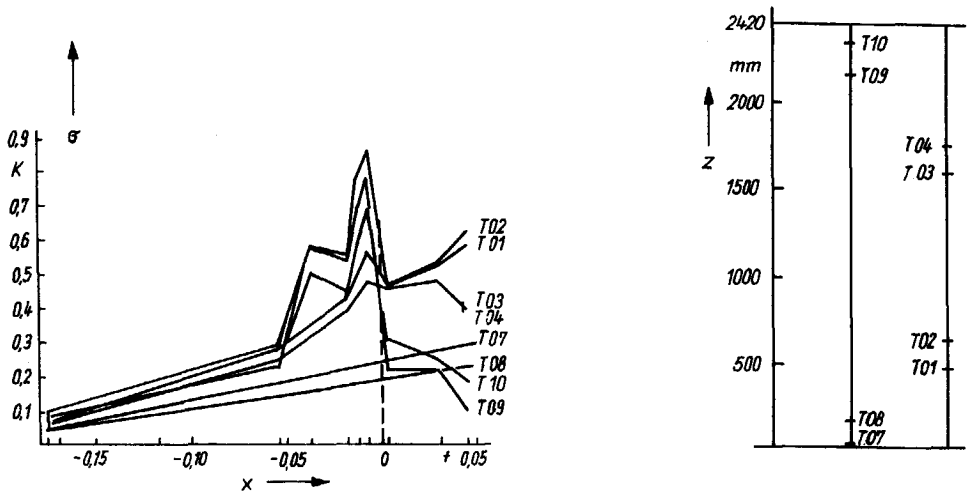


Figure 5.4: RMS of temperature fluctuations as a function of steam content x [Wer86].

Results shown in Figs. 5.3 and 5.4 have been interpreted as follows [Kat78], [Wer86]. Fluctuations of the coolant temperature are partly of external origin with regard to the core. These inlet temperature fluctuations

enter the core, propagate, and attenuate in the coolant channels.

The other part of the temperature fluctuations is generated inside the channels due to the turbulent heat transfer processes between the heated plates and the coolant. In single-phase flow, the temperature fluctuations grow when the heating power is increased because of intensification of the turbulent heat transfer processes. In this case, the intensity of temperature fluctuations is proportional to the gradient of coolant temperature [Bat76].

There are several reasons for increased temperature noise during subcooled boiling (region A in Fig. 5.3 and the first part with increasing effective values of temperature noise in Fig. 5.4). The first reason is the big difference between the temperature of the coolant and the bubbles having temperature of saturation. Additionally, large radial temperature gradients in the subcooled flow result in increasing turbulence, which yields still higher temperature fluctuations. Finally, because of the stochastic character of the generation of bubbles, the amount of heat transferred to the coolant has unequal distribution in time, which contributes to increasing temperature fluctuation.

According to experimental investigations [Wer86], the magnitude of temperature noise spectra increases at low frequencies when subcooled boiling occurs. This behaviour indicates that the above-mentioned thermohydraulic effects in the non-equilibrium, two-phase flow have relatively low-frequency character.

Temperature fluctuations in the sensitive volume of a TC decrease as the state of saturated boiling is reached via increasing the heat flux density or diminishing the flow rate. Approaching saturation, the radial temperature gradient in the bulk of the coolant decreases, thereby reducing turbulence. Both the water and the steam phases are at saturation temperature in saturated boiling. These effects yield falling RMS values, as is seen in section B in Fig. 5.3 and in the neighbourhood of $x = 0$ in Fig. 5.4.

The temperature of the water and the steam is the same in saturated boiling; thus temperature fluctuations cannot arise from temperature differences between the phases. There are temperature fluctuations in the coolant in this case, too, due to the variation of saturation temperature determined by pressure fluctuations. This behaviour is seen in region C of Fig. 5.3 and in the part with the highest values of steam content in Fig. 5.4.

The behaviour of temperature noise RMS described above directly influences the magnitude of the temperature noise spectra. In single-phase flow, the magnitude of the temperature noise APSD increases in a wide frequency range, due to the intensification of turbulent heat transfer processes. When

increasing the heat flux density, subcooled boiling begins at a given surface position. The magnitude of APSDs of temperature fluctuations strongly increases at low frequencies if subcooled boiling occurs. The increase ceases with the onset of saturated boiling. The significant growth of RMS temperature noise is an efficient indicator of subcooled boiling. Further on, the results of HOR experiments will be analysed on the theoretical basis introduced above.

5.4 Temperature noise at different levels of boiling at NIOBE

First, temperature noise field in single-phase flow will be studied. In Fig. 5.5a, temperature noise APSDs of the lowest TC in the middle plate are shown. The APSD curves are continuously shifted upwards when the heating power is increased. The amplitude of the temperature noise increases at each frequency with increasing heating power. On the basis of data presented in Fig. 5.2, it has been concluded that there is one-phase flow at the lowest TC level in every measurement. This conclusion is supported by results of Fig. 5.5a, for continuous growth of temperature fluctuations in a wide frequency range is typical for one-phase flow.

This picture, however, changes for TCs at higher elevations. Figs. 5.5b to 5.5d correspond to TC positions in the middle and upper part of the core. There is no continuous shifting of the curves any more; instead, several curves cross each other. With increasing heating power, the magnitudes of the temperature APSDs increase at some frequencies and remain unchanged or even decrease at others.

The magnitude of the temperature APSD is high in Figs. 5.5c and 5.5d at low frequencies (below 1 Hz) during experiment I, i.e., at the lowest heating power level. This remarkable feature disappears in both figures when the heating is increased (experiment II). In experiment II, the APSD magnitude was reduced considerably below 1 Hz and increased slightly at higher frequencies in comparison with experiment I.

This behaviour can be explained as follows. TCs 1.5 and 3.5 detect subcooled boiling in case I and saturated boiling in cases II and III, as large APSD magnitude at low frequencies followed by a drop with increasing heating power is a feature of the subcooled boiling \rightarrow saturated boiling transition.

No such decreasing, low-frequency magnitude of the temperature noise

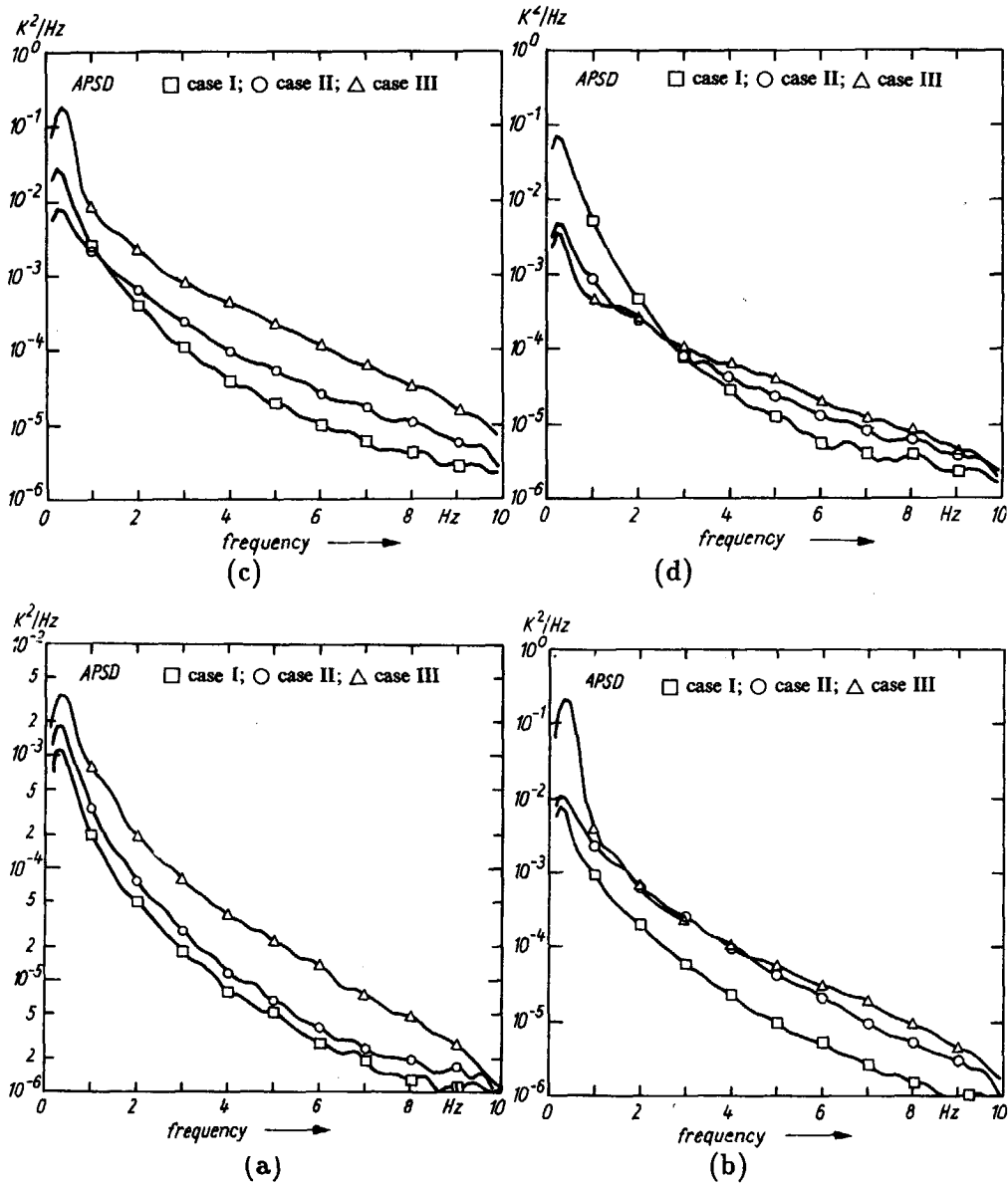


Figure 5.5: Temperature noise APSDs of (a): TC 2.1 (b): TC 2.3 (c): TC 1.5 (d): TC 3.5.

APSD is found at the upper TCs of the middle plate (2.3, 2.4, and 2.5) when comparing experiments I and II. Thus, subcooled boiling cannot be exactly localized in this case. However, by analyzing the axial dependence of the temperature noise RMS, important conclusions can be drawn.

Three RMS curves are depicted for the middle plate TCs in Fig. 5.6. Each of them contains 5 measured points fitted by spline functions. In every measurement, the RMS increases when moving from the lowest position to the middle of the plate and continuously decreases when moving towards the top of the plate. During experiment II, there was a remarkable increase at the half height of the core, especially at the position of TC 2.3. This behaviour can be explained by the effect of the coolant boiling that starts at medium elevation in a cooling channel adjacent to plate 2. The maximum of the RMS curve shifts to lower positions when a higher power level was applied (experiment III). This is in full agreement with the fact that ONB was reached at lower axial positions during experiment III than during experiment II.

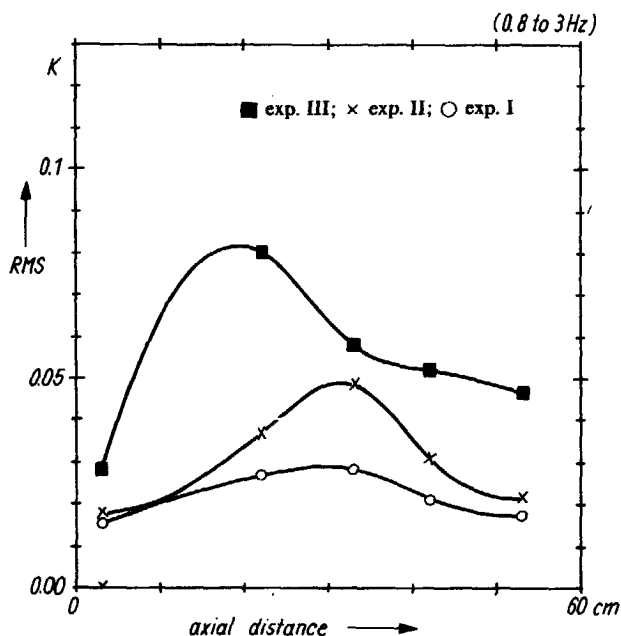


Figure 5.6: Axial dependence of the temperature RMS; experiments I, II, III.

On the basis of temperature RMS analysis, one can conclude that coolant boiling starts in the middle of the plates during experiments II and III. This boiling develops further in the upper part of the core. Subcooled boiling has been identified in the two outer channels during measurement I.

The similarity in the behaviour of TCs 1.5 and 3.5 obtained during experiments I and II disappears when a higher power level is applied (compare curves III in Fig. 5.5c and Fig. 5.5d). In the case of TC 3.5, curve III changes only slightly compared to curve II. This behaviour indicates that temperature fluctuations stay more or less unchanged upon reaching the saturated boiling state of the coolant.

TC 1.5 detects a considerably increased temperature noise field at the highest power level. This effect is interpreted in the following way. One of the coolant channels, which is adjacent to the first fuel plate, differs a little from the others so far as technical features are concerned. These differences lead to the presence of increased void fractions in that particular channel. Large void contents result in high hydraulic resistance in the narrow channels, so thermohydraulic instabilities may occur. The steam leaves the channel periodically in the form of larger and smaller steam packets. Detailed analysis of the measured temperature noise supports this conclusion. In Fig. 5.7, results of the analysis with frequency resolution 0.02 Hz are depicted in the region from 0 to 2 Hz. Most of the temperature APSDs show a distinct peak at 0.4 Hz. Only the TC of the first plate (TC 1.5) and the lowest TCs of the middle plate (TC 2.1 and TC 2.2) do not show this effect. Moreover, the APSD of TC 2.3 has higher harmonics as well.

The low-frequency peak in the APSD of TCs 2.3, 2.4, and 2.5 in Fig. 5.7 indicates that the high void fluctuation detected by TC 1.5 is registered by the upper TCs of the middle plate as well. TC 3.5 did not detect this low-frequency phenomenon. Thus, the high void fluctuation of experiment III must be closer to the first and second plate than to the third one. On the other hand, TC 2.1 and TC 2.2 at the lower part of the plate do not detect the low-frequency void fluctuation. Thus, this effect takes place in the upper regions of the assembly.

Summarizing the main results of the present section, it has to be mentioned that subcooled boiling has been detected in the two outer channels during experiment I. There was saturated boiling in the middle and upper part of the assembly in experiments II and III. Applying the highest heating power (case III), high void contents were present next to plates 1 and 2 in the upper regions of the assembly. The steam leaves the channel periodically in the form of steam packets (slug-type flow) during experiment III.

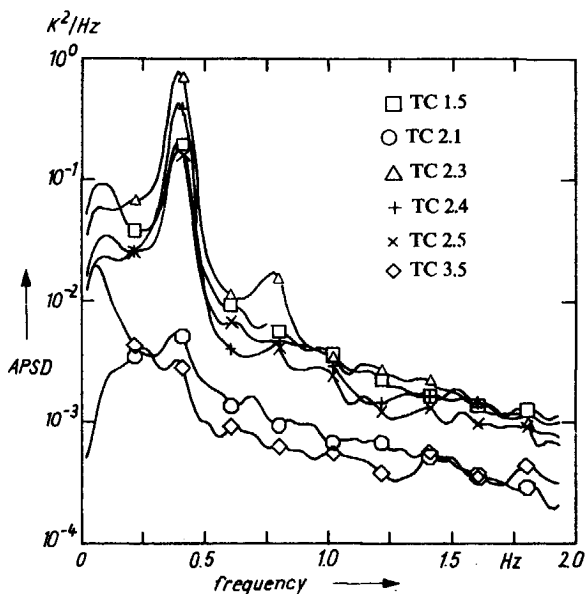


Figure 5.7: The low-frequency resonance in the temperature noise

The characteristic time constant of the process is 2.5 sec. This value is about half the oscillation period reported at NIOBE (Chapter 4). The difference between the channel geometries and flow conditions can be responsible for the different values of the oscillation periods.

The plate temperatures are usually lower in experiments with 450 l/h volumetric flow rate than in the case of 300 l/h; compare Figs. 5.2a and 5.2b. The difference, however, is not too large. Temperature noise spectra at flow rate 450 l/h (experiments 1, 2, and 3) are similar to the ones shown in Figs. 5.5a-d, and they can be interpreted analogously [Koz90a].

The RMS curves of the TCs at the middle plate are shown in Fig. 5.8 for experiments 1, 2, and 3. There is no characteristic peaking of curve 2 at the TC 2.3 position, contrary to curve II in Fig. 5.6. This is due to better cooling in the case of higher volumetric flow rate and less intensive boiling in the 2nd case compared to case II. The increased overall temperature noise level at higher volumetric flow rates can be interpreted as the result of the higher coolant velocity and larger turbulence. Further increasing the heating power, the RMS will have a maximum at the position of TC 2.3, i.e., the maximum is shifted towards higher axial positions compared to curve III in

Fig. 5.6.

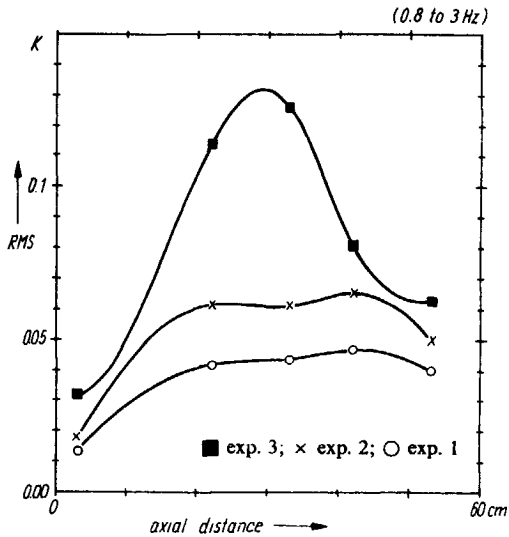


Figure 5.8: Axial dependence of the temperature RMS; experiments 1, 2, 3.

5.5 Neutron noise measurements

The coherence of noise signals of two SPNDs is close to one, and the phase of the CPSDs is nearly zero in experiments without boiling. The neutron noise field changes when boiling emerges in the channels. The magnitudes of the neutron APSDs increase in the regions with high void fraction while the coherence diminishes and the zero phase disappears.

The main goal of the present section is to reveal which stage of the boiling is indicated by neutron detectors and what kind of neutron noise features belong to the thermohydraulic states identified previously. In Fig. 5.9a-d APSDs of four neutron detectors are given. Curves of experiments I and II draw near to each other for every ND. This behaviour indicates that the NDs do not register differences between these two states. Also, the coherence functions and phases of CPSDs between NDs do not change when increasing power from level I to level II. Coherences are close to one up to about 5 Hz; phases of CPSDs are zero. It has been concluded from the thermohydraulic noise analysis that subcooled boiling takes place in the upper part of the assembly during experiment I, and that there was developed volume boiling

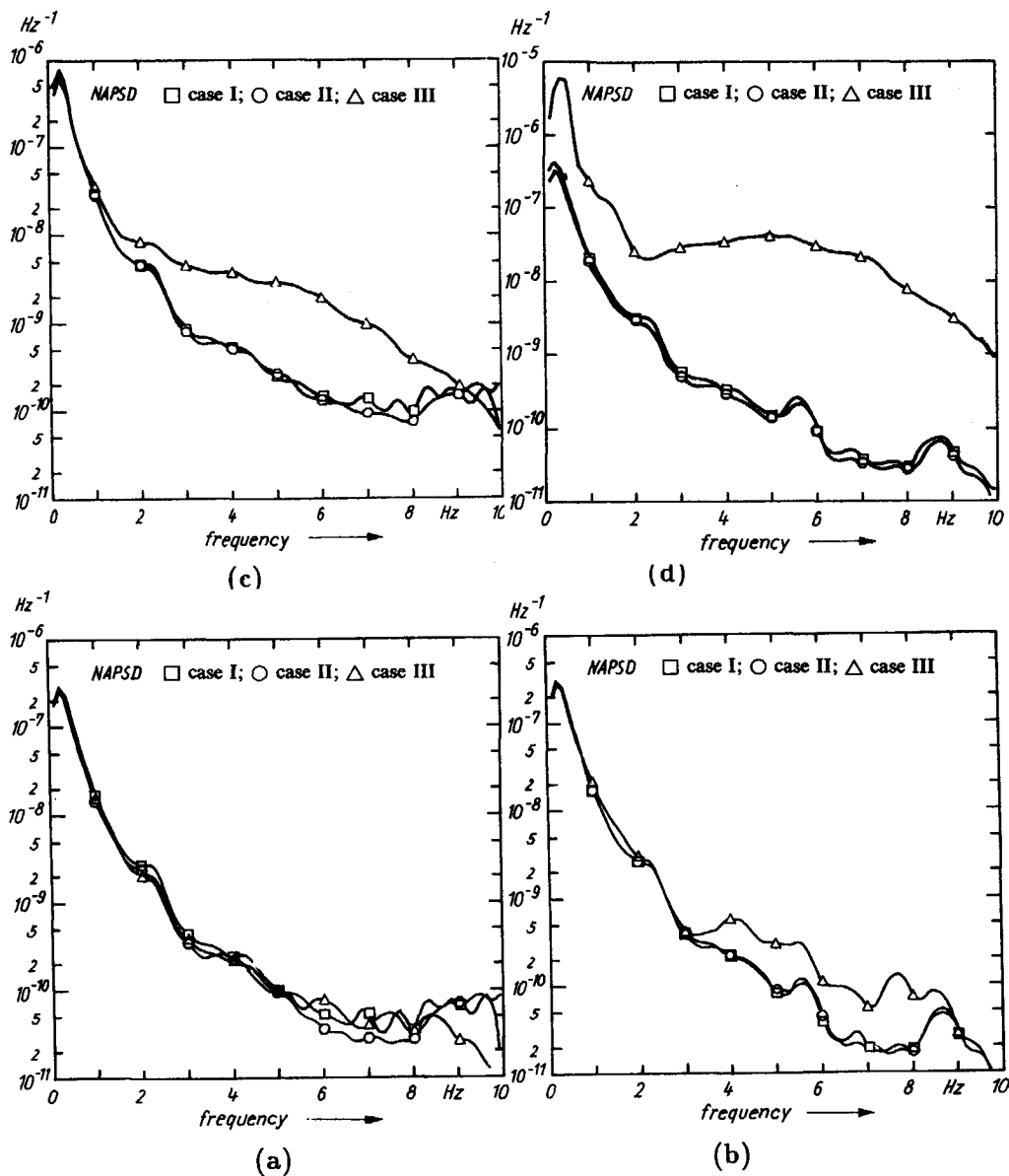


Figure 5.9: Normalized APSDs of the neutron noise; (a) lower SPND in the first string, (b) lower SPND in the second string, (c) higher SPND in the first string, (d) higher SPND in the second string

at the highest TC position during experiment II. None of the NDs indicates these effects.

The boiling detected by TCs 2.3, 2.4, and 2.5 must be very close to the NDs. The distance between the upper NDs and the fifth level TCs is 9-10 cm, between the upper NDs and TC 2.4 only 5 cm, and between the lower NDs and TC 2.3 about 3 cm. Coolant boiling in the upper half of the assembly had only a very short-range effect on the neutron noise field during experiment II. In this sense, the thermohydraulic perturbation was strongly 'localized'.

On further increasing the heating power (case III), the neutron noise field changes to such an extent that most of the measured neutron APSDs change as well. The upper NDs of both strings and the lower ND of the second string indicate variation in the neutron noise in experiment III. Only the noise spectrum of the lower ND of the first string does not change.

Fig. 5.9a-d is a nice example of the local/global theory of neutron noise [Wac74], [VDa76], [Beh77], [Dif80]. This theory will be summarized in Chapter 6 together with the quantitative analysis of the observed effects at NIOBE. Here, a short description of the local/global concept of neutron noise follows.

The neutron noise field in a nuclear reactor can be divided into two main components, namely local and global noise. The global component is important at low frequencies, and the scale of its spatial variation is comparable to the size of the core. On the other hand, the local component dominates at higher frequencies where the influence of the global component is negligible. The local component has a short-range effect only. Its spatial relaxation length is comparable with the thermal diffusion length of neutrons and is found to be a few cm in LWRs. The local component is attributed to fluctuations of the core parameters in the neighbourhood of the neutron detector (first of all coolant density fluctuations), while the global component is generated by reactivity fluctuations which propagate spatially through fission chains.

Very important progress in local/global theory has been made by [Kle81b], who showed that, due to feedback effects, the relaxation length of the global effect may decrease at very low frequencies (typically at a few tenths of a Hz). The space-dependence of the low-frequency neutron noise has been analysed further by [Koz85b], [Kat88].

Let us return now to Fig. 5.9. The increase of the high-frequency part of the APSDs is due to the local effect. The observation that the change of the SPND signals differs for different detectors proves that this boiling

effect is really of a local nature. On the other hand, no change is seen at low frequencies (except ND II/H) in accordance with local/global theory. The low-frequency increase of the APSD of ND II/H is due to the oscillating character of the boiling and will be discussed later in this section.

TC noise signals show that the coolant boiling in experiment III arose in the neighbourhood of the first and second plate. It is supposed that the differences in the behaviour of the SPND signals are caused by the differences in distance of NDs and the thermohydraulic noise sources. Taking into account the spatial arrangement of the NDs, a stronger effect is expected at the detectors of the second string. The magnitudes of the APSDs support the above assumption. Growth of the APSD magnitude is highest in the case of NDII/H, followed by NDI/H, and NDII/L. There is no significant variation in the spectrum of NDI/L.

A low-frequency peak appears in the APSD of NDII/H. By comparing APSDs of the upper two detectors in case III, it becomes clear that NDI/H indicates some boiling, but the low-frequency void fluctuation is still outside its field-of-view. At the same time, NDII/H detects both the boiling and the low-frequency void fluctuation.

Comparing neutron APSDs in one string, it can be seen that at higher frequencies (above 1-2 Hz) the magnitudes of the APSDs increase when taking higher axial positions, due to the increasing level of local density fluctuations (i.e., boiling).

An important conclusion of the present section is that NDs were insensitive to boiling in experiments I and II in spite of the fact that the distance between the detectors and the boiling was only 3 to 10 cm. The ND signals changed appreciably only at a high level of boiling during experiment III. This is caused by the limited range of the local neutron noise component.

Further detailed analysis of boiling neutron noise is necessary to determine the exact sensitivity margin of a boiling detection method based on monitoring the local neutron noise. This will be done in Chapter 6.

5.6 Conclusions

The aim of the present studies was to identify different stages of boiling in the HOR experiments. The electrical heating power was increased while the flow rate was maintained constant, thus inducing a single-phase flow, followed by subcooled boiling and, finally, by developed boiling in the experimental assembly. The conclusions of the experimental work are as follows:

One-phase flow and volume boiling could be identified on the basis of noise analysis of TC signals. The results are in agreement with the findings obtained with the help of stationary temperature values. Temperature noise analysis allows us to study subcooled boiling, and the thermohydraulic state of the coolant can be identified during the experiments.

Temperature noise signals showed the appearance of high void fraction fluctuations at the highest heating power. The steam produced in the narrow cooling channel formed steam packets which left the channel periodically. The characteristic time-constant of this process was 2.5 s. Fluctuations with the same period are present in certain neutron signals.

The first stage of coolant boiling (subcooled boiling and onset of boiling) could not be detected by SPNDs during the present experiments. This behaviour shows the limited field-of-view of NDs towards thermohydraulic disturbances. Only large void fraction fluctuations in measurement III caused remarkable changes in the neutron noise. Detailed quantitative analysis of the sensitivity of high-frequency neutron noise follows in Chapter 6.

Chapter 6

Boiling Neutron Noise at High Frequencies

In this chapter, the theoretical basis of high-frequency neutron noise is summarized. This is followed by experimental results obtained at NIOBE with the injection of non-condensable nitrogen bubbles and with actual coolant boiling. The sensitivity of the NRMS neutron noise method is evaluated on the basis of the experiments.

6.1 Introduction

In-core neutron noise of reactors with coolant boiling in their core has been analysed by a number of authors in order to determine local void fraction. There is a connection between intensity of the neutron noise and the void fraction in the coolant channels [Kos75], [Cee76], [Att78]. The interpretation of these results is based on the observation that bubbles in the streaming coolant disturb the neutron flux and generate propagating neutron flux perturbations. This is the parametric effect of thermohydraulic perturbations on neutron noise. Further experimental studies have been aimed at studying the connection between neutron noise intensity and the void fraction [Blu82], [Ber82], [Mit82].

The neutron flux fluctuates in the absence of boiling as well. Part of these fluctuations are concentrated at low frequencies. They are generated by reactivity variations and by thermohydraulic effects. In addition, there are always oscillations at certain well-defined frequencies which correspond to mechanical movements of reactor components or other parts of the pri-

mary system. In the case of a reactor with boiling, the boiling noise is superimposed on these effects which are regarded as background noise components in the framework of the present study. Boiling can be detected by noise methods if the boiling noise exceeds the background.

Fluctuations of the detector signal induced by boiling have a certain frequency content corresponding to the dynamics of bubbles and to the transfer properties of the reactor and the detectors. Boiling-induced neutronic fluctuations are detectable only if their frequency ranges overlap with the working frequencies of the reactor-detector system. This condition is usually fulfilled at frequencies of up to at least 20-30 Hz, when SPNDs have upper cut-off frequencies of 50 Hz or more and the reactor transfer-function cut-off frequency is about 20-30 Hz. On the other hand, boiling noise is of a wide-frequency character and extends from low frequencies to well above 50 Hz in the case of developed boiling.

The relationships between various neutron noise components have to be analysed in the actual measurement conditions in order to develop an objective void fraction detection method. In practical applications, usually the high-frequency NRMS (normalised root-mean-square) neutron noise is studied. The upper cut-off frequency is chosen according to the given experimental circumstances, and it may extend as far as 40-50 Hz. The background noise level is low at HOR, and its magnitude at high frequencies (above 2 Hz) is less than 0.01 % of the DC value. Due to the low background noise level, clear boiling effects can be identified at NIOBE above 2 Hz. These effects are studied thoroughly in this chapter.

6.2 Theory of boiling reactor noise

The presence of steam bubbles at a certain position in a nuclear reactor results in the variation of the local material parameters (macroscopic cross-sections and diffusion coefficients in the case of diffusion approximation). The response of a neutron detector to these types of parametric fluctuations can be evaluated by the powerful method of adjoint functions [VDa76]. Here, a brief description of this theory follows, in which two-group neutron diffusion equations are used. The one-group diffusion equation is too rough for the description of the neutron life-cycle which involves an energy scale of ~ 10 decades. On the other hand, the main conclusions of two-group theory regarding neutron noise decomposition remain in force in the case of n -group theory ($n \geq 3$) and one-group, slowing-down theory as well [Paz81].

Further on, the results given in [VDa76] are summarized. Let the fast and thermal neutron fluxes, Φ_1 and Φ_2 , be the solutions of the homogenous 2-group diffusion equations of a critical reactor. Introduce the fast and thermal adjoint 2-group diffusion equations with detector cross-sections Σ_{d1} and Σ_{d2} in the fast and thermal groups, respectively. The solutions of the adjoint equations are the adjoint fast and thermal functions, Φ_1^+ and Φ_2^+ , respectively. Neglect the effects of fluctuations of diffusion coefficients which are usually small in large reactor cores. The fluctuations generated by fast and thermal absorption cross-section variations are small compared to the effect of the moderation cross-section changes. The response of a detector which is sensitive only to thermal neutrons appears in this case [VDa76]:

$$\delta R(\mathbf{r}_1, \omega) = - \int_V \Sigma_{d2} \delta \Phi_2 dV = - \int_V \delta \Sigma_R(\mathbf{r}, \omega) \Phi_1(\mathbf{r}) \Phi_R^+(\mathbf{r}, \mathbf{r}_1, \omega) dV. \quad (6.1)$$

Here, $\delta R(\mathbf{r}_1, \omega)$ is the response in the frequency domain of a detector at position \mathbf{r}_1 ; and the notation $\Phi_R^+ = \Phi_1^+ - \Phi_2^+$ is used. The source term, $\delta \Sigma_R$, which is generated by void fraction fluctuations appears as:

$$\delta \Sigma_R(\mathbf{r}, \omega) = \frac{\partial \Sigma_R}{\partial \alpha} \delta \alpha(\mathbf{r}, \omega) = k_\alpha \delta \alpha(\mathbf{r}, \omega). \quad (6.2)$$

k_α is assumed to be constant in the present approximation. The cross power spectral density (CPSD) between two in-core neutron detectors will be calculated according to the relationship

$$CPSD_{\delta R \delta R}(\mathbf{r}_1, \mathbf{r}_2, \omega) = \delta R(\mathbf{r}_1, \omega) \delta R^*(\mathbf{r}_2, \omega) \quad (6.3)$$

Substituting Eqs. (6.1) and (6.2) into Eq. (6.3), one obtains

$$CPSD_{\delta R \delta R}(\mathbf{r}_1, \mathbf{r}_2, \omega) = \int_V dV \int_V dV' \Phi_R^+(\mathbf{r}, \mathbf{r}_1, \omega) \Phi_1(\mathbf{r}) k_\alpha^2 \cdot \quad (6.4)$$

$$CPSD_{\alpha \alpha}(\mathbf{r}, \mathbf{r}', \omega) \Phi_1(\mathbf{r}') \Phi_R^{+*}(\mathbf{r}', \mathbf{r}_2, \omega)$$

Here, Φ_R^{+*} denotes the complex conjugate of Φ_R^+ and $CPSD_{\alpha \alpha}(\mathbf{r}, \mathbf{r}', \omega)$ is the cross spectrum of the void fraction fluctuations between positions \mathbf{r} and \mathbf{r}' . In the following discussion, the APSD of the detector signal is considered which, is obtained by substituting $\mathbf{r}_1 = \mathbf{r}_2$ into the above equation.

Up until this point, our treatment was quite general. To proceed further, we have to specify the spectrum of void fraction fluctuations. Consider first the Poisson model [Kos75], in which the following assumptions are introduced with respect to the void fraction fluctuations:

- bubbly flow with low void fractions is considered;
- the production of bubbles is a Poisson-process, and there is no spatial or temporal correlation between distinct bubbles; thus there is no correlation between different radial positions, and the bubble spectrum is white;
- bubbles neither coalesce nor collapse while they pass through the core.

Then, the auto spectrum of void fraction fluctuations at a certain position is given by [Kos75]

$$APSD_{\alpha\alpha}(\mathbf{r}, \omega) = \frac{\alpha(\mathbf{r})}{v(\mathbf{r})} \bar{V}_B(\mathbf{r}). \quad (6.5)$$

\bar{V}_B denotes the average bubble volume. We restrict further studies to frequencies between 0.1 Hz and 20 Hz. Those frequencies belong to the plateau-region of the zero-power transfer function of the reactor [Dud76]. In this case, the frequency-dependence of $\Phi_R^+(\mathbf{r}, \mathbf{r}_1, \omega)$ can be neglected. By substituting Eq. (6.5) into Eq. (6.4), one sees that the APSD of a neutron detector signal generated by void fraction fluctuations is proportional to the ratio of the local void fraction and the steam velocity, independent of frequency.

In addition to the boiling neutron noise, the total signal of a neutron detector consists of a non-boiling component as well. According to experimental studies, this background component is restricted to frequencies below a few Hz, while the boiling noise is of importance at high frequencies. Calculations based on Eq. (6.4) support this conclusion [VDa76], [Beh79], [Dif80].

The quantitative characterisation of the noise intensity at a given frequency range can be given by the NRMS neutron noise. The NRMS neutron noise over frequencies f_1 to f_2 is defined as follows:

$$NRMS(\mathbf{r}, f_1, f_2) = \frac{1}{I_N} \sqrt{\int_{f_1}^{f_2} APSD_{NN}(\mathbf{r}, f) df} \quad (6.6)$$

I_N is the DC component of the detector signal. Taking into account that boiling neutron noise is uncorrelated with background noise, the $NRMS^2$ of the detector signal is written as:

$$NRMS^2(\mathbf{r}, f_1, f_2) = m \frac{\alpha(\mathbf{r})}{v(\mathbf{r})} + C, \quad (6.7)$$

where m and C depend on the position and the frequency but are independent of α or v .

The results of the Poisson theory of bubbling noise given in Eqs. (6.5) and (6.7) are widely used in reactor noise models [VDa76], [Mit82], [Ber82]. It is clear that these results can be valid only for low void fractions. Nevertheless, already in the article laying down the basis of the above theory [Kos75], these results have been used for the interpretation of neutron noise measurements with void fractions reaching 60 %.

Based on Bernoulli statistics of bubble dynamics, a model of void fraction fluctuations will be introduced in the next section. We will use binomial distributions without a transition to Poissonian distribution. In this way, the decrease of neutron noise intensity at high void fractions can be interpreted. In an extended model, the presence of temporal correlations (i.e., non-white character) of bubbling noise is allowed as well. This approach will be of use for describing slug flows.

6.3 Bernoulli statistics of boiling noise

Let us consider a Bernoulli variable with possible outcomes a and 0 and with probabilities of these outcomes $P(a) = p$ and $P(0) = q = 1 - p$. By repeating the observation N times, the possible sums of the outcomes are $0, a, 2a, \dots, Na$. The probability distribution is binomial in the case of N events [Jen68]:

$$P(ka) = \binom{N}{k} p^k q^{N-k} ; k = 1, 2, \dots, N. \quad (6.8)$$

The mean μ_B and standard deviation σ_B of the binomial distribution are given by

$$\mu_B = Nap, \quad (6.9)$$

$$\sigma_B = \sqrt{Na^2pq} \quad (6.10)$$

Assume that the appearance of bubbles in a unit volume around a certain spatial point \mathbf{r} obeys Bernoulli's law. This means that bubbles appear independently in different space-time points and that the possible outcome of an elementary observation volume is either a (a bubble has been observed) or 0 (no bubble is present). Here a denotes the void fraction increase induced by a single bubble. The probability of bubble appearance in the unit observation is the average local void fraction $\alpha(\mathbf{r})$ which, in turn, can be identified as the parameter p of the Bernoulli process: $P(a) = p = \alpha(\mathbf{r}), P(0) = 1 - p = 1 - \alpha(\mathbf{r})$.

Consider a system in which a maximum of N bubbles may take place at a time. In our boiling detection problem, this system will be that part of the sensitivity volume of the SPND where bubbles might appear. The autospectrum of void fraction fluctuations in the unit observation volume does not depend on frequency. Its variance, $\sigma_B^2(\mathbf{r})$, is obtained from Eq. (6.10):

$$\sigma_B^2(\mathbf{r}) = K_0 \alpha(\mathbf{r})(1 - \alpha(\mathbf{r})) \quad (6.11)$$

where $K_0 = Na^2$ is a constant which does not depend on the void fraction. After substituting Eq. (6.11) into Eq. (6.4) and assuming that $\Phi_R^+(\mathbf{r}, \mathbf{r}_1, \omega)$, $\Phi_1(\mathbf{r})$ and $\alpha(\mathbf{r})$ do not vary within the sensitivity volume of the detector, we obtain

$$NRMS^2(\mathbf{r}, f_1, f_2) = m' \alpha(\mathbf{r})(1 - \alpha(\mathbf{r})) + C' , \quad (6.12)$$

where m' and C' are constants which are independent of α .

Equation (6.12) indicates a parabolic relationship between $NRMS^2$ and α instead of the linear dependence in Eq. (6.7). Fig. 6.1 illustrates that the difference between Poissonian and non-Poissonian theories decreases towards low void void fractions. No background noise is considered in Fig. 6.1 for the sake of simplicity. The relative difference between variances of the binomial and Poissonian models is less than 10 % for void fractions up to 0.1. At higher void fractions, this difference quickly increases. Above $\alpha = 0.5$, the binomial model predicts decreasing variance contrary to the continuously increasing variance of the Poisson model. Taking into account that the Poisson distribution is a limit to the binomial distribution when $p \rightarrow 0$ ($Np = \text{const.}$), this conclusion is understandable. It is also clear that the Poisson theory is applicable for low void fractions only.

The assumption concerning spatial and temporal independence of bubbles is definitely not valid at void fractions above 0.2, due to bubble-to-slug flow regime transition [Vin82]. Therefore, the binomial model breaks down above approx. 0.2 void fraction. Part of the difficulties can be solved by introducing a modified binomial model, in which certain time-correlations are incorporated.

In the modified model, bimodal neutron noise generated by bimodal two-phase flow is considered. The bimodal noise is characterised by the following set of parameters: μ_1 and μ_2 , σ_1^2 and σ_2^2 , which are the expected values and variances of the first and second mode, respectively. An additional parameter is the relative occurrence α_L of mode 1, where $0 \leq \alpha_L \leq 1$. By making use of the above parameters, the following expressions are obtained for the

expected value μ_{BM} and variance σ_{BM}^2 of the bimodal noise

$$\mu_{BM} = \alpha_L \mu_1 + (1 - \alpha_L) \mu_2 \quad (6.13)$$

$$\sigma_{BM}^2 = \alpha_L \sigma_1^2 + (1 - \alpha_L) \sigma_2^2 + \alpha_L (1 - \alpha_L) (\mu_1 - \mu_2)^2 \quad (6.14)$$

The variance of the bimodal mixture is the sum of weighed variances of

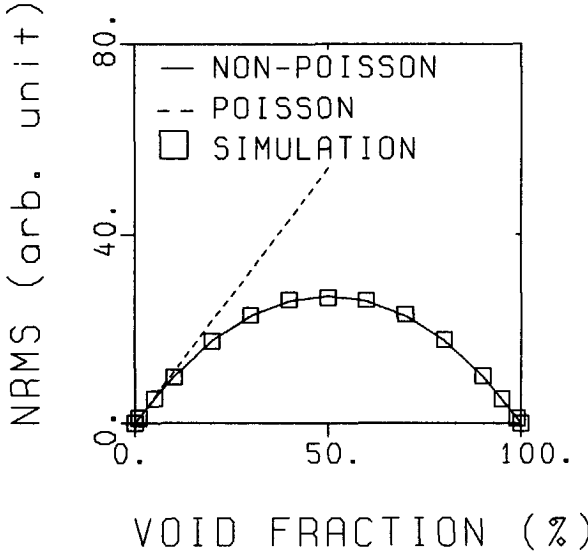


Figure 6.1: Variance of void fraction fluctuations according to model calculations.

Solid line : non-Poissonian theory; dotted line: linear approximation at low void fractions (Poisson theory); squares denote NRMS^2 evaluated from the APSD of a signal produced by computer simulation.

the separate modes and an additional term, which depends on the difference between the expected values of the two modes and on their relative frequency of occurrence (α_L). For $\alpha_L \rightarrow 1$ and $\alpha_L \rightarrow 0$, $\sigma_{BM}^2 \rightarrow \sigma_1^2$ and $\sigma_{BM}^2 \rightarrow \sigma_2^2$, respectively. When the parameters of the two modes are *a priori* known, the variance of the bimodal flow can be calculated from Eq. (6.14).

Consider the neutron noise generated by bimodal two-phase coolant. Let σ_1^2 and σ_2^2 be the variances of the two modes, both containing a background component ($\sigma_{i;bg}^2$) and a part induced by boiling ($\sigma_{i;boil}^2$). Assume that the difference between the expected values of the two modes is proportional to the difference of the void fractions. Then we obtain:

$$\sigma_i^2 = \sigma_{i;bg}^2 + \sigma_{i;boil}^2; \quad i = 1, 2, \quad (6.15)$$

$$\mu_1 - \mu_2 = c_\alpha(\alpha_1 - \alpha_2) \quad (6.16)$$

It will be assumed that the variances of the boiling components of each mode obey Eq. (6.12):

$$\sigma_{i;boil}^2 = c_o^2 \alpha_i (1 - \alpha_i); \quad i = 1, 2 \quad (6.17)$$

Substituting Eqs. (6.15)-(6.17) into Eq. (6.14), an expression is obtained for the variance of the bimodal noise as a function of 7 parameters:

$$\sigma_{BNI}^2 = f(\sigma_{i;bg}, \alpha_i, \alpha_L, c_o^2, c_\alpha),$$

where $i = 1, 2$. c_α stands for the void coefficient of the detector current which is assumed to be independent of the void fraction. On the other hand, c_o^2 is the void coefficient of the neutron noise variance at $\alpha = 0$, $c_o^2 = \partial \sigma_i^2 / \partial \alpha |_{\alpha=0}$. Its value can be calculated either by the Poisson bubbling noise theory or determined from measurements with low void fraction. The large number of parameters to be fitted from measurement data makes it difficult to use Eq. (6.14) in its complete form. In the following discussions, some simplifications will be introduced.

The boiling component of the first mode sometimes can be neglected with respect to that of the second mode. This is the case, for example, when the void fraction in the first mode is very low (or it contains no void at all), and the second mode has large concentration of bubbles. Another example is the slug flow with large regular bubbles (mode 1 with small $\sigma_{1;boil}^2$) which are separated from each other by a matrix of small bubbles (mode 2 with large $\sigma_{2;boil}^2$).

We will assume that the void fraction in the first mode is zero. The average void fraction of the total bimodal flow, α , can be expressed as $\alpha = \alpha_L \alpha_1 + (1 - \alpha_L) \alpha_2$. If $\alpha_1 = 0$, we obtain $\alpha_2 = \alpha / (1 - \alpha_L)$. The final expression of the variance of the bimodal noise is written:

$$\sigma_{BNI}^2 = \sigma_{1;bg}^2 \alpha_L + \sigma_{2;bg}^2 (1 - \alpha_L) + c_o^2 \alpha + \frac{\alpha_L c_\alpha^2 - c_o^2}{1 - \alpha_L} \alpha^2 \quad (6.18)$$

The value of α_L in Eq. (6.18), generally speaking, depends on the void fraction. In certain situations, however, this effect can be neglected and the variance of the bimodal signal has a parabolic dependence on the void fraction.

6.4 Periodic bimodal noise

In this section, bimodal signals with given expected values, μ_1 and μ_2 , variances, σ_1^2 and σ_2^2 , and existence probabilities of the two modes, α_L and $1 - \alpha_L$, are studied. We consider two cases with respect to the time distribution of the modes: (1) random distribution and (2) periodic alteration of modes in such a way that mode 1 comes for a period of T_1 followed by mode 2 during T_2 , then again mode 1 is present for time T_1 , and so on. For the standard deviation of the bimodal process we recall Eq. (6.14)

$$\sigma_{BNI}^2 = \alpha_L \sigma_1^2 + (1 - \alpha_L) \sigma_2^2 + \alpha_L (1 - \alpha_L) (\mu_1 - \mu_2)^2 \quad (6.19)$$

The standard deviation does not depend on the way the modes are distributed in time. The spectrum is frequency independent for the random distribution, but it has peaks at frequency $f_0 = 1/(T_1 + T_2)$ and at its harmonics in the case of periodic alteration of modes. The magnitude of the peaks decreases with increasing frequency. At frequencies much higher than f_0 , the peaks diminish, and the variances of the two modes determine the spectrum.

To illustrate the spectral effect of the periodicity, a computer simulation has been performed. Two normally distributed independent stochastic variables have been generated numerically, and a bimodal process has been produced by combining them randomly and periodically, respectively. Spectra of the resulting bimodal noise have been evaluated by standard techniques. The RMS of the spectrum has been determined over various frequency bands.

Consider a numerical example with the following parameters: $T = T_1 + T_2 = 4.5$ s, $\sigma_1 = 2.95$, $\sigma_2 = 1.0$, $\mu_1 - \mu_2 = 4.81$. The sampling time was 18 ms, and T_1 has been increased from 0 (no first mode is present) to 4.5 s (absence of the second mode). The RMS has been evaluated over various frequency regions. The calculated RMS^2 is shown in Fig. 6.2 as a function of $\alpha_L = T_1/T$ for different frequency bands. All the points are normalised to the value at $\alpha_L = 0$. In Fig. 6.2, the theoretical curve $\sigma_{th}^2 = -23.13\alpha^2 + 30.85\alpha + 1$ given by Eq. (6.19) is depicted as well. Points corresponding to the RMS^2 over frequency range (0 to 20 Hz) are marked by squares, and they are found on this curve. Above 1 Hz, i.e., at frequencies much higher than $f_0 = 1/T = 0.22$ Hz, the RMS^2 is in fact independent of the oscillation between the modes, and it is the weighed sum of the variances of the two modes. The corresponding points are marked by diamonds and triangles in Fig. 6.2.

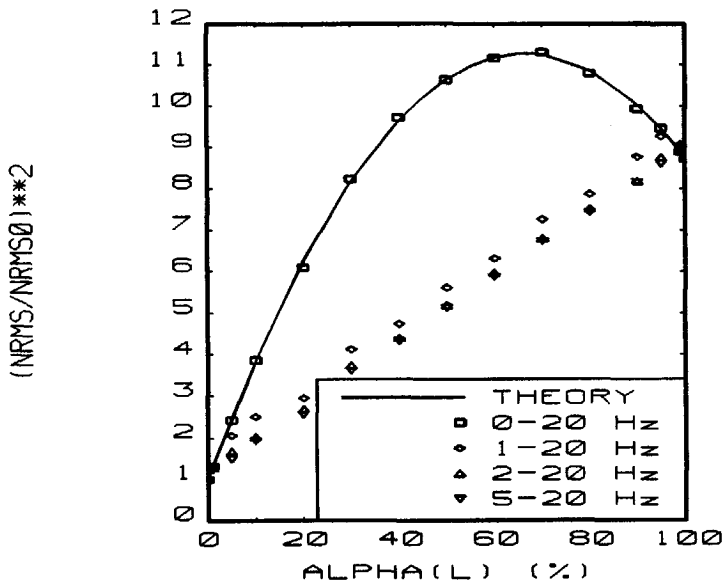


Figure 6.2: RMS of APSD of fluctuations in a simulated bimodal flow for different frequency regions.

The solid line shows the result of the bimodal model.

In the next discussions, experimental results are interpreted on the basis of the above findings.

6.5 Bubble injection experiments

6.5.1 Overview

The influence of density fluctuations on neutron noise can be investigated by injecting noncondensable gas (nitrogen, air, etc.) into the reactor channel. The advantage of this method is that the flow rate of the gas is a controllable quantity and, assuming that the propagation velocity of the gaseous phase is known in the reactor channels, the void fraction can be determined as follows:

$$\alpha = \frac{A_g}{A} = \frac{V_g}{v_g A}, \quad (6.20)$$

where A and A_g are the channel cross-sectional area and the area occupied by gas, respectively; V_g and v_g are the volumetric flowrate and the velocity of the gas, respectively. The disadvantage of the bubble injection methods is that the dynamics of the boiling process cannot be studied in this way.

Experiments with injection of noncondensable gas phase into the coolant channels have been performed by several authors both at research reactors and at (sub-)critical assemblies. These works revealed important aspects of boiling effects caused by bubbly flow [Fug77], [Kle79], [Por84] and other flow types [Alb82]. The relationship between the RMS neutron noise and the void fraction has not been treated there. In this section, results obtained at NIOBE concerning RMS neutron noise are given.

6.5.2 Experimental

Pure nitrogen gas was used in the experiments in order to minimize radiological effects. The upper end of one of the coolant transport tubes was connected to a vessel containing N_2 gas at high pressure. After opening a control valve, nitrogen pushes the water out of this coolant tube and enters the coolant channel at the bottom. N_2 bubbles move upwards in the water (which stands still) due to buoyance and leave the channel through another transport tube. The flow rate of N_2 gas is measured by a flowmeter (Krohne DK 47).

Noise signals of 4 SPNDs from instrument tubes 1 and 4 have been analysed. The notations ND1, ND2, ND3, and ND4 are used for SPNDs

at elevations 46 cm, 36 cm, 30 cm, and 20 cm above the channel inlet, respectively. The volumetric flow rate of nitrogen has been increased in 8 steps from a state without nitrogen to 21 cm³/s. The noise signal of the detectors has been recorded at each step for 30 min to achieve proper statistical accuracy.

A clear propagation effect is present in the neutron noise signals. Except for the lowest volumetric flow rates, the maximum of the cross correlation functions (CCF) is shifted with regard to zero time lag. Also, the phase of CPSD between signals of SPNDs deviates from zero and has a linear behaviour. The transit time of the propagation has been estimated by the CCF and the phase of CPSD as well. The results are given in Table I.

At the lowest volumetric flow rates, the effect of bubble transport was sometimes undetectable. In that case, no transit time was determined. The failure of ND1 is the reason for the missing data points during the experiment with 21.35 cm³/s volumetric flow rate.

TABLE I
Velocities inferred from noise measurements

No.	V_g (cm ³ /s)	ND1 - ND2			ND3 - ND4		
		$\tau(s)$		v_g (cm/s)	$\tau(s)$		v_g (cm/s)
		CPSD	CCF		CPSD	CCF	
1.	0.72	0.338	-	29.6	-	-	-
2.	1.78	0.326	0.331	30.7	0.296	0.286	33.7
3.	3.56	0.304	0.305	32.9	0.276	0.284	36.3
4.	5.34	0.269	0.271	37.2	0.245	0.261	40.7
5.	7.12	0.267	0.267	37.4	0.246	0.258	40.6
6.	8.88	0.250	0.249	40.0	0.231	0.243	43.3
7.	13.52	0.231	0.234	43.2	0.232	0.236	43.1
8.	21.35	-	-	-	0.205	0.216	48.7

Both τ_{CPSD} and τ_{CCF} decreases with increasing volumetric flow rate of N₂. The difference between transit times determined from the phase of the CPSD and the maximum of the CCF is less than 1.5 % of the determined τ value for detector pair ND1 - ND2. The differences are higher for the other detector pair. The CCF method always gives a higher estimation of τ than the phase fitting method (the difference varies between 1.7 % and 6.5 %). The presence of a wider range of actual velocities at lower axial positions is due to the peculiar character of bubble injection at the channel inlet. It gives rise to the difference between transit times determined by

these two methods close to the inlet (ND3 - ND4). The indicated velocities are determined from τ_{CPSD} . The inferred velocity increases with increasing volumetric flow rate of N_2 , but this increase significantly lags behind the increase of the volumetric flow rate.

The terminal rise velocity (v_∞) of a single bubble depends upon fluid properties and equivalent bubble diameter [Ton79]. Bubbles with diameters between 1 mm and 2 mm have terminal velocity between 20 cm/s and 35 cm/s. The velocities measured during the first 3 experiments can be velocities of individual bubbles. However, bubbles of spherical size cannot have terminal velocity of 40 cm/s or more in a rectangular duct of width 5 mm. High velocities can be caused by the movement of large, elongated bubbles (slugs) and by collective movement of bubbles.

The average void fraction is evaluated according to Eq. (6.19). It varies from 0.78 % to 14.77 %. Void fraction fluctuations have a very strong low-frequency component. In fact, a periodic movement of bubble/slug populations has been detected by SPNDs. This is illustrated by the normalised variation of time signals of ND2 in Fig. 6.3.

In experiment 1, the fluctuations are small, see Fig. 6.3a. Starting from Fig. 6.3b, two characteristic patterns can be distinguished in the signals. Pronounced negative peaks (dips) dominate the time signal for about 2.5 s. These dips are caused by passing N_2 bubbles due the negative void effect at the position of strings 4 and 1 described in Chapter 2. The magnitude of the relative variations reaches ~ 1 % in experiments with the highest gas volumetric flow rates.

The bubbling period is followed by a period of weak fluctuations (waiting period). These smaller fluctuations are similar to the ones observed during experiments without gas injection. It is concluded that there are no bubbles at the detector position during the waiting period. The entire behaviour appears periodically at every ~ 10 s with the lowest volumetric flow rate. By increasing the volumetric flow rate, the period decreases to 5 s in the case of the highest rates.

The conditions of injecting bubbles into the channel are rather peculiar in our experiments, determined by the geometry of the simulated assembly. Instead of having a circular orifice or a porous plate which are commonly used in bubble injection experiments, the bubbles are generated at a 6.15 cm long and 0.16 cm wide orifice at NIOBE. The presence of this orifice, in combination with the thin coolant channel, means that bubbles do not depart individually from the orifice but form a large gas slug at the bottom of the channel. After reaching a critical size, this slug finally detaches and passes

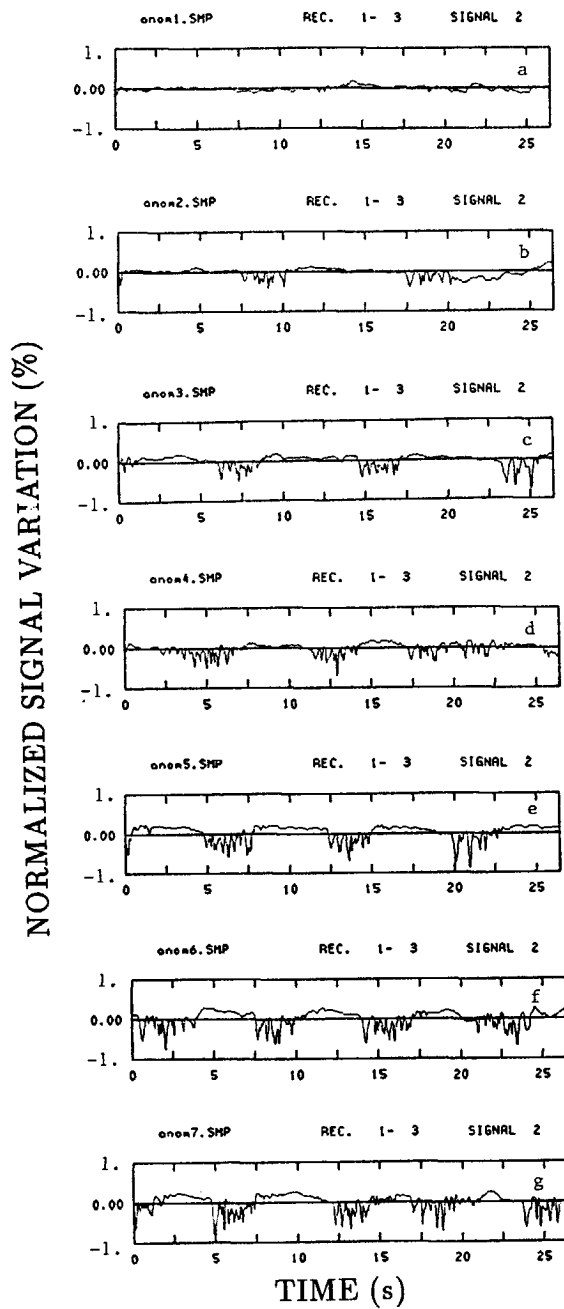


Figure 6.3: Time signal of ND2 in experiments 1 to 7.

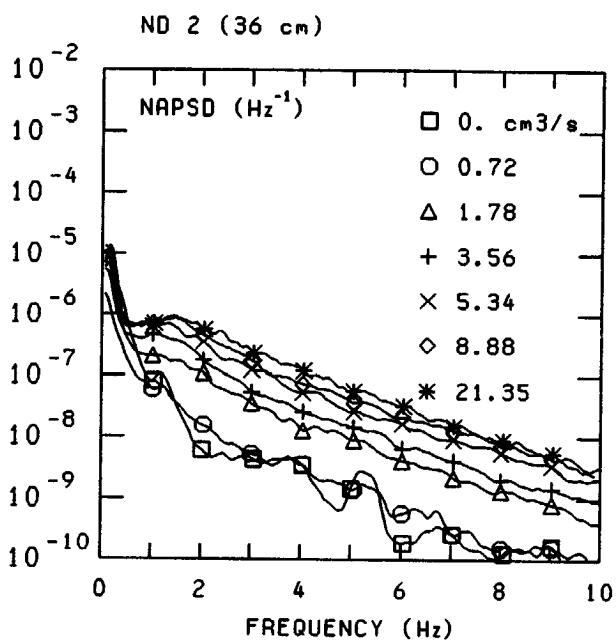


Figure 6.4: APSD of ND2 at different volumetric flow rates of N_2 .

through the channel.

The APSD of the noise signal of ND2 is given for some volumetric flow rates in Fig. 6.4. At the lowest volumetric flow rate ($0.72 \text{ cm}^3/\text{s}$), the high-frequency part of the spectrum does not change significantly compared to the case with no gas flow. By further increasing the volumetric flow rate of N_2 , the APSD clearly increases above $\sim 1 \text{ Hz}$. In order to characterise these changes quantitatively, NRMS neutron noise will be evaluated.

6.5.3 Analysis of neutron noise NRMS

The results are depicted in Fig. 6.5 in the form of an $NRMS^2$ vs. α/v plot, where α/v is obtained from data of Table I and Eq. (6.19). NRMS is evaluated over the $[0 \text{ Hz}, 10 \text{ Hz}]$ frequency region.

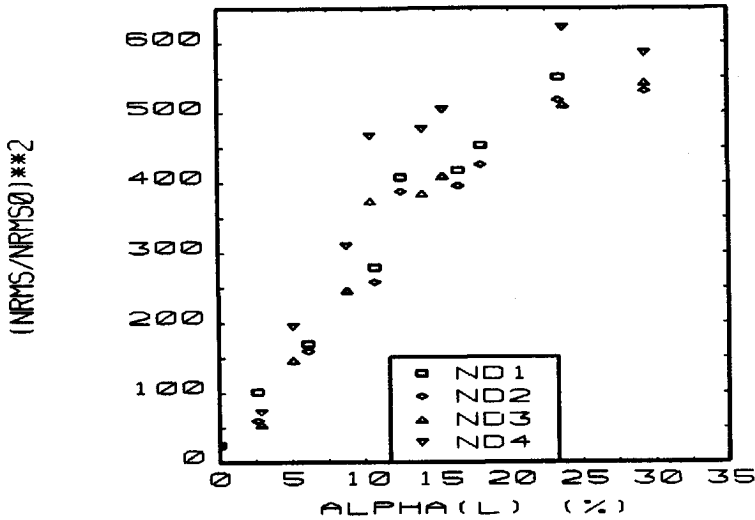


Figure 6.5: $NRMS^2$ vs. α/v in the bubble-injection experiments over frequencies $[0 \text{ Hz}, 10 \text{ Hz}]$.

After quick growth for lower α/v values, the $NRMS^2$ increases less intensively when $\alpha/v \geq 0.15 \text{ s/cm}$. In experiments with highest volumetric flow rates, the increase of the NRMS is very small and, for ND4, even a decreasing tendency is observed. This result contradicts the conclusions of the Poisson theory introduced earlier in this chapter, which predicts a linear relationship between $NRMS^2$ and α/v . This example shows that the Poisson theory indeed breaks down at higher void fraction.

Next, the high-frequency component of the neutron will be analysed. $NRMS^2$ values evaluated over the [1 Hz, 10 Hz] frequency region are shown in Fig. 6.6. The lines in Fig. 6.6 correspond to linear fittings of data points for each detector; the points with $\alpha/v = 0$ and $\alpha/v \geq 0.25$ s/cm have been excluded from the fitted data set.

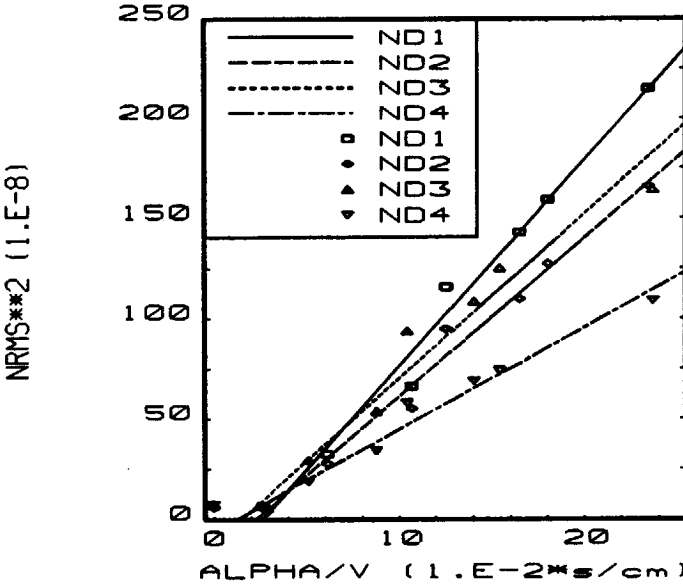


Figure 6.6: $NRMS^2$ vs. α/v plots, [1 Hz, 10 Hz]. The measurement points (with $\alpha > 0$) have been fitted linearly for each SPND.

The error of NRMS consists of two parts: the errors of the RMS of the spectra and of the measured DC signals, respectively. The relative error of the RMS is given by the relationship [Jen68]

$$\sigma_{RMS}/RMS = 0.5\sqrt{0.75/(Nn)}, \quad (6.21)$$

where N and n are the number of records and the number of spectrum points within the considered frequency region, respectively. The actual values were $N = 200$ and $n = 231$ in the experiments, which yield $\sigma_{RMS}/RMS = 0.2\%$. The DC level of SPNDs has changed by less than 0.3 % between different experiments. These changes had no clear trend. Finally, the error of the NRMS is less than 0.5%.

The error of α/v is 15%, which is dominated by the experimental error of the flow indication ($\sim 10\%$). The remaining part of the error is about equally distributed between the uncertainty of geometric dimensions and the error of transit time evaluation. In view of these error values, the linear fitting of the measurement points for $0.02 \leq \alpha/v \leq 0.25$ is satisfactory. This condition corresponds to void fractions $1\% \leq \alpha \leq 10\%$.

According to the Poisson theory (Section 6.2), a linear relationship is expected between $NRMS^2$ and α/v for an arbitrary frequency range. The experiments do not support this result. No void-effect is observed at $\alpha < 1\%$ at frequencies above 1 Hz. On the other hand, at large α values ($\alpha > 10\%$), the actual $NRMS^2$ is smaller than the value predicted by linear extrapolation.

Consider now the region of low void fractions ($\alpha \leq 1$) where no RMS increase has been detected. Similar behaviour has been observed in the experiments at the OSIRIS reactor, Saclay [Ber82]. It can be explained by the non-white character of the generating void fraction fluctuations [Kat83]. By assuming the dominance of low-frequency void fraction fluctuations (band limited fluctuations of α), a high-pass filter might eliminate the greater part of the boiling effect at low void fractions. Exactly this is the case at sub-cooled boiling when the boiling process is controlled by coolant temperature fluctuations which are of inherently low-frequency character. In the case of nitrogen injection experiments, no actual coolant boiling takes place. The fact that the $NRMS$ varies only slightly or does not vary at all for low void fractions indicates, however, that the spectrum of void fraction fluctuation is not white in this case either.

Let us apply the results of non-Poissonian theory of boiling noise (Section 6.3) for the interpretation of the deviation from the linear $NRMS^2$ vs. α/v function at high void fractions. According to Eq. (6.18), there is a parabolic relationship between $NRMS^2$ for the total frequency range and α . In Fig. 6.7, the $NRMS^2$ vs. α relationship is given together with a parabolic fit of the experimental points for each detector. Eq. (6.18) is used in the present case, because no remarkable void fraction is present in the neighbourhood of the detectors during the waiting period (mode 1) between two bubble populations according to the previous discussions. The coefficient of the quadratic term ($\varepsilon^{(2)}$) includes the void-coefficient of the local neutron flux (c_α^2) according to the following relationship $\varepsilon^{(2)} = \frac{\alpha_L c_\alpha^2 - \varepsilon^{(1)}}{1 - \alpha_L} \alpha^2$, where $\varepsilon^{(1)}$ is the coefficient of the linear term of the fit. Using the value $\alpha_L = \text{const.} = 0.6$, the void coefficient value of $c_\alpha = -1.132 \times 10^{-4}(\text{void } \%)^{-1}$ is obtained for ND1. The values corresponding to ND2, ND3, and ND4 are $-1.103 \times 10^{-4}(\text{void } \%)^{-1}$, $-1.113 \times 10^{-4}(\text{void } \%)^{-1}$, and $-1.265 \times 10^{-4}(\text{void } \%)^{-1}$,

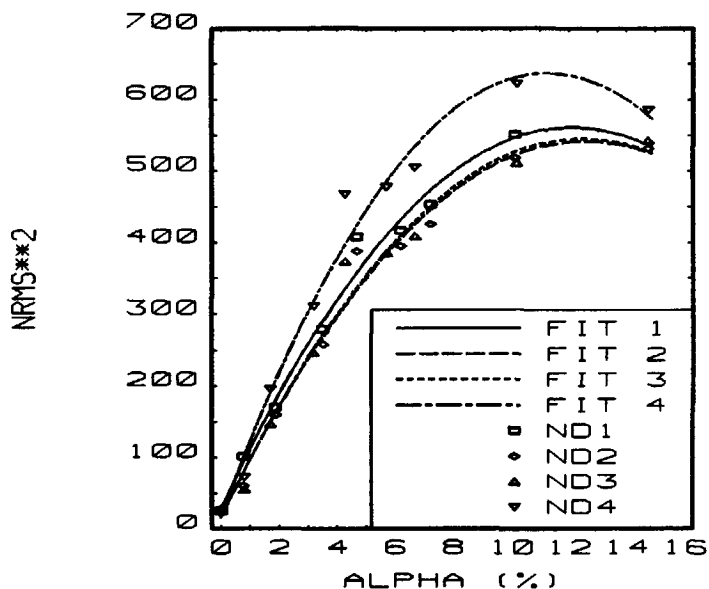


Figure 6.7: Non-Poissonian fit of the NRMS vs. void fraction function.

respectively. 2-dimensional (X-Y) multigroup diffusion calculations by CITATION introduced in Chapter 2 give a void coefficient by a factor of three higher ($c_{\alpha}^{calc} \approx -3. \times 10^{-4} (\text{void } \%)^{-1}$). In those calculations, homogeneously distributed void is assumed to be present in both coolant channels. During the actual experiments, however, bubbles are injected into one channel only. This can explain about half the difference. Moreover, the radial distribution of the nitrogen is not homogeneous in the coolant channel. Finally, also the simplifications made in the bubbling noise model ($\alpha_L = \text{const}$, $\sigma_{1;boil} = 0$), etc.) certainly contribute to this deviation between theory and experiment. Nevertheless, the non-Poissonian theory gives a better description of noise processes in two-phase flows than the linear model.

6.6 Experiments with subcooled boiling

6.6.1 General

The mean liquid enthalpy in the channels of NIOBE remains below saturation even at the highest heat power densities (which correspond to heating conditions of a nominal MTR-type fuel plate) because of the significant heat

losses and limited heating power.

Boiling at the two fuel plates next to the Contimet isolation is accompanied by excessive vibrations. It is caused by boiling in the narrow gap between the Contimet and fuel plates, which is normally occupied by water. These vibrations can be detected by accelerometers, and they result in periodic oscillations in the SPND signals. The appearance of these mechanical oscillations can be avoided by applying more intensive heating at the middle plate than at the other two. In this case, boiling takes place only at the middle plate, which is cooled from both sides by streaming coolant.

Experiments with various combinations of heating powers and flow rates have been performed under stationary and non-stationary conditions. In the present study, results obtained with a fixed average heat flux density of 91.1 kW/m^2 at the middle plate and with several heat flux levels at the other two plates are given. The mass velocity was fixed at a value of $227 \text{ kg/m}^2/\text{s}$ in both channels. The coolant was highly subcooled in the experiments. The coolant outlet temperature varied between 93°C and 97°C . Some slow temperature variations occur even at constant heating power and flow rate at NIOBE due to changes in the operational parameters of HOR.

6.6.2 Subcooled boiling description

The subcooled boiling region along a heated channel can be divided into two parts. The first part is called the wall voidage regime. During wall voidage, the wall temperature is sufficiently high for the incipience of boiling, but the main liquid volume is highly subcooled, and there is no significant vapour production. At a certain point, which is called the point of net vapour generation (NVG), bubbles leave the narrow boundary layer next to the wall, and intensive vapour generation starts. The void fraction itself is very small before the point of net vapour generation. The presence of wall voidage, however, yields a significant increase in the pressure drop and heat transfer coefficient and cannot be neglected in the boiling channels of nuclear reactors with high heat flux densities [Ton79]. The point of net vapour generation is given by the condition [Sah74]:

$$\begin{aligned} Nu_{NVG} &= 455 & \text{if } Pe \leq 70000 \\ St_{NVG} &= 0.0065 & \text{if } Pe > 70000 \end{aligned} \tag{6.22}$$

Here Nu , St , and Pe are the local Nusselt, Stanton, and Peclet numbers, respectively, defined as

$$Nu_{NVG} = \frac{q'' D_e}{k_c (T_s - T_{c,NVG})} \quad (6.23)$$

$$St_{NVG} = \frac{q''}{G c_{p,c} (T_s - T_{c,NVG})} \quad (6.24)$$

$$Pe = \frac{Nu}{St} = \frac{D_e G c_{p,c}}{k_c} \quad (6.25)$$

Here, the meanings of subscripts are: NVG - at the point of net void generation, c - coolant, s - saturation. Relationship (6.22) expresses the fact that thermal processes determine the net void generation at low mass velocities ($Pe \leq 70000$). On the other hand, at high mass velocities ($Pe > 70000$), hydrodynamic conditions prevail. Bubble detachment occurs as soon as the local Stanton number becomes 0.0065. This does not yield NVG in the case of thermally controlled regime, because the detached bubbles can exist only near the heated wall due to the very deep subcooling. Bubbles enter the subcooled liquid core only if $Nu \geq 455$.

Void generation is always thermally controlled at NIOBE, because $Pe = 17000$ at the highest possible mass velocities ($300 \text{ kg/m}^2\text{s}$). Nu remains far below 455 during the present experiments, with outlet coolant temperature between 93°C and 97°C . The actual Nusselt number is around 40, therefore, we are far away from the point of NVG.

The maximum wall superheat, $T_{11'} - T_s$, is about 10°C during the experiments with boiling. This value is much higher than the onset of nucleate boiling limit [Roh85], which is about 3°C in our case. The local St has been calculated as a function of the axial position based on the known heat flux density distribution. The local coolant temperature has been determined by assuming an average heat loss of 40 %. The calculations show that $St = 0.0055$ at medium axial elevations, and it reaches a value of 0.0065 at elevation 48 cm. The effective thickness of the bubble layer is $\sim 0.1 \text{ mm}$ at that point [Ton79], which means a void fraction of about 2% across the 5 mm wide channel. q'' drops quickly above an elevation of 50 cm, and the thickness of the bubble layer diminishes.

6.6.3 Neutron noise NRMS effects

In experiments with subcooled boiling, the coherence between SPNDs is close to unity up to about 2 Hz. The coherence decreases continuously above 2 Hz, and no significant coherence is measured at frequencies above 10 Hz. The

phase of CPSD is zero at frequencies where reasonable coherence is found, i.e., up to ~ 5 Hz.

Two experiments (A and B) have been performed with subcooled boiling of the coolant, while there was a single phase coolant in the channels during the reference experiment (C). The outlet coolant temperature was 95°C and 97°C in experiments A and B, respectively. Signals of SPNDs at axial positions 40 cm, 50 cm, and 59 cm are analysed in this section. The magnitudes of the APSDs of SPNDs increase at frequencies above ~ 2 Hz at positions 40 cm and 50 cm. This effect is seen in Fig. 6.8, where APSDs measured during experiments A, B, and C at axial position 50 cm are shown. On the other hand, this high-frequency increase of the APSD is not indicated by SPND at elevation 59 cm.

In order to characterise this effect quantitatively, the NRMS neutron noise has been calculated for different frequencies. In Table II, calculated NRMS values are given over frequency ranges [0.3 Hz, 1.5 Hz] and [2.0 Hz, 4 Hz]. $\Delta NRMS = NRMS_B - NRMS_{NB}$ is the difference between the NRMS measured in experiments with and without boiling.

According to Table II, there is significant change in the NRMS in both frequency ranges. This conclusion looks to be in contradiction of the visual inspection of Fig. 6.8.

One has to take into account, however, that the NRMS changes are suppressed by strong background effects at low frequencies ([0.3 Hz, 1.5 Hz]). The relative change in the NRMS is remarkable at frequencies [2 Hz, 4 Hz] and can reach 40% in the case of boiling. The error of the NRMS evaluation is about 0.5-1%, depending on the parameters of the experiment as it was described earlier in this chapter. The variation of the NRMS at low frequencies is just a few %. In the higher frequency region, however, the relative variation of the NRMS exceeds the statistical error at least 30 -40 times at positions 40 cm, and 50 cm and a clear boiling effect can be detected.

TABLE II
Variation of NRMS due to boiling

Detector position	0.3Hz-1.5Hz		2Hz-4Hz	
	$\Delta NRMS$	$\frac{\Delta NRMS}{NRMS}$	$\Delta NRMS$	(%)
	(10^{-5})	(%)	(10^{-5})	
40cm	0.35	1.99	0.71	32.54
50cm	1.08	6.24	0.93	40.08
59cm	0.84	4.93	0.23	7.53

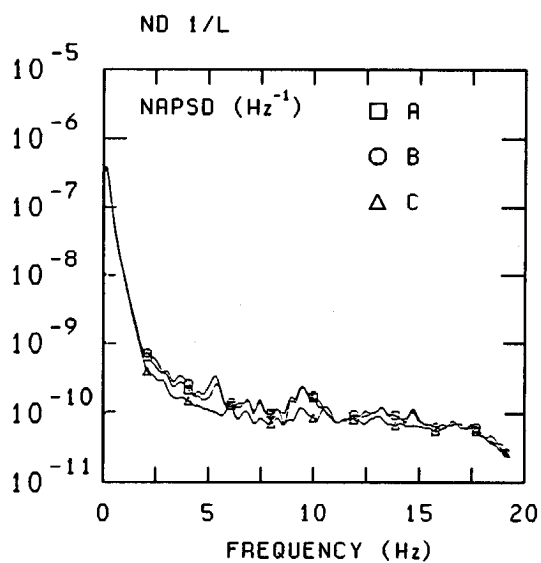


Figure 6.8: Changes in the APSDs at the onset of boiling.
 Experiment C: no boiling; A: boiling with $T_{out} = 95^{\circ}\text{C}$; B: boiling with $T_{out} = 97^{\circ}\text{C}$. ND1/H at 50 cm.

The NRMS increases by 40% at position 50 cm, where the void fraction is $\sim 2\%$ according to the effective bubble layer calculations. Bubble detachment starts at 48 cm, where $Pe = 0.0065$. The increase of the NRMS is much smaller in experiments with actual boiling than in the case of nitrogen injection. This is partly due to the special structure of the wall voidage. One has to keep in mind that periodic oscillations took place during bubble injection. These differences limit the possibility of using the analogy between actual boiling and bubble injection qualitatively.

6.6.4 An anomaly detection method

Methods of early detection of anomalies in reactors are of great practical interest. If the anomaly is strong, the detection method can possibly be based on the monitoring of the DC components of certain detector signals. We are interested in weak anomalies, when the DC components of the detectors (mostly in-core and ex-core neutron detectors) do not vary, or the actual changes are small and cannot be detected reliably.

In the framework of the present study, the coolant boiling is considered to be the anomaly. It has been shown earlier in this chapter that at the beginning of subcooled boiling in NIOBE, the variation of the DC component of SPNDs is undetectable (it is in the order of 0.1%), but certain properly chosen noise patterns clearly indicate boiling.

The degradation of the system is often a continuous process, and also the anomaly appears continuously. The associated noise signals represent nonstationary processes. The methods based on frequency-domain analysis of noise signals and used in this work have to be used with caution in the case of non-stationary processes. (Strictly speaking, they are not valid for non-stationary processes.) It will be assumed that the anomaly is weak and changes occur only slowly during the experiment. This means in practice that the duration of one measurement must be short, and the process can be considered to be stationary during this time interval. Further on, the analysis of the measured data based on this assumption is introduced.

An experiment lasts 230 s, and it includes 50 records of 4.6 s duration each. The inaccuracy of the NRMS is 1.2% for a 2 Hz wide frequency band according to Eq. (6.21). The results are shown in Fig. 6.9, where the relative change of the NRMS with regard to the situation without boiling is shown along the vertical axis for frequencies between 2 Hz and 4 Hz.

The location of detectors is given in Table III. A certain flow rate and heating power have been fixed at the beginning of the experiment. At a

later time instant (at 1510 s), pumping and heating were stopped by the safety system of NIOBE as a consequence of the decrease of water inventory by evaporation. This event can be clearly recognised from the drop of the NRMS of most of the SPNDs in Fig. 6.9.

TABLE III
Location of the SPNDs

No.	$TC_{out} = 95^{\circ}C$
ND1	String 1: 40 cm
ND2	String 1: 50 cm
ND3	String 3: 45 cm
ND4	String 3: 59 cm

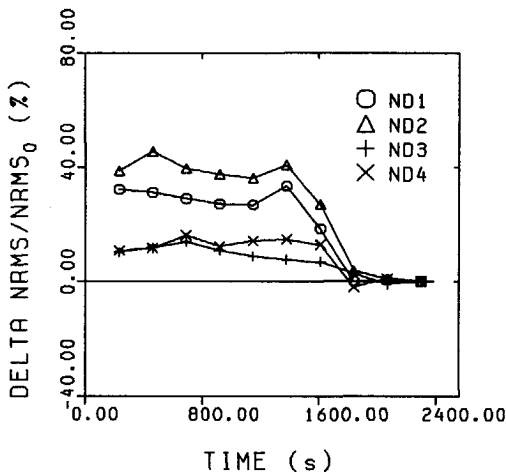


Figure 6.9: Time-behaviour of the NRMS of SPND signals in experiment with $TC_{out} = 95^{\circ}C$.

The NRMS fluctuates during the first period of the experiments (before the stop) as well. The magnitude of these fluctuations varies between 3 % and 5 % for strings 1 and 3, respectively. The statistical error of the measured NRMS (1.2 %) is much less than the observed fluctuation of the NRMS. Actual coolant temperature fluctuations (which are in the order of 0.5 - 1. °C during the experiments) yield fluctuating void fraction. This can be the reason for neutron noise NRMS fluctuations during boiling. The largest changes are indicated by detectors of string 1, while string 3 was much less sensitive to void fraction fluctuations.

6.7 Conclusions

Void effects have been monitored by means of the NRMS of in-core SPNDs at NIOBE. Conclusions based on Poisson theory of neutron noise generated by bubbly two-phase flow are valid only in a limited range of void fractions, between 1 % and 10%. Deviations from the theoretically expected relationship at large void fractions are explained by a non-Poissonian bubbling noise model.

The band-passed NRMS is capable of detecting wall voidage in the highly subcooled flow. The sensitivity of this void fraction detection method depends on the frequency band used for NRMS monitoring and on the accuracy of the experiment. A void fraction of 2% has been detected reliably at NIOBE at frequencies from 2 to 4 Hz. Further studies are necessary to determine the actual spectrum of void fraction fluctuations at subcooled boiling.

The SPNDs are located in the direct neighbourhood (within a few cm) of the boiling region at NIOBE. In pressurized water reactors, where the detection of small void fractions is of practical interest, the distance between the boiling region and the closest in-core neutron detectors can reach values of 20 to 30 cm. For example, one in-core string contains 6 neutron detectors along the 268 cm high core of the Borssele PWR [Upa84]. The background noise level is usually much higher at power reactors than at HOR. The sensitivity of a boiling detection method based on the high frequency neutron noise NRMS at power reactors, therefore, can differ from the results obtained at NIOBE.

Chapter 7

Low-Frequency Neutron Noise Analysis

Low-frequency neutron noise generated by coolant boiling is analysed in this chapter. Boiling may influence the low-frequency neutron noise component via thermohydraulic feedback. The experimentally observed boiling effects at NIOBE, however, cannot be caused by thermohydraulic feedback, as feedback effects are weak at HOR and, in addition, boiling at NIOBE has only a very weak influence on the reactivity of the core due to its actual location in the reflector. The measured boiling effects at low frequencies will be attributed to the non-white character of void fraction fluctuations.

7.1 Introduction

The experiments introduced in this chapter have thermohydraulic parameters which are similar to those described in Section 6.6, Chapter 6. Here, the main features of the experiments are given.

Coolant boiling has been induced at the fuel plate located in the middle of NIOBE. That plate is cooled from both sides by streaming coolant. The power of this plate has been 7 kW, a value which corresponds to heating conditions in a fuel assembly located in the central regions of HOR. The heating power level at the other two plates has been varied in order to achieve different coolant temperatures. At low heating, single-phase coolant took place in the channels. By increasing the heating of the side-plates, boiling has been generated at the middle plate. Experiments with various mass velocities have been performed. In the following, experiments with a

mass velocity of 227 kg/m²s are analysed. The outlet coolant temperature varied between 93 °C and 97 °C in experiments with boiling.

According to the thermohydraulic analysis given in Section 6.6, subcooled boiling without net void generation (NVG) occurs in the channels. The steam bubbles are attached to the wall. The maximum void fraction is about 2 between 45 cm and 50 cm.

Noise signals of SPNDs in strings 1, 2, and 3 were analysed at low frequencies. The frequency resolution was 0.0135 Hz in the analysis. The total duration of an experiment was 23 minutes. In the next section, spectral characteristics of measured SPND signals are evaluated.

7.2 Neutron noise coherence at low frequencies

Auto- and cross spectra, phase of the CPSD, and coherence between the two SPNDs in string 1 are shown in Fig. 7.1 under non-boiling (a) and boiling (b) conditions up to 1 Hz. The SPNDs are located in string 1 at axial positions 40 cm (detector 1) and 50 cm (detector 2), respectively. The magnitudes of the spectra show some changes at low frequencies when boiling occurs. The phase of CPSD remains zero over the whole frequency range. The coherence drops at low frequencies when boiling occurs.

Let us analyse first the behaviour of the coherence (γ^2). The coherence between noise signals A and B is defined as follows

$$\gamma^2 = \frac{|CPSD_{AB}(\omega)|^2}{APSD_A(\omega)APSD_B(\omega)} \quad (7.1)$$

where $CPSD_{AB}(\omega)$ is the cross spectrum of signals A and B; $APSD_A(\omega)$ are the autospectra of signal A and B, respectively.

The coherence shows a clear boiling effect in Fig. 7.1b. γ^2 is very high (close to unity) in the absence of boiling and decreases below 1 Hz in the experiment with boiling. The decrease is most remarkable below 0.3 Hz, and γ^2 drops to 0.7 at frequencies around 0.2 Hz. The statistical error of the coherence is in our case [Jen68]

$$\frac{\sigma_{\gamma^2}^2}{\gamma^2} = 2 \frac{W_b}{N} (1 - \gamma^2)^2 \quad (7.2)$$

where $W_b = 0.75$ for a Hanning window and N is the number of records. According to the above equation, the statistical accuracy of γ^2 increases with increasing γ^2 . If γ^2 approaches 1, $\sigma_{\gamma^2}^2 \rightarrow 0$. In the case of $N = 37$

APSD (Hz^{-1})

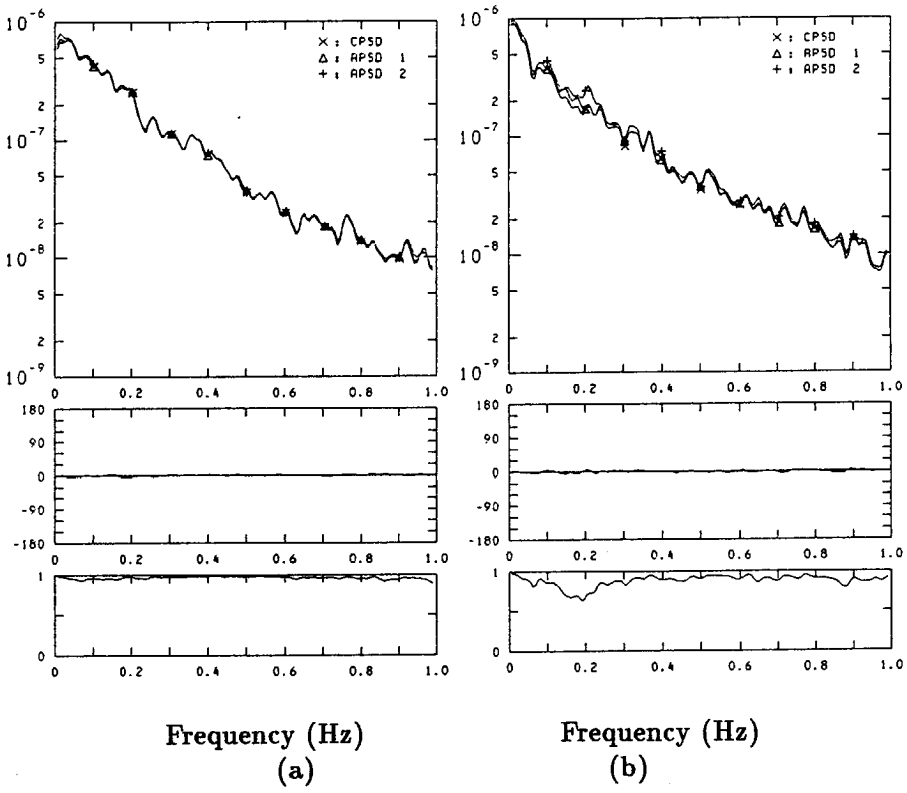


Figure 7.1: Magnitude, phase, and coherence of noise signals of SPNDs of string 1.

(a) : non-boiling, and (b) : boiling circumstances; the positions are: detector 1 - 40 cm, detector 2 - 50 cm.

and $\gamma^2 = 0.95$, $\sigma_{\gamma^2}/\gamma^2 = 0.0103$. This value is considerably smaller than the measured decrease of the coherence at low frequencies. Therefore, the change of the coherence caused by boiling at low frequencies is indeed significant.

The observed effect in the coherence is analysed by calculating the average coherence values over a certain interval. In this way, the statistical accuracy of the detection method can be further increased. Taking the average over n frequency points and assuming independence of these points, the accuracy of the average γ^2 is improved by a factor of \sqrt{n} compared to the accuracy of the individual points. In the evaluations, intervals 0.05 Hz to 0.3 Hz and 0.45 Hz to 0.7 Hz have been used. These intervals contain 18 points ($18 \approx 0.25 \text{ Hz}/\Delta f = 0.25/0.0135$), so the variance of the average coherency is decreased by a factor of 4.243 compared to the variance of a single coherence point.

The change of the average coherence ($\langle \gamma^2 \rangle$) has been monitored by making use of different detector combinations from strings 1 and 2. Average coherences have been calculated between SPNDs of one string and different strings as well.

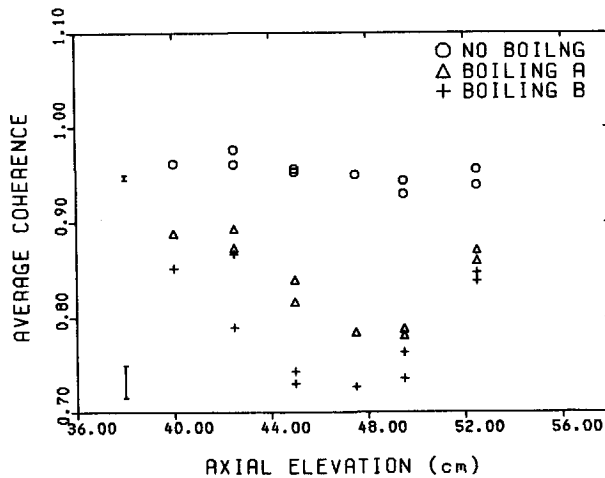


Figure 7.2: The space-dependence of the average coherence at frequencies [0.05 Hz, 0.3 Hz] with and without boiling.

The average coherence is shown for frequencies between 0.05 Hz and 0.3 Hz in Fig. 7.2. The boiling is more intensive in experiment B than in experiment A, but it remains subcooled in both cases according to thermo-hydraulic calculations. In Fig. 7.2, $\langle \gamma^2 \rangle$ values belonging to experiments

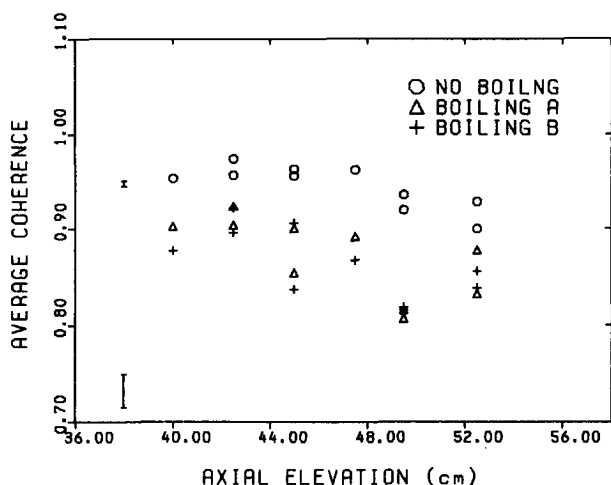


Figure 7.3: The average coherence at frequencies [0.45 Hz, 0.7 Hz]; experiments with and without boiling.

without boiling are shown as well. $\langle \gamma^2 \rangle$ is very high without boiling and drops significantly with boiling. The axial position (indicated along the x-axis) is the location of the middle point between the two SPNDs in that pair. The boiling effect is strongest in experiment B at axial elevations between 44 cm and 50 cm.

The relative error of $\langle \gamma^2 \rangle$ (calculated over 18 frequency points) is 0.25 % for a coherence level of 0.95 and it increases to 1.70 % for a coherence of 0.7. In Fig. 7.2, we observe much larger changes in $\langle \gamma^2 \rangle$ than these statistical errors.

According to the thermohydraulic analysis of boiling at NIOBE, wall voidage takes place at the fuel plates during subcooled boiling. The thickness of the bubble layer at the wall reaches a maximum value at axial elevations of about 50 cm and drops quickly at higher elevations due to the decreasing heating power (the axial distribution of the heat flux density has a chopped cosine shape in the fuel plates of NIOBE).

It also has been shown that thermohydraulic conditions do not allow appreciable bubble detachment. This result can explain the experimentally observed behaviour of the phase of CPSD between SPNDs in one string. Namely, no propagating void fraction fluctuations are present in the coolant channels in the absence of bubble detachment. The phase of the CPSD between signals of axially displaced SPNDs does not show a transport phe-

nomenon in this case, i.e., it remains zero, as it is seen in Fig. 7.1b. Moreover, the decrease of the coherence is strongest at axial elevations between 44 cm and 50 cm, where the thickness of the bubble layer is largest according to calculations.

The low-frequency boiling effect has been analysed by evaluating the average coherence over frequencies 0.45 Hz to 0.7 Hz as well; see Fig. 7.3. In the absence of boiling, $\langle \gamma^2 \rangle$ is still high, although it is smaller than at frequencies between 0.05 Hz and 0.3 Hz. This difference is less than 0.02, and it is covered partly by experimental errors. In the case of boiling, γ^2 decreases in Fig. 7.3, too, but the changes are much less pronounced than in Fig. 7.2. These results indicate the significance of neutron noise effects in the narrow frequency band of [0.05 Hz, 0.3 Hz]. The changes of the neutron noise intensity in various frequency regions is analysed in the next section.

7.3 Spectral distribution of boiling neutron noise

The neutron noise NRMS has been evaluated over frequency regions [0.05 Hz, 0.3 Hz] and [0.45 Hz, 0.7 Hz] for SPNDs in strings 1 and 2 in experiments with and without boiling. The results are given in Table IV. The location of the detectors are: ND1 - elevation 40 cm in string 1, ND2 - elevation 50 cm in string 1, ND3 - elevation 40 cm in string 2, and ND4 - elevation 65 cm in string 2.

TABLE IV
NRMS neutron noise over specified frequencies

No. detector	Boiling NRMS (10^{-4})		No boiling NRMS (10^{-4})	
	Frequency region (Hz)		Frequency region (Hz)	
	0.05 – 0.3	0.45 – 0.7	0.05 – 0.3	0.45 – 0.7
APSD ND1	2.488	0.908	2.597	0.866
APSD ND2	2.588	0.892	2.632	0.860
APSD ND3	2.521	0.908	2.615	0.873
APSD ND4	2.473	0.902	2.590	0.861
CPSD 1-2	2.434	0.878	2.582	0.855
APSD 3-4	2.418	0.878	2.568	0.852

The NRMS value over frequencies 0.05 Hz to 0.3 Hz is larger in experiments without boiling than in the case of boiling (experiment A). The

decrease of NRMS is found between 1.7 % and 4.7 % for different SPNDs. The error of the evaluated NRMS is 1.67 % according to the relationship $\sigma_{RMS}/RMS = 0.5\sqrt{0.75/(Nn)}$, where N is the number of records ($N = 37$) and n is the number of points in the considered frequency interval ($n = 18$). The observed change of the NRMS at boiling exceeds this value, so the increase of the NRMS is significant.

On the other hand, at frequencies between 0.45 Hz and 0.7 Hz, the NRMS neutron noise increases when boiling is present at NIOBE. Moreover, it is clear from the results of Chapter 6 that, at frequencies above about 1 Hz, the NRMS significantly increases at boiling due to the dominance of the local neutron noise component.

Next, possible reasons of decreasing NRMS values observed during boiling at frequencies below about 0.3 Hz are discussed.

Thermohydraulic feedback is weak at HOR. Moreover, due to the peripheral location of NIOBE, the reactivity of HOR is influenced only slightly by coolant boiling at NIOBE as is shown in Chapter 2. Reactivity fluctuations generate the global component of the neutron noise which is dominant at low frequencies. Therefore, no significant changes are expected due to global effects at NIOBE at low frequencies. It is concluded, therefore, that the observed effects below 0.3 Hz cannot be caused by feedback.

Let us consider the influence of local perturbations on the signals of SPNDs at NIOBE at low frequencies. It is often assumed in reactor noise models that the spectrum of void fraction fluctuations is white. In the case of white void fraction fluctuations, the local noise component is of no importance at low frequencies. But subcooled boiling at NIOBE has a very special character and its spectrum is not white due to the following reasons.

It has to be emphasised that bubbles do not enter the main coolant stream during subcooled boiling at NIOBE. Instead, they are attached to the wall and collapse in its direct neighbourhood. These bubbles move only slightly along the wall, or they do not move at all. A bubble may be present at a given position of the wall within the sensitivity volume of a neutron detector for a considerable time period. During this time, it contributes to the noise signal of the nearby ND. The lifetime of such a bubble can be several seconds at low flow rates, and it decreases with increasing flow rates [Bel88]. This effect is an important factor which contributes to the non-white character of void fraction fluctuations.

The present results point out the importance of studies aimed at the spectral distribution of void fraction fluctuations at subcooled boiling. To achieve proper statistical accuracy, long experiments are needed. It is dif-

difficult to maintain constant thermohydraulic parameters at NIOBE in an experiment of more than half hour duration. Due to this problem, a comprehensive study of the spectral distribution of boiling noise has not been accomplished in this work. The statistics of subcooled boiling has to be investigated in a well-instrumented experiment, preferably not in a nuclear reactor environment.

7.4 Remarks on feedback effects

Thermohydraulic feedback effects at HOR have been studied with the help of a coupled neutronic-thermohydraulic reactor noise model [Koz89b]. The results of model calculations show that feedback is weak at the HOR. Moreover, by applying non-nuclear (electrical) heating at NIOBE, the effect of fluctuations of coolant parameters on heat production is disregarded, and the thermohydraulic processes are, in fact, independent of the neutronics of the core. Some heat is coming from the HOR to the assembly (nuclear heating). However, the amount of this heat is always small compared to the applied electrical heating in experiments with boiling. The interaction between thermohydraulics and neutronic processes appears entirely through parametric density effects. The feedback loop is interrupted in this way.

One can try to modulate the heating power according to the measured neutron noise in order to close the interrupted feedback loop. It is also possible to increase (or decrease) the magnitude of the heating fluctuations, and the mechanism of the feedback can be investigated. The power supply unit of NIOBE can be used in remote mode, and its output voltage can be adjusted according to a controlled input signal added to a fixed DC voltage. This feature of the power unit makes it possible to establish an artificial feedback loop. Experiments have been performed with artificial feedback at NIOBE. In these experiments, the filtered and amplified signal of an SPND has been used to control the electrical heating power. Some variations have been observed in the neutron noise, but the measured effects were not pronounced, and no quantitative conclusions could be drawn concerning feedback effects.

NIOBE is located in the first row of the reflector, adjacent to an actual fuel assembly. There is a relatively large distance (5 cm) between the coolant in the simulated assembly and the fission material of the actual fuel. Therefore, the thermohydraulic changes in the coolant affect the fission process less intensively than in the case of an actual fuel assembly. This is the reason

for the weak neutronic effects even in the case of strong artificial feedback. Stronger neutronic effects can be induced by positioning NIOBE inside the core, but this experiment has not been accomplished in the framework of the present work.

7.5 Conclusions

Boiling effects at low frequencies have been studied in this chapter. A disadvantage of the experiments at low frequencies is the long measurement time which is necessary to achieve proper statistical accuracy. The method is slow, and it is difficult to realize early detection of anomalies.

Boiling effects have been detected at NIOBE at low frequencies, below ~ 0.3 Hz. Both the spectral densities and the coherence between noise signals of in-core SPNDs vary at those frequencies. The phase of the CPSD does not change in experiments with boiling compared to experiments without boiling, i.e., the phase remains zero.

A significant effect is found in the coherence. γ^2 drops from a value about 1 to ~ 0.7 in the neighbourhood of 0.2 Hz. By introducing the average coherence over a narrow band at low-frequencies, a quantitative characterisation of this boiling effects is given.

Possible reasons for the measured low-frequency effects have been analysed. According to theoretical calculations, feedback effects are weak at HOR, and they cannot be responsible for the phenomena observed in the experiments. The properties of void generation without bubble detachment during subcooled boiling at NIOBE are factors which contribute to the observed phenomena. To obtain further insight into the relationship between the boiling state of the coolant and $\langle \gamma^2 \rangle$, further experiments are necessary, in which the movable SPND strings would scan the axial neutron noise field.

Due to the low-frequency character of the phenomenon to be investigated, this is a time-consuming task. Taking into account the technical problems we face during long experiments at NIOBE this question has not been dealt with in the present study.

APPENDIX A

Nomenclature of most important symbols

<i>Symbol</i>	<i>Definition</i>
a	- thermal diffusivity (m^2/s)
A	- surface area (m^2)
c_p	- specific heat (kJ/kgK)
c_o^2	- void coefficient of detector current variance at $\alpha = 0$ ($\text{A}^2/(\% \text{ void})$)
c_α	- void coefficient of detector current ($\text{A}/(\% \text{ void})$)
d	- channel width (m)
D_e	- equivalent diameter of channel (m)
D_g	- neutron diffusion coefficient in the g-th energy group (cm)
E_f	- energy release per fission (J)
f	- frequency (Hz)
G	- mass flux density (mass velocity) ($\text{kg}/\text{m}^2\text{s}$)
G	- number of energy groups
h	- enthalpy (kJ/kg)
h	- heat transfer coefficient ($\text{kW}/\text{m}^2\text{K}$)
I	- current (A)
k	- multiplication coefficient of the reactor
k	- heat conductivity ($\text{W}/\text{m}\cdot\text{K}$)
L	- heat loss (kW/m^3)
N	- number of records per measurement
N	- number of independent events in Bernoulli process
Nu	- Nusselt number: $Nu = \frac{hD_e}{k}$
p	- pressure (bar)
p, q	- probabilities of outcomes of a Bernoulli event; $p = 1 - q$
P	- heating power (kW)
Pe	- Peclet number: $Pe = \frac{Nu}{St} = \frac{D_e G c_p}{k}$
Pr	- Prandtl number: $Pr = \frac{\mu c_p}{k}$
q''	- heat flux density (kW/m^2)
Q	- heating power per unit volume via convection (kW/m^3)
r	- distance (m)
R	- relative variation of the detector signal

Re	- Reynolds number: $Re = \frac{GD_c}{\mu}$,
S	- heating power per unit volume via direct heating (kW/m ³)
St	- Stanton number: $St = \frac{h}{c_p G}$
t	- time variable (s)
T	- time period (s)
T	- temperature (K)
u	- total energy (kJ/kg)
v	- velocity (m/s)
U	- voltage (V)
V_{fm}	- volumetric flow measured by flowmeter (m ³ /s)
V	- volume (m ³)
w_i	- i-th background noise component
x, y, z	- spatial variables (m)

Greek Letters

α	- volumetric void fraction
α_L	- existence probability of mode 1 in a in a bimodal system
α_i	- attenuation constant of the i-th component of a neutron wave (m ⁻¹)
β	- fraction of delayed neutrons
γ^2	- coherence
δ	- bubble radius (m)
Θ	- temperature noise source (K)
κ	- i-th spatial eigenvalue of neutron noise field (m ⁻¹)
$\bar{\lambda}$	- decay constant of delayed neutrons (s ⁻¹)
μ	- dynamic viscosity (kg/(m·s))
μ	- expected value of a stochastic variable
ν_g	- number of fission neutrons in the g-th group
ξ_i	- phase constant of the i-th component of a neutron wave (m ⁻¹)
ρ	- density (kg/m ³)
σ	- standard deviation
Σ_{fg}	- fission macroscopic cross-section in the g-th group (cm ⁻¹)
$\Sigma_{sg' \rightarrow g}$	- scattering macroscopic cross-section from group g' to group g (cm ⁻¹)
Σ_R	- removal macroscopic cross-section (cm ⁻¹)
τ	- time delay (s)

τ	- time constant (s)
φ	- phase of CPSD
Φ_g	- neutron flux in the g-th group ($\text{cm}^{-2}\text{s}^{-1}$)
Φ_g^+	- adjoint function in the g-th group
χ_g	- relative yield of fission neutrons in group g
ω	- angular frequency (rad/s)

Subscripts

<i>bg</i>	- background
<i>boil</i>	- at boiling
<i>B</i>	- bubble
<i>BM</i>	- bimodal
<i>c</i>	- coolant
<i>D</i>	- detector
<i>f</i>	- film property
<i>F</i>	- fuel plate
<i>G</i>	- measured by flowmeter
<i>in</i>	- inlet
<i>p</i>	- peak value
<i>s</i>	- saturation
<i>sat</i>	- wall superheat above saturation
<i>sub</i>	- subcooling
<i>W</i>	- fuel wall surface

Acronyms

<i>APSD</i>	- auto power spectral density function
<i>ARMA</i>	- autoregression moving average
<i>BWR</i>	- boiling water reactor
<i>CCF</i>	- cross correlation function
<i>CPSD</i>	- cross power spectral density function
<i>FC</i>	- forced convection
<i>FDNB</i>	- fully-developed nucleate boiling
<i>HFCF</i>	- high-frequency contribution fraction
<i>HOR</i>	- Higher Educational Reactor (Hoger Onderwijs Reactor)
<i>INER</i>	- Institute of Nuclear Energy Research, Taiwan
<i>IRI</i>	- Interfaculty Reactor Institute, Delft
<i>LWR</i>	- light water reactor

<i>MTR</i>	- material testing reactor
<i>ND</i>	- neutron detector
<i>NIOBE</i>	- experimental setup for Noise Investigations On Boiling Effects
<i>NPP</i>	- nuclear power plant
<i>NRMS</i>	- normalized root-mean-square
<i>NVG</i>	- point of net vapour generation
<i>ONB</i>	- onset of nucleate boiling
<i>PDF</i>	- probability density function
<i>PWR</i>	- pressurized water reactor
<i>SB</i>	- saturated boiling
<i>SCB</i>	- subcooled boiling
<i>SPND</i>	- self-powered neutron detector
<i>TC</i>	- thermocouple

APPENDIX B

A Model of Temperature Diffusion in the Fuel Plate

Temperature effects in the fuel plate are modelled with the help of the fuel heat balance equation. For the sake of simplicity, assume one- dimensional fuel along the z -axis. Considering temperature effects in a sufficiently small z -segment, we can assume that the fuel is infinite. Then, the initial value problem is written as:

$$\frac{\partial T}{\partial t} = \frac{k_F}{c_{pF}\rho_F} \frac{\partial^2}{\partial z^2} T + \frac{q'''(z, t)}{c_{pF}\rho_F} - \frac{h}{c_{pF}\rho_F} \gamma (T - T_c), \quad t > 0; \quad (\text{B.1})$$

with initial condition

$$T(z, t = 0) = T_0(z). \quad (\text{B.2})$$

The notations are

- $T(z, t)$ - space- and time-dependent fuel plate temperature (K),
- k_F - fuel plate heat conductivity ($\text{kW}/\text{m} \cdot \text{K}$),
- ρ_F - fuel plate density (kg/m^3),
- c_{pF} - specific heat of the fuel plate ($\text{kJ}/\text{kg} \cdot \text{K}$),
- h - fuel-to-coolant heat transfer coefficient ($\text{kW}/\text{m}^2 \cdot \text{K}$),
- γ - heat-transfer surface per unit fuel volume ($1/\text{m}$),
- T_c - coolant temperature (K),
- $q'''(z, t)$ - heat source term (kW/m^3).

We intend to calculate temperature disturbances in the fuel plate caused by the appearance of a bubble attached to the wall. This can be taken into consideration via the heat source term in Eq. (B.1). Assume uniform heat generation along the fuel and constant temperature in the fuel before the appearance of the bubble on the wall. In this case without a hot spot, thermal equilibrium exists in the plate, i.e., the total amount of heat generated in a unit fuel volume is completely transferred to the coolant due to convective heat transfer. As soon as a bubble appears on the wall and does not detach, the fuel-to-coolant heat transfer coefficient drops significantly nearby this

bubble. This means that the local equilibrium breaks down and the temperature of the plate begins to increase. On the other hand, heat transfer conditions remain unchanged further away from this bubble.

Let us restrict our studies to the beginning of this process, when the increase in the local plate temperature is much smaller than the difference between the channel wall and coolant temperatures. The influence of this nondetachable steam bubble will be modelled by an effective heat source q'''_{eff} at the bubble position. In practical calculations the following form of $q'''_{eff}(z, t)$ has been used:

$$q'''_{eff}(z, t) = \begin{cases} 0 & \text{if } t \leq 0 \\ q'''_0 \delta^2 / (\delta^2 + z^2) & \text{if } t > 0, \end{cases}$$

where q'''_0 is the heat source density at the bubble position (kW/m^3), and 2δ is the characteristic size of the isolation (bubble) at the surface. In model calculations, the following parameters of the aluminium plates were used: $k = 0.23 \text{ kW}/\text{m}\cdot\text{K}$, $\rho = 2.7 \cdot 10^3 \text{ kg}/\text{m}^3$, $c_p = 0.89 \text{ kJ}/\text{kg}\cdot\text{K}$, $q'''_0 = 4.96 \cdot 10^4 \text{ kW}/\text{m}^3$.

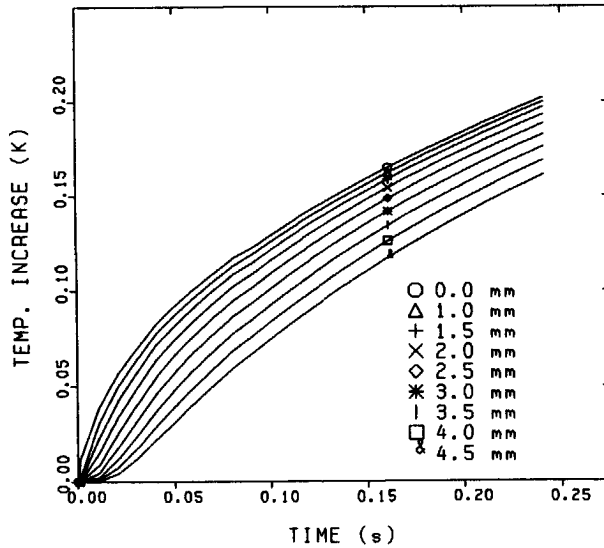


Figure B.1: Calculated time-behaviour of plate temperature around a boiling centre

The time-behaviour of the calculated temperature increase with respect to the stationary situation is depicted in Fig. B.1, where each curve corresponds to a certain position measured from the boiling centre. For our

purposes, it is important to determine the time interval which is necessary to reach a certain temperature at a given position, because the activation of new boiling centers around the original bubble is a function of the local temperature of the plate. This time lag can be determined from Fig. B.1, considering the beginning of the process. In the case of an initial hot spot of size $\delta = 0.3$ mm, this time is 0.0051 s between positions 0 mm and 1 mm at a temperature level of $\Delta T = 0.12K$, which yields a velocity of expansion of the high temperature region in the plate $v = 0.1/0.0051$ cm/s = 19.6 cm/s. By changing δ between 0.1 mm and 1 mm, velocity values of 30 to 10 cm/s are obtained.

The time-lag between curves in Fig. B.1 increases with increasing time; we also get larger time lags at positions farther away from the boiling origin. Generally speaking, the velocity is time- and space-dependent, and it always has to be averaged in one way or another, in order to obtain a certain velocity value. This point can be illustrated by the following considerations. The mean-square distance, $\langle r^2 \rangle$, characterizing the temperature diffusion in the plate is given by

$$\langle r^2 \rangle = 6at, \quad (\text{B.3})$$

where $a = k/(c_p \rho) = 9.57 \cdot 10^{-4}$ m²/s is the fuel thermal diffusivity. Equation (B.3) can be derived, for example, by making use of the analogy between the time-dependent diffusion equation and the Fermi-age equation; see e.g. [Dud76]. Based on Eq. (B.3), a time-dependent velocity can be obtained: $v(t) = \sqrt{6a/t}$. Taking the average of $v(t)$ over time interval $[0, T]$, we get an average velocity of the form:

$$\bar{v}_T = 2\sqrt{6a/T}.$$

The average velocity decreases with increasing time: it is inversely proportional to the square root of the duration of the considered time interval. Calculating the average over a time interval 0.08 s, the value of the average velocity will be 16.9 cm/s.

As soon as the temperature increase is sufficiently large and the bubble still sticks to the wall, new boiling centres are activated around the initial bubble, and the heat source term in Eq. (B.1) has to be modified (extended). These additional source terms yield higher temperatures. In the framework of the present linear model, we do not change the heat source term, and the initial tendency of temperature increase is used to estimate the possible velocity range of temperature variations in the plate.

Bibliography

- [Alb82] Albrecht R.W. et al. (1982) 53 Progr. Nucl. Energy, Vol. 9, p.37
- [Ana84] Analytis G.Th., Lubbesmeyer D. (1984) Prog. Nucl. Energy, Vol. 14, p.95
- [Att78] Atta Y.N. et al. (1978) Nucl. Sci. Engng., Vol. 66, p.264
- [Bat76] Batchelor G.K., Miles I.W. (1976) "The Structure of Turbulent Shear Flow", Cambridge Univ. Press
- [Bau88] Bauernfeind V., D. Wach (1988) "Anomaly Detection by Spectral Analysis of Incore Neutron Flux Fluctuations", Proc. OECD/NEA Specialists' Meeting on Incore Instrumentation and Reactor Core Assesment, Cadarache, France, p.376
- [Beh77] Behringer K., G. Kosaly, Lj. Kostic (1977) Nucl. Sci. Engng., Vol. 63, p.306
- [Beh79] Behringer K., G. Kosaly, I. Pazsit (1979) Nucl. Sci. Engng., Vol. 72, p.304
- [Beh81] Behringer K., R.D. Crowe (1981) Atomkernenergie, Vol. 38, p.47
- [Beh82] Behringer K. et al. (1982) Progr. Nucl. Energy, Vol. 9. p.75
- [Beh83] Behringer K. (1983) Ann. nucl. Energy, Vol. 10, p.433
- [Bel88] Belhadj M., T. Aldemir, R.N. Christensen (1988) Nucl. Technology, Vol. 82, p.330
- [Bel91] Belhadj M., T. Aldemir, R.N. Christensen (1991) Nucl. Technology, Vol. 95, p.95

- [Ber64] Bergles A.E., W.N. Roshenow (1964) J. Heat Transfer, Trans. ASME, Series C, Vol. 86, p.365
- [Ber82] Bernard P., J. Cloue, C. Messainguiral (1982) Progr. Nucl. Energy, Vol. 9. p.581
- [Bjo82] Bjorge R.W., G.R. Hall, W.M. Roshenow (1982) Int. J. Heat Mass Transfer, Vol.25, No.6, p.753
- [Blu82] Blumentritt G. et al. (1982) Proc. of CMEA-Seminar "Heat Physics - TF '82", Karlovy Vary, CSSR, in Russian
- [Cee76] Ceelen D., P. Gebureck , D. Stegemann (1976) Atomkernenergie Vol. 27, p. 239
- [Col86] Collatz S., Rindelhardt U.(1986) Annals nucl. energy, Vol. 13, No 6, p293.
- [Def88] Defloor J., R. Baeyens (1988) Progr. Nucl. Energy, Vol. 21, p.547
- [Del77] Delhay I.M. (1977) Two-Phase Flow and Heat Transfer Proceedings of NATO Adv. Studies Institute, Istanbul 1976, Vol. 1, Washington-London
- [Dif80] Diflippio F.C., P.J. Otaduy (1980) Nucl. Sci. Engng., Vol. 75, pp.258-264
- [Dud76] Duderstadt J.J., L.J. Hamilton (1976) "Nuclear Reactor Analysis", p.363, John Wiley and Sons Inc., N.Y.
- [Duk86] Dukler A.E., Y. Taiter (1986) Multiph. Sci. Tech., Vol. 2, p.1
- [DVr86] Vries J. De, H. Van Dam, G. Gysler (1986) "Protection System for Minimizing the Consequences of a Flow Blockage Incident at a Pool-Type Research Reactor", IAEA-SM-310/86P, p.543
- [ElW78] El-Wakil M.M. (1978) Nuclear Heat Transfer. ANS
- [Fed82] Federico A. et al. (1982) Prog. Nucl. Energy, Vol. 9, p.631
- [Fow71] Fowler T.B., D.R. Vondy, G.W. Cunningham (1971) "Nuclear Reactor Core Analysis Code: CITATION", ORNL-TM-2496,Rev.2.
- [Fug77] Fuge R. et al. (1977) Annals Nucl. Energy, Vol. 4, p.161

- [Hoo85] Hoogenboom J.E. et al. (1985) Progr. Nucl. Energy, Vol. 15, p.771
- [Hoo88] Hoogenboom J.E. (1988) Report IRI-131-88-07
- [Ish75] Ishii M. (1975) "Thermo-Fluid Dynamic Theory of Two-Phase Flow", Eyrolles, Paris
- [Jen68] Jenkins G.M., D.G. Watts (1968) "Spectral Analysis and Its Applications", Holden Day, S.F./U.S.A.
- [Jon75] Jones O.C., N. Zuber (1975) Int. J. Multiph. Flow, Vol. 2, p.273
- [Kat78] Katona T. (1978) Report KFKI-1978-64, in Russian
- [Kat83] Katona T. (1983) Diagnostics of Subcooled Boiling in WWER-Type Nuclear Reactors, Thesis, Moscow Univ. Energ., in Russian
- [Kat85] Katona T. (1985) Progr. Nucl. Energy, Vol. 15, p.685
- [Kat88] Katona T., R. Kozma (1988) Progr. Nucl. Energy, Vol. 21, p.431
- [Kin89] King C.H. et al. (1989) Nucl. Technology, Vol. 86, p.70
- [Kle79] Kleiss E., H. van Dam (1979) Annals nucl. energy, Vol. 6, p.385
- [Kle81a] Kleiss E., H. van Dam (1981) Nucl. Technology, Vol.53, p.31.
- [Kle81b] Kleiss E., H. van Dam (1981) Annals nucl. energy, Vol. 8, p.205
- [Kon82] Konno H., K. Saito (1982) Progr. Nucl. Energy, Vol. 12, p. 291
- [Kos75] Kosaly G., L. Maroti, L. Mesko (1975) Annals nucl. energy, Vol. 2, p.315
- [Kos77] Kosaly G. et al. (1977) Prog. Nucl. Energy, Vol. 1, p.99
- [Kos82] Kosály G. (1982) et al. Progr. Nuclear Energy, Vol. 9. p.23
- [Koz85a] Kozma R. (1985) Annals nucl. energy, Vol. 12, p.247
- [Koz85b] Kozma R., L. Mesko (1985) Progr. Nucl. Energy, Vol. 15, p.699
- [Koz86] Kozma R. (1986) "Application of a Coupled Thermohydraulic-Neutronic Model for the Diagnosis of Thermohydraulic Anomalies in the Core of PWRs", Summary KFKI-86-48, in Hungarian

- [Koz88a] Kozma R. (1988) "Feedback and Dispersion Laws in LWRs", Proc. 1988 International Conference on Reactor Physics, Jackson Hole, Wyoming, U.S.A., Vol. 3, p.423
- [Koz88b] Kozma R., J.E. Hoogenboom, H. van Dam (1988) "Boiling Detection Using Signals of SPNDs and Thermocouples", in: Proc. OECD/NEA Specialists' Meeting on In-core Instrumentation and Reactor Assessment, Cadarache, France, p.390
- [Koz88c] Kozma R. (1988) Progr. Nucl. Energy, Vol. 21, p.309
- [Koz89a] Kozma R., J.T. Van Bloois (1989) Report IRI-131-89-007
- [Koz89b] Kozma R. (1989) Report IRI-131-89-016
- [Koz90a] Kozma R., J.E. Hoogenboom, H. van Dam (1990) Kernenergie, Vol. 33, p.191
- [Koz90b] Kozma R., J.E. Hoogenboom (1990) Annals nucl. energy, Vol. 17, p.493
- [Koz91] Kozma R. (1991) "Interpretation of Velocities Measured by Neutron Noise in BWRs", Proc. 6th Symp. on Nuclear Reactor Surveillance and Diagnostics, Knoxville, U.S.A., Vol. 2, pp. 38.01-38.11
- [Koz92] Kozma R., H. Van Dam, J. E. Hoogenboom (1992) Nuclear Technology, Vol. 99, (to appear)
- [Mes84] Mesko L., R. Kozma (1984) Nucl. Sci. Engng. Vol. 88, p.88
- [Lah78] Lahey R.T. Jr., G. Krycuk, B.K. Malaviya (1978) Trans. ANS, Vol. 30, p.497
- [Lub83a] Lubbesmeyer D. (1983) Ann. nucl. Energy, Vol. 10, p.421
- [Lub83b] Lubbesmeyer D., B. Leoni (1983) Int. J. Multiph. Flow, Vol. 9, p.665
- [Lub84] Lubbesmeyer D. (1984) Progr. Nucl. Energy, Vol. 14, p.41
- [Mit79] Miteff L. (1979) Report EIR-373
- [Mit82] Miteff L., K. Behringer (1982) Progr. Nucl. Energy, Vol. 9, p.649

- [Nab89] Nabbi R. (1989) "HEATHYD - A One-Dimensional Code for the Iterative Calculation of Heat Transfer and Coolant Distribution at Parallel Plate Fuel Elements", KFA Julich , NEA Data Bank Code No.: NEA 1292/01.
- [Paz81] Pazsit I. (1981) *Annals nucl. energy*, Vol. 8, p.393
- [Por84] Por G., S. Horanyi, O.J. Dikanarov (1984) *Annals nucl. energy*, Vol. 11, p.197
- [Por88] Por G., O. Glockler, U. Rindelhardt (1988) *Progr. Nucl. Energy*, Vol. 21, p.555
- [Rin85] Rindelhardt U. et al. (1985) *Progr. Nucl. Energy*, Vol. 15, p.225
- [Roh85] Rohsenow W.M., J.P. Hartnett, E.N. Ganic (1985) *Handbook of Heat Transfer Fundamentals*, McGraw Hill, N.Y.
- [Sah74] Saha Pr., N. Zuber (1974) "Point of Net Vapour Generation and Vapour Void Fraction in Subcooled Boiling", *Proc. 5th Internat. Heat Tr. Conf.*, Tokyo, Vol. IV, p.175
- [Sei73] Seifritz W., Cioli F. (1973) *Trans. Am. Nucl. Soc.*, Vol. 17, p.451
- [Sti91] Stigter B. (1991) Personal Communication
- [Sud86] Sudo Y. et al. (1986) *J. Nucl. Sci. Tech.*, Vol. 23, p.73
- [Ton79] Tong L.S., J. Weisman (1979) "Thermal Analysis of PWRs", ANS
- [Upa84] Upadhyaya B.R., E. Turkcan (1984) *Analysis of Neutron Detector and Core Exit Thermocouple Signals in the Borssele Reactor*, Nov. 1984, The University of Tennessee, Knoxville, U.S.A.
- [VDa76] Van Dam H. (1976) *Atomkernenergie*, Vol. 27, p.8
- [VDH88] Hagen T. Van Der, J. Van Der Voet (1988) *Prog. Nucl. Energy*, Vol. 21, p.565
- [VDH89] Hagen Van Der T. (1989) *Stability Monitoring of a Natural-Circulation-Cooled Boiling Water Reactor*, Thesis, Delft Univ. of Technology, p.139
- [VMe84] Meulenbroek van B.M. (1984) Report IRI-131-84-05

- [VMe85] Meulenbroek B.M. van, Wakker B.M. van de (1985) Int. J. Heat Mass Transfer, Vol. 28, p.886
- [Vin82] Vince M.A., R.T. Lahey Jr. (1982) Int. J. Multiph. Flow, Vol. 8, p.99
- [Woo84] Woodruff W.L. (1984) Nucl. Technology, Vol. 64, p.196
- [Wac73] Wach D. (1973) Atomwirtschaft, Vol. 15, p.580
- [Wac74] Wach D., Kosaly G. (1974) Atomkerenergie Vol. 23, p.244
- [Wan88] Wang Y.W., C.H. King, B.S. Pei (1988) Nucl. Technology, Vol. 83, p.56
- [Wan89] Wang Y.W. et al. (1989) Trans. ANS, Vol. 59, p.365
- [Wer86] Werner M. et al. (1986) Kernenergie, Vol. 39, p.144

SUMMARY

Noise Investigations On Boiling Effects In a Simulated MTR-type Fuel Assembly

In this thesis, boiling effects in nuclear reactors are studied. The experimental part of the work has been performed at the NIOBE facility using the Hoger Onderwijs Reactor (HOR) of the Interfaculty Reactor Institute, Delft, The Netherlands. NIOBE is an acronym for Noise Investigations On Boiling Effects. Thermohydraulic and neutronic processes in an MTR-type fuel assembly of the HOR are simulated at NIOBE by making use of an electrically heated fuel assembly. The parameters of the coolant in NIOBE can be varied over a wide range. This feature allows one to study the influence of coolant boiling on the neutron noise field in an actual nuclear reactor.

The present work includes results in three major topics: (1) validation/testing of existing neutron noise methods under well-controlled circumstances; (2) investigation of boiling phenomena in narrow channels; (3) development of a novel boiling monitoring method.

In Chapter 1, the tasks and main methods of boiling detection in nuclear reactors are introduced. Chapter 2 contains the description of NIOBE and the experimental circumstances. It is pointed out that boiling at NIOBE has only a very weak reactivity effect due to its peripheral location in the reflector region of the HOR. The experimental studies are based on the analysis of noise signals of self-powered neutron detectors and thermocouples which belong to the instrumentation of NIOBE and which are located in the direct neighbourhood of the boiling region.

Noise signals of thermocouples in the channel wall have been used for velocity profile monitoring, as is shown in Chapter 3. It is found that velocities inferred from the slope of the phase curve of the cross power spectral density functions between axially displaced thermocouples at low frequencies give a good estimation of the area-averaged coolant velocity. At higher

frequencies, above about 1 Hz, the corresponding inferred velocities are close to the estimated maximum of the radial velocity profile.

Flow patterns in the boiling coolant are identified by means of analysis of probability density functions and spectra of neutron noise, according to the results of Chapter 4. Criteria are derived for detection of bubbly and slug flows on the basis of the second and fourth moments of probability densities of the neutron noise. It has been shown that boiling has an oscillating character in the narrow coolant channels of NIOBE due to partial channel blockage caused by steam slugs generated periodically between the plates. The period of this process is about 4.5 s. These oscillations yield sharp resonance peaks in the power spectral densities of neutron noise at low frequencies. The parameters of these experiments correspond to conditions with low flow and nominal power in the HOR. These conditions might occur at HOR during accidental partial blockage of a few coolant channels.

Local neutron noise effects are studied in Chapters 5 and 6. The sensitivity of the boiling detection method based on monitoring the intensity of the neutron noise at high frequencies is found to be about 1 % void fraction for neutron detectors located at a distance of 2 - 3 cm from the boiling region. This sensitivity margin can have a different value at power reactors where the actual distance between the neutron detectors and the region with subcooled boiling can be much larger than a few cm. No deviation from the zero phase of cross spectra between self-powered neutron detectors has been observed during subcooled boiling at NIOBE.

The bubbling source term of the neutron noise is often assumed to be a Poisson process. This approximation is found to be valid only in a limited range of low void fractions at NIOBE. The reasons for the difference between the Poisson theory and the experimental results are the non-white character of the void fraction fluctuations and the inconsistency of this theory at high void fractions. In Chapter 6, an alternative model is developed which explains the experimentally observed deviation from the Poisson theory at high void fractions.

In Chapter 7, boiling neutron noise at low frequencies is analysed. A remarkable boiling effect has been observed experimentally in the coherence between SPNDs at various spatial positions at frequencies below 1 Hz. This effect is attributed to the special boiling phenomenon at a low level of boiling at NIOBE. Based on experimental and theoretical analysis, it is found that thermohydraulic feedback is not significant at NIOBE due to its weak reactivity effect.

SAMENVATTING

Onderzoek naar kookeffecten in een gesimuleerd splijstofelement door middel van kernreaktorruis

In dit proefschrift worden kookeffecten in nucleaire reactoren bestudeerd. Het experimentele gedeelte van het werk werd uitgevoerd in de NIOBE opstelling bij de Hoger Onderwijs Reactor (HOR) van het Interfacultair Reactor Instituut in Delft. De naam NIOBE is een acroniem voor Noise Investigations On Boiling Effects. Thermohydraulische en neutronische verschijnselen in een splijstofelement van de HOR worden met een elektrisch verhit modelelement in NIOBE gesimuleerd. De parameters van het koelmiddel in NIOBE kunnen worden gevarieerd tussen brede grenzen, waardoor verschillende kookverschijnselen kunnen optreden in de koelkanalen. In NIOBE werd met name de invloed van koken op de neutronenruis van de HOR bestudeerd.

Dit proefschrift bevat resultaten op de volgende gebieden: (1) de validatie en het testen van bekende kookdetectiemethoden onder goed gecontroleerde omstandigheden; (2) het bestuderen van de eigenschappen van koken in smalle kanalen; (3) het ontwikkelen van een nieuwe kookdetectiemethode.

In Hoofdstuk 1 worden de taken en methoden van kookdetectie in nucleaire reactoren beschreven. De constructie van NIOBE en de experimentele omstandigheden worden in Hoofdstuk 2 besproken. Koken in NIOBE heeft geringe reactiviteitseffecten omdat het niet in de kern van HOR zelf plaatsvindt, maar in de reflector. In de kookexperimenten worden ruissignalen van self-powered neutronendetectors en thermokoppels geanalyseerd, die aangebracht zijn in het gesimuleerde splijstofelement, dus in de directe omgeving van het kookgebied.

In Hoofdstuk 3 worden resultaten gepresenteerd van metingen van snelheidsprofielen met behulp van thermokoppels in de wand van de koelkanalen.

Het blijkt, dat de gemiddelde snelheid van het koelmiddel in het koelkanaal (gemiddeld over de doorsnede van het kanaal) bepaald kan worden door middel van analyse bij lage frequenties (kleiner dan 1 Hz) van de fase van het kruisvermogenspectrum van ruissignalen van boven elkaar in de wand gelokaliseerde thermokoppels. Snelheden die zijn verkregen uit de fase van het kruisspectrum boven 1 Hz, liggen dicht bij het geschatte maximum van het radiale snelheidsprofiel.

In Hoofdstuk 4 worden stromingspatronen in het kokende koelmiddel geïdentificeerd d.m.v. analyse van kansdichtheidsfuncties en spectra van neutronenruis. Bellen- en slugstromingen kunnen worden gedetecteerd op basis van de analyse van het tweede en vierde moment van de kansdichtheidsfunctie van de neutronenruis. Koken in de smalle kanalen van NIOBE vertoont een oscillerend gedrag veroorzaakt door de gedeeltelijke afsluiting van de koelkanalen door grote stoombellen (slugs). Deze oscillaties hebben een periode van ongeveer 4,5 s en het spectrum van de neutronenruis vertoont scherpe resonantiepieken bij lage frequenties. De parameters van deze experimenten corresponderen met HOR-condities bij nominaal vermogen, maar laag koeldebiet. Deze condities kunnen optreden in de HOR tijdens een ongeluk met gedeeltelijke afsluiting van enkele koelkanalen.

Lokale neutronenruiseffecten worden in Hoofdstuk 5 en 6 geanalyseerd. De gevoeligheid van de kookdetectiemethode gebaseerd op het bepalen van de intensiteit van neutronenruis bij hoge frequenties bedraagt ongeveer 1 % dampfractie in het geval van neutronendetectors gelokaliseerd op een afstand van 2 - 3 cm van het kookgebied. Deze gevoeligheid kan een andere waarde hebben bij vermogensreactoren, waarin de afstand tussen het kookgebied en de dichtsbijzijnde in-core neutronendetectors veel meer kan bedragen dan enkele cm. Tijdens onderkoeld koken in NIOBE werd in de kruisspectra van self-powered neutronendetectors geen van nul afwijkende fase waargenomen.

De bronterm van neutronenruis wordt in de literatuur vaak beschouwd als een Poisson-proces. Deze aanname is alleen geldig in een beperkt gebied van bellenfractie in NIOBE. Het verschil tussen Poisson-theorie en experimentele resultaten wordt veroorzaakt door het niet-witte spectrum van de fluctuaties van de bellenfractie en door de inconsistentie van deze theorie bij grotere bellenfracties. Een nieuw model voor fluctuaties van de bellenfractie wordt in Hoofdstuk 6 besproken. Dit model is geschikt om de experimentele resultaten bij grotere bellenfracties te verklaren.

Hoofdstuk 7 gaat dieper in op de analyse van neutronenruis bij lage frequenties. Uit de coherenties tussen neutronenruissignalen bij frequenties

beneden 1 Hz konden plaatsafhankelijke kookeffecten worden gedetecteerd. Die effecten worden toegeschreven aan de speciale kookverschijnselen bij een laag niveau van koken in NIOBE. Uit experimentele en theoretische analyse blijkt thermohydraulische terugkoppeling niet significant te zijn in NIOBE wegens het geringe reactiviteitseffect.

ACKNOWLEDGEMENTS

I would like to express my gratitude to everybody who helped me in completing the work presented in this thesis.

First of all, I want to thank Prof. Dr. Ir. H. van Dam for making it possible for me to perform my promotion work under his supervision and for his constant support and valuable discussions. I greatly appreciate the continuous attention, useful discussions and critical remarks of Dr. Ir. J.E. Hoogenboom.

My colleagues at the Department of Reactor Physics created an excellent working atmosphere for fruitful research. I would like especially to thank Dr. Ir. Tim van der Hagen for the useful discussions and Ir. Jim Kuijper and Ir. Jan-Leen Kloosterman for their valuable remarks and suggestions concerning the manuscript. Jelle Schut has been an indispensable "motor" for the experimental work, while Ir. Piet de Leege helped me greatly in computer calculations. I am indebted to Ronald Otte and Dick de Haas for their technical assistance. Also, the contributions of Theo van Bloois and Peter Leemker are appreciated.

I am indebted to the members of the Reactor Operation Group of HOR for their help in performing the experiments with NIOBE. The reliable work of the Computer System Group of IRI is hereby acknowledged.

It was my privilege to work together with Dr. Özer Ciftciouglu of Istanbul Technical University, Turkey, Dr. Achim Pohlus of ZfK Rossendorf and GRS Garching, Germany, and Dr. Janos Valkó of CRIP, Budapest during their stay at IRI. The suggestions of Dr. Joe Thie (Consultant), Knoxville, U.S.A. and Prof. Dr. Imre Pázsit of Chalmers University, Göteborg, Sweden were most useful to me. I also wish to thank Steven Gilbert for his advice regarding the English text.

Finally, I want to thank you, Valika, for your support and help in completing this thesis.

CURRICULUM VITAE

Born on May 10th, 1958, in Szeged, Hungary

EDUCATION

- | | |
|------------------------------|---|
| 1972 -1976 | High School "Gymnasium Endre Sagvari", Szeged
- Secondary education certificate with distinction
specialized in mathematics |
| 1976 - 1982 | University of Energetics, Moscow, USSR
- majoring in nuclear power stations and equipments |
| Autumn 1981 | - Master's project at Zentralinstitut für
Kernforschung (ZfK), Rossendorf, G.D.R. |
| Feb. 20 th , 1982 | - Diploma of Engineer-Physicist, with distinction |
| 1983 - 1988 | Eötvös Lorand University of Arts and Sciences,
Budapest, Hungary |
| Jun. 27 th , 1988 | - Master of Science Degree in Applied Mathematics
qualification of his Degree: "outstanding" |

WORK EXPERIENCE

- | | |
|---------------------|--|
| 1982 - 1988 | Central Research Institute for Physics, Budapest
- research assistant, then research fellow
investigating noise effects in nuclear reactors |
| May - Nov. 1986 | Interuniversity Reactor Institute, Delft
- guest researcher carrying out experiments at HOR |
| Jun. - Sep. 1988 | Prizma Co., Budapest
- safety analysis for Nuclear Power Plant 'Paks' |
| Sep.1988 - May 1992 | Interfaculty Reactor Institute, Delft University of
Technology
- carrying out research on boiling detection in nu-
clear reactors at the Reactor Physics Department |

LIST OF PUBLICATIONS
related to this thesis

- Kozma R., J.E. Hoogenboom, and H. Van Dam, "Boiling Detection Using Signals of SPNDs and Thermocouples," *Proc. OECD/NEA Specialists' Meeting on In-core Instrumentation and Reactor Assessment*, 1988, Cadarache, France, pp. 390-398 (1988)
- Kozma R., "Feedback and Dispersion Laws in Light-Water Reactors," *Proc. American Nuclear Society 1988 International Conference on Reactor Physics*, Jackson Hole, Wyoming, U.S.A., 3, pp.423-432 (1988)
- Kozma R., J.E. Hoogenboom, and H. van Dam, "Experimental Investigation of the Field-of-View of Neutron Detectors," *Kernenergie*, 33, pp.191-199 (1990)
- Kozma R. and J.E. Hoogenboom, "Flow Measurements Using Noise Signals of Axially Displaced Thermocouples," *Annals nucl. energy*, 17, pp. 493-513 (1990)
- Kozma R., "Interpretation of Velocities Measured by Neutron Noise in BWRs," *Proc. 6th Symp. on Nuclear Reactor Surveillance and Diagnostics*, 1991, Knoxville, U.S.A., 2, pp. 38.01-38.11 (1991)
- Kozma R., H. Van Dam, and J. E. Hoogenboom, "Identification of Flow Patterns by Neutron Noise Analysis During Actual Coolant Boiling in Thin Rectangular Channels," *Nuclear Technology*, 99, to appear (1992)
- Kozma R., "Void-Fraction Measurements in Two-Phase Flows Via Neutron Noise Methods," *Int. J. Multiph. Flow*, to be published (1992)